CHARACTERIZATION AND DESIGN OF INSULATOR-BASED DIELECTROPHORESIS DEVICES FOR CONTINUOUS-FLOW PARTICLE ENRICHMENT AND AUTOMATED ELECTRODE-BASED DIELECTROPHORETIC CHARACTERIZATION OF MYCOBACTERIUM SMEGMATIS

A Dissertation

Presented to the Faculty of the Graduate School

of Cornell University

in Partial Fulfillment of the Requirements for the Degree of

Doctor of Philosophy

by

Benjamin George Hawkins

January 2011

CHARACTERIZATION AND DESIGN OF INSULATOR-BASED DIELECTROPHORESIS DEVICES FOR CONTINUOUS-FLOW PARTICLE ENRICHMENT AND AUTOMATED ELECTRODE-BASED DIELECTROPHORETIC CHARACTERIZATION OF MYCOBACTERIUM SMEGMATIS

Benjamin George Hawkins, Ph.D.

Cornell University 2011

In this work we detail the development of insulator-based dielectrophoresis devices to be used for enrichment of cellular subpopulations with phenotypic differences in membrane composition. We present a novel insulator-based dielectrophoresis device design that incorporates coherently patterned three-dimensional channel constrictions and demonstrate continuous flow particle separation based on dielectrophoretic mobility. Experimental and numerical techniques were used to characterize the effects of channel geometry on particle motion and distilled to a set of design criteria for similar devices. We also detail further characterization of fluid motion due to electrothermal fluid body forces via numeric multiphysics simulations. These simulations model heat transport via convection through the channel and conduction through the substrate material and consider the coupling between fluid, electrical, and thermal equation systems via temperature-dependent material properties. Finally, we discuss the development of an automated electrode-based dielectrophoresis device for cell characterization and its application to *Escherichia coli* as well as wild-type and ethambutol-treated *Mycobacterium smegmatis*. We discuss these results in the context of *Mycobacterial* physiology and the mechanism of action of ethambutol.

BIOGRAPHICAL SKETCH

Benjamin G. Hawkins was inspired, at the age of 5, to obtain a Ph.D., by his uncle, Dr. Henry Lauren Pugh — so that he could get a Nintendo. Now, so many years later, he realizes that there was probably an easier way.

Born in 1981 in Fresno, CA, Ben was first inspired in the sciences by his 6th grade teacher, Richard Vezzolini. In 2000, Ben began his degree in electrical engineering at California State University, Fresno as a member of the Smittcamp Family Honors College. In 2005, he graduated Summa Cum Laude, with minors in math and physics, as the Dean's Medalist in the College of Engineering. Later that year, he began his doctoral work in the Biomedical Engineering Department at Cornell University. In 2006, Ben officially joined the Kirby research group and was awarded a Graduate Research Fellowship from the National Science Foundation to conduct his doctoral research.

Beyond his academic endeavors, Ben has a deep love of the outdoors. In addition to mountain biking, ice climbing, mountaineering, and backpacking, he trains and competes in off-road triathlons.

After completing his doctorate, Ben plans to assume a position as a guest researcher at the National Institute of Standards and Technology through the National Academy of Sciences Research Associateship Program. He is looking forward to his future pursuits, both athletic and academic, as Dr. Hawkins.

This work is dedicated to my wife, Sarah, for her constant support and motivation.

ACKNOWLEDGEMENTS

First and foremost, I would like to thank my family and friends for their continual support; without them, I never would have come this far.

I would like to thank my advisor and committee chair, Prof. Brian J. Kirby. I am lucky to have Prof. Kirby's advice and guidance though academic and professional challenges. Not only have I gained knowledge of the field, but also gained experience as a researcher, presenter, teacher, and professional though the opportunities that he has provided. Professor Kirby works incredibly hard to create a particular kind of environment for his students, where pressure and motivation to answer research questions through designing intelligent experiments is balanced against a relaxed atmosphere where mistakes and missteps are part of the process. A significant portion of my personal and professional development as a graduate student is due solely to the efforts and support of Prof. Kirby. He has unquestioningly supported my desire to enter academia and provided me every possible opportunity to succeed. Working for him has been a truly formative experience.

I also would like to thank my committee members, Prof. Donald Koch and Prof. David Russell, for their support, insight, and direction as I learned, not only more about two separate fields that were brand new to me, but how to do research and approach research questions.

My colleagues in the Kirby research group and the Biomedical Engineering Department have been deep source of insight and motivation. From the Kirby research group, Srinitya Arasanipalai, Nick Baldasaro, Nik Bordia, Charlie Huang, James Li, Zeke Smith, Ivo Stranic, Yusef Syed and Yvonne Tsui all contributed tangibly to the my research efforts. Alex Barbati, Sowmya Kondapalli, Erica Pratt, and Vishal Tandon provided countless hours of advice and support. I would also like to thank Jason Gleghorn for his work supporting my research and his help and advice on searching for post-

doctoral positions. Robby Bowles was a continual source of amusement, motivation, and self-confidence.

My time here at Cornell has been made pleasant and effortless through the work of Belinda Hine-Floyd in the Biomedical Engineering Department and Marcia Sawyer in the Sibley School of Mechanical and Aerospace Engineering. Belinda and Prof. Chris Schaffer in the Biomedical Engineering Department made possible a number of activities and events that I never thought possible during my time as President of the Cornell Biomedical Engineering Society. Thank you for all of your help!

Finally, I must thank my undergraduate advisors Prof. Nagy Bengiamin, Prof. Ramakrishna Nunna, and Prof. Kausik Chatterjee for their continual support of my academic efforts. And to all the people mentioned above, all my friends and family, and especially my wife Sarah: thank you for your continual support and unwavering faith in my abilities.

TABLE OF CONTENTS

LIST OF TABLES

LIST OF FIGURES

CHAPTER 1

INTRODUCTION

The primary focus of this work is on developing dielectrophoresis-based devices to separate or enrich particle[1] populations based on their dielectric properties, characterizing confounding factors in such devices, such as electrothermal flow, and characterizing particle dielectrophoretic reponse as a function of the frequency of the applied electric field. Throughout this work, the intended outcome is to develop a continuous-flow cell separation or enrichment technique that is sensitive to phenotypic differences in the composition of the cell membrane. Our interest in the cell membrane is motivated by bacterial populations such as *Mycobacterium tuberculosis* whose primary adjuvant effects are tied to the composition of their membrane structure[1, 2]. Dielectrophoresis (DEP) refers to the force on a polarizable particle in a non-uniform electric field, and, as discussed in Chapter 2, depends on cell composition. Therefore, the DEP force is an attractive tool for researchers attempting to sort, separate, enrich, manipulate, or characterize cellular samples.

Careful characterization of device and particle can be used to overcome the limitations[3] of dielectrophoresis, such as its strong size dependence, and implement a successful cell sorting technique.

The phenomena of dielectrophoresis has its origins in electromagnetism, but reaches into many different fields. The primary focus of this work is the integration of DEP into microfluidic platform with applications to *Mycobacteria*. Because DEP forces depend on gradients in the applied electric field, they benefit from scaling down to micrometer length scales where such gradients are stronger and easier to generate.

[1] Throughout this text the term "particle" will be used in a general sense, to mean either a polystyrene microsphere, biological cell, or other generic microscale colloid. The term "cell" will be used exclusive of non-biological particles.

1.1 *Mycobacteria*

Members of the genus *Mycobacterium* are gram-positive aerobic bacteria possessing a thick, waxy coating of covalently bound lipids[4]. The outer portion of the cell envelope of *Mycobacterium tuberculosis* contains a particular lipid — trehalose dimycolate — that has been shown to induce inflammation and granulomatous host responses[5, 1, 2]. In part due to its densely packed, hydrophobic outer envelope, *M. tuberculosis* has developed antibiotic-resistant, multiply-drug-resistant, and *completely*-drug-resistant strains[5, 2, 4, 6]. While the likelihood of tuberculosis infection in the developed portions of the world is low, infection incidence remains high in developing countries where access to medical supplies is limited and the prevalence of immunocompromising diseases such as HIV and AIDS is high[4, 7]. In many cases, tuberculosis infection is opportunistic, remaining dormant or asymptomatic until such time as the host immune system is compromised[8, 9].

Antibiotic drugs typically target the cell membrane, and this is particularly true in the case of *Mycobacteria*. The biosynthesis of mycolic acids and derivatives such as trehalose dimycolate remains an active area of research. One primary avenue of investigation is to isolate mutants with a particular susceptability or resistance and extrapolate portions of the biosynthetic pathway from genotypic and phenotypic information. For *Mycobacteria*, these key biosynthetic pathways involve membrane biosynthesis.

The membrane structure of *Mycobacterium* continues to be an active area of research, and while the detailed structure may vary from species to species, the gross features remain. The cytoplasmic membrane is surrounded by peptidoglycan (PG). A polysaccharide, arabinogalactan, is bound to PG, which provides the covalent anchoring point for mycolic acids[4, 7]. Covalently bound mycolic acids of various types form the

core–lipid structure of the mycobacterial envelope. Non-covalently bound lipids, including various mycolic acids, accumulate in a thick pseudocapsule outside the covalently bound layer[4, 10, 11, 12, 13]. Paul, et al.[10, 11, 12], examined cellular cross sections of freeze-substituted *Mycobacteria* using electron microscopy. The results show large electron transparent zones indicative of the collection of lipids in this extracellular space. This pseudocapsular material can be removed by gentle agitation in the presence of a surfactant[14].

Our efforts in this line of inquiry are directed toward developing a device capable of screening a population of *Mycobacteria* for phenotypic differences in membrane composition. One such population of interest is the product of a transposon mutagensis process. Random transposon mutagenesis is a process by which genes are disrupted by the insertion of a transposon from a plasmid. The insertion element disrupts the function of the gene. Transposon mutagenesis in *mycobacteria* has been demonstrated using transposons Tn5367, Tn5368, and Tn5370. The insertion element Himar1 also transposes efficiently in *mycobacteria* [4]. Trasponon mutagenesis allows the insertion site to be tagged by the insertion element, streamlining subsequent analysis to identify the disrupted genes in subsequent genomic analysis. By screening a population of randomly transposed mutants and isolating a subpopulation with phenotypic differences in membrane composition, we can streamline genomic analysis and isolate disrupted genes that contribute to altered membrane phenotype.

1.1.1 *Mycobacterium smegmatis*

In this work, *M. smegmatis* was used as a fast-growing, non-pathogenic surrogate for *M. tuberculosis*. While there are many differences between the two species, such as

different protein expression profiles, the general structure and composition of the cell envelope is conserved, as are the shapes and sizes of the bacteria. While the doubling time of *M. tuberculosis* is on the order of 18 to 24 hours, *M. smegmatis* doubles approximately every 2 hours[7]. *M. smegmatis* maintains the same cell wall structure found in its pathogenic cousins.

1.1.2 Ethambutol

Ethambutol is an anti-mycobacterial drug known to inhibit the attachment of mycolic acids via inhibition of the biosynthesis of arabinogalactan (AG)[4]. While the specific method of action is unknown, the primary action site is on the formation of functional arabinose[15, 16], more specifically, the polymerization of D-arabinofuranose[17, 18]. The evidence provided in these studies, via ^{14}C incorporation after treatment with ethambutol, is supported by additional evidence of the accumulation of D-arabinofuranose precursors in the cytoplasm and the initial evidence against ethambutol as a mycolic acid inhibitor — the accumulation of trehalose monomycolate, trehalose dimycolate, and free mycolic acids in the extracellular media[19].

Additional evidence for the removal of the exterior, covalently attached lipids from *Mycobacteria* after treatment with ethambtol can be found in recent work by Verbelen, et al.[20] and Alsteens, et al.[21] who imaged *M. smegmatis* before and after treatment with ethambutol using atomic force microscopy. Initial work shows that cells have a soft, smooth surface prior to treatment, and a rough, striated surface afterwards[20]. Subsequent studies paired AFM imaging of the cell surface with immunogold labeling and adhesion measurements. Immunogold AFM imaging confirms that treatment with ethambutol exposes liparabinomannan (LAM) by inhibiting the incorporation of AG

into the cell membrane. This is consistent with the mechanism of action of ethambutol, which seems to preferentially inhibit the polymerization of arabinose in AG compared to LAM. Thus, the recent findings using immunogold labeling of LAM [21] are consistent with earlier work by Mikusova, et al.[17], and Deng, et al.[18], who demonstrated latency in ^{14}C uptake between AG and LAM after treatment with ethambutol.

1.2 Dielectrophoresis: Summary of Chapters and Accomplishments

Dielectrophoresis (DEP) is the transport of polarizable particles in response to a nonuniform electric field, exclusive of electrophoresis [22]. DEP forces depend on the magnitude and nonuniformity of an externally applied electric field, as well as the complex permittivity of a particle and its surrounding media [23]. The complex permittivities ($\tilde{\varepsilon} = \varepsilon - i\sigma/\omega$) of the particle and surrounding media are a function of the frequency of the polarizing electric field, ω, electrical conductivity, σ, and permittivity, ε; the permittivity, ε, is assumed independent of frequency over the range used in this study. The combination of material- and frequency dependence makes DEP a useful technique for researchers attempting to manipulate, separate, and characterize particles and cells.

Owing to its unique material and frequency dependent nature, DEP techniques have the potential to identify cellular subpopulations with phenotypic differences in membrane composition without *a priori* knowledge of the nature of the specific nature of the mutation. We hypothesize that a subpopulation of random mutants could be enriched for mutants with specific differences in membrane composition using DEP. DEP potentially offers a label-free option for preferential cellular manipulation. A number of approaches can be used to induce electric field non-uniformities, ranging from various

electrode configurations to purely insulative techniques. A survey of the origins and assumptions used to describe DEP, numerical techniques and analytical approximations used model particles of various shapes and compositions, and the experimental devices and techniques used to generate and utilize DEP forces is presented in **Chapter 2**.

The initial development work of this project focused on creating an insulator-based DEP device to achieve continuous-flow particle separation based on DEP mobility. To do this we examined an insulating constriction in channel depth and developed and tested a new set of design criteria using polystyrene particles. Using these criteria, we designed a device with three dimensional constrictions in channel depth. The constrictions curved transverse to the direction of flow, changing the direction of DEP forces as a function of transverse position. Based on the design criteria, the particle distribution across the width of the channel outlet is a function of DEP mobility. In **Chapter 3**, we discuss the operation of this device and confirm its ability to achieve continuous flow particle separation as a function of DEP mobility.

While investigating the behavior of insulator-based DEP devices, we identified a key factor that was not quantitatively addressed in the literature: electrothermal flow. Electrothermal effects are well documented in electrode-based devices for dielectrophoresis, AC electroosmosis, and other electrokinetic effects driven by the application of electric fields in solution. To address the effects of electrothermal flow, specifically in insulator-based DEP systems fabricated in polymeric substrates (such as those discussed in **Chapter 3**), we devised and implemented a set of numeric simulations to quantify the effects of electrothermal flow on particle trajectories near an electrically insulating constriction in channel depth. Owing to the finite thermal Péclet number in the channel, these computations included the coupling between fluid, electrical, and thermal equation systems via temperature dependent fluid properties. We specifically model temperature

dependent electrical permittivity and conductivity, viscosity, thermal conductivity, and specific heat. Heat is generated via Joule heating, transported via electroosmotic fluid flow and electrothermally induced flow, and conducted through the channel substrate. Heat convection outside the device and conduction through the substrate is modeled using empirical relationships and a linearized heat transfer coefficient, respectively. The results of this work (detailed in **Chapter 4**) quantify the change in particle pathlines owing to electrothermal effects as a function of fluid conductivity, AC and DC electric field magnitudes, particle electrophoretic mobility, channel electroosmotic mobility, and constriction geometry.

In **Chapter 3** we develop a set of device design criteria for insulator-based DEP devices and verified the operational characteristics using polystyrene particles. In **Chapter 4**, we quantify the potentially confounding effects of electrothermal flow on particle trajectories in insulator-based DEP devices. In **Chapter 5**, we discuss the development of an automated DEP characterization technique for measuring the frequency dependence and relative magnitude of the positive DEP force on particles. The technique was developed and tested on polystyrene particles and *Escherichia coli* bacteria and the results compared to similar measurements in the literature[24, 25]. The technique was then applied to wild-type and ethambutol treated *M. smegmatis* to quantify the change in the dielectrophoretic force as a function of frequency. Significant changes in the membrane composition induced by treatment with ethambutol induced an equally significant change in cellular dielectrophoretic response.

1.3 Related Work

While a summary of DEP theory and techniques addressed in the literature is presented in **Chapter 2**, we also highlight here some key works that specifically address mainly microbiological questions using dielectrophoresis or dielectrophoresis-related techniques. The work presented in **Chapter 5** is based on techniques developed by Sanchis, et al.[24], and Gascoyne, et al.[26], who characterized *E. coli* and *Staphylococcus aureus* and normal and cancerous eurythrocytes, respectively, using "collection spectra". Castellarnau, et al.[25], used measurements of the cross-over frequency (where the DEP force changes from positive to negative, or vice versa) to differentiate between isogenic mutants of *E. coli*. They found that by interpreting their results in the context of a spheroidal multishell model (discussed in this work in **Chapters 2 and 5**), they were able to predict the phenotype of four separate strains based on their measurements. Hoettges, et al.[27], utilized a "DEP-well" system to analyze the antibiotic resistance of *E. coli* populations by monitoring the change in cellular dielectrophoretic response over time and interpreting the data in terms of a simplified cell model. Cell viability was determined based on changes in cytoplasmic conductivity.

Electrorotation measurements depend on a rotational torque on a particle rather than a translational force, but are related to the same cellular composition. These measurements have been used to differentiate viable from non-viable bacterial biofilms[28], characterize human B- and T-lymphocytes, monocytes, and granulocytes[29], and determine the transport properties of lipophilic ions myeloma cells[30].

Lapizco-Encinas and co-workers have demonstrated multiple applications of insulator-based dielectrophoresis techniques, separating live and dead *E. coli* and separating mixtures of any two species among *E. coli*, *Bacillus subtilis*, *B. cereus*, and *B.*

megaterium. In what it perhaps the most relevant example of insulator-based DEP, Barrett, et al.[31], demonstrated continuous flow separation of *B. subtilis* from polystyrene beads in a glass microfluidic channel with angled constrictions in channel depth. To the best of the authors knowledge, only one group has demonstrated dielectrophoretic manipulation of *Mycobacterium*. Zhu, et al.[32], characterized *M. smegmatis* cells in active, "viable-but-not-culturable" (VBNC), and dead states. Using the information obtained from characterization they utilized castellated electrode arrays at a specified frequency to deplete VBNC cells from a flowing suspension.

BIBLIOGRAPHY

[1] E. Rhoades, F-. F. Hsu, J. B. Torrelles, J. Turk, D. Chatterjee, and D. G. Russell. Identification and macrophage-activating activity of glycolipids released from intracellular Mycobacterium bovis BCG. *Molecular Microbiology*, 48(4):875–888, May 2003.

[2] Elizabeth R Rhoades, Rachel E Geisel, Barbara A Butcher, Sean McDonough, and David G Russell. Cell wall lipids from Mycobacterium bovis BCG are inflammatory when inoculated within a gel matrix: characterization of a new model of the granulomatous response to mycobacterial components. *Tuberculosis (Edinburgh, Scotland)*, 85(3):159–76, May 2005.

[3] J Voldman. Electrical forces for microscale cell manipulation. *Annual review of biomedical engineering*, 8:425–54, 2006.

[4] S. T. Cole, K. D. Eisenach, D. N. McMurray, and Jr. Jacobs, W. R., editors. *Tuberculosis and the Tubercle Bacillus*. ASM Press, Washington, DC, 2005.

[5] Rachel E Geisel, Kaori Sakamoto, David G Russell, and Elizabeth R Rhoades. In vivo activity of released cell wall lipids of Mycobacterium bovis bacillus Calmette-Guérin is due principally to trehalose mycolates. *Journal of immunology (Baltimore, Md. : 1950)*, 174(8):5007–15, April 2005.

[6] Y. Zhang and W. W. Yew. Mechanisms of drug resistance in Mycobacterium tuberculosis. *The International Journal of Tuberculosis and Lunch Disease*, 12(11):1320–1330, 2009.

[7] C Ratledge and Jeremy Dale, editors. *Mycobacteria: Molecular Biology and Virulence*. Blackwell Science, Oxford, UK, 1999.

[8] Erik C Hett and Eric J Rubin. Bacterial growth and cell division: a mycobacterial perspective. *Microbiology and molecular biology reviews : MMBR*, 72(1):126–56, table of contents, March 2008.

[9] M J Smeulders, R A Speight, Jacquie Keer, and H D Williams. Adaptation of Mycobacterium smegmatis to stationary phase. *Journal of bacteriology*, 181(1):270–83, January 1999.

[10] T R Paul and T J Beveridge. Reevaluation of envelope profiles and cytoplasmic ultrastructure of mycobacteria processed by conventional embedding and freeze-substitution protocols. *Journal of bacteriology*, 174(20):6508–17, October 1992.

[11] T R Paul and T J Beveridge. Ultrastructure of mycobacterial surfaces by freeze-substitution. *Zentralblatt für Bakteriologie : international journal of medical microbiology*, 279(4):450–7, November 1993.

[12] T R Paul and T J Beveridge. Preservation of surface lipids and determination of ultrastructure of Mycobacterium kansasii by freeze-substitution. *Infection and immunity*, 62(5):1542–50, May 1994.

[13] Akemi Takade, Akiko Umeda, Masanori Matsuoka, Shin-ichi Yoshida, Masahiro Nakamura, and Kazunobu Amako. Comparative studies of the cell structures of Mycobacterium leprae and M. tuberculosis using the electron microscopy freeze-substitution technique. *Microbiology and immunology*, 47(4):265–70, January 2003.

[14] A Ortalo-Magné, A Lemassu, M A Lanéelle, F Bardou, G Silve, P Gounon, G Marchal, and M Daffé. Identification of the surface-exposed lipids on the cell envelopes of Mycobacterium tuberculosis and other mycobacterial species. *Journal of bacteriology*, 178(2):456–61, January 1996.

[15] K Takayama, E L Armstrong, K A Kunugi, and J O Kilburn. Inhibition by ethambutol of mycolic acid transfer into the cell wall of Mycobacterium smegmatis. *Antimicrobial agents and chemotherapy*, 16(2):240–2, August 1979.

[16] K Takayama and J O Kilburn. Inhibition of synthesis of arabinogalactan by ethambutol in Mycobacterium smegmatis. *Antimicrobial agents and chemotherapy*, 33(9):1493–9, September 1989.

[17] K Mikusová, R A Slayden, G S Besra, and P J Brennan. Biogenesis of the mycobacterial cell wall and the site of action of ethambutol. *Antimicrobial agents and chemotherapy*, 39(11):2484–9, 1995.

[18] L Deng, K Mikusová, K G Robuck, M Scherman, P J Brennan, and M R McNeil. Recognition of multiple effects of ethambutol on metabolism of mycobacterial cell envelope. *Antimicrobial agents and chemotherapy*, 39(3):694–701, March 1995.

[19] J O Kilburn and K Takayama. Effects of ethambutol on accumulation and secretion of trehalose mycolates and free mycolic acid in Mycobacterium smegmatis. *Antimicrobial agents and chemotherapy*, 20(3):401–4, September 1981.

[20] Claire Verbelen, Vincent Dupres, Franco D. Menozzi, Dominique Raze, Alain R Baulard, Pascal Hols, and Yves F Dufrêne. Ethambutol-induced alterations in Mycobacterium bovis BCG imaged by atomic force microscopy. *FEMS microbiology letters*, 264(2):192–7, November 2006.

[21] David Alsteens, Claire Verbelen, Etienne Dague, Dominique Raze, Alain R Baulard, and Yves F Dufrêne. Organization of the mycobacterial cell wall: a nanoscale view. *Pflügers Archiv : European journal of physiology*, 456(1):117–25, April 2008.

[22] Herbert A Pohl. *Dielectrophoresis: The behavior of neutral matter in nonuniform electric fields*. Cambridge University Press, 1978.

[23] Thomas B Jones. *Electromechanics of Particles*. Cambridge University Press, New York, 1995.

[24] A Sanchis, A P Brown, M Sancho, G Martínez, J L Sebastián, S Muñoz, and J M Miranda. Dielectric characterization of bacterial cells using dielectrophoresis. *Bioelectromagnetics*, 28(5):393–401, 2007.

[25] M Castellarnau, A Errachid, C Madrid, A Juárez, and J Samitier. Dielectrophoresis as a tool to characterize and differentiate isogenic mutants of Escherichia coli. *Biophysical journal*, 91(10):3937–45, November 2006.

[26] P.R.C. Gascoyne, J. Noshari, F.F. Becker, and R. Pethig. Use of dielectrophoretic collection spectra for characterizing differences between normal and cancerous cells. *IEEE Transactions on Industry Applications*, 30(4):829–834, 1994.

[27] Kai F Hoettges, Jeremy W Dale, and Michael P Hughes. Rapid determination of antibiotic resistance in E. coli using dielectrophoresis. *Physics in medicine and biology*, 52(19):6001–9, October 2007.

[28] X-F Zhou, G. H. Markx, Ronald Pethig, and Ian M Eastwood. Differentiation of viable and non-viable bacterial biofilms using electrorotation. *Biochimica et Biophysica Acta (BBA) - General Subjects*, 1245(1):85–93, August 1995.

[29] Jun Yang, Ying Huang, Xiao-Bo Wang, X.B. Wang, F.F. Becker, and P.R.C. Gascoyne. Dielectric properties of human leukocyte subpopulations determined by electrorotation as a cell separation criterion. *Biophysical journal*, 76(6):3307–3314, 1999.

[30] O Reuss. Interaction of fluorinated lipophilic ions with the plasma membrane of mammalian cells studied by electrorotation and dielectrophoresis. *Journal of Electrostatics*, 56(4):419–434, 2002.

[31] Louise M Barrett, Andrew J Skulan, Anup K Singh, Eric B Cummings, and Gregory J Fiechtner. Dielectrophoretic manipulation of particles and cells using insu-

lating ridges in faceted prism microchannels. *Analytical chemistry*, 77(21):6798–804, 2005.

[32] Junjie Zhu, Tzuen-Rong J Tzeng, and Xiangchun Xuan. Continuous dielectrophoretic separation of particles in a spiral microchannel. *Electrophoresis*, 31(8):1382–8, April 2010.

CHAPTER 2

DIELECTROPHORESIS FOR PARTICLE AND CELL MANIPULATIONS

2.1 Abstract

In this chapter, we will explore the use of dielectrophoresis (DEP) for particle and cell manipulation. This is a broad field, and so our aim will be to present the theory behind several dielectrophoresis techniques, as well as specific experimental recipes. Initially, we will present the concept and theoretical underpinnings of DEP and build a framework of approximations that connect our theoretical development to engineering design and experimental implementation. First, from a theoretical perspective, we will approach DEP techniques based on the properties of the driving electric field and introduce experimental techniques for manipulating these field properties. Next, from an experimental perspective, we will approach DEP techniques based on device geometries used to generate electric field non-uniformities and report specific methodologies for reproducing experimental results. Finally, from a design perspective, we will present DEP techniques based on the resulting motion of particles in the system and examine a variety of demonstrated applications.

2.2 Introduction: Physical origins of DEP

The term "dielectrophoresis" was used by Herbert A. Pohl as early as 1951 in describing the motion of particles in response to a non-uniform electric field [2]. In that work, "dielectrophoresis" describes the force — exclusive of electrophoresis — exerted on

[0]The content of this chapter was submitted and accepted for publication as a book chapter titled "Dielectrophoresis for Particle and Cell Manipulation" in *Methods in Bioengineering: Biomicrofabrication and Biomicrofluidics*[1].

polarizable particles, as a function of their complex permittivity, in the presence of an externally-applied, non-uniform electric field. In this work, we additionally include the torque experienced by a particle in a rotating electric field. We reason that these phenomena are related in that each is dependent, in some manner, on the relative complex permittivities of a particle and its surrounding media.

Dielectrophoresis originates from the response of matter to an electric field, and more specifically, from differences in this response across an interface. In an electric field, a perfectly conducting material will transport electrons instantaneously along the field, effectively making the electric potential uniform within the material. For a material that is perfectly insulating, electrons are immobile, and the electric current within is zero; leaving the electric potential defined by the charge distribution according to Gauss' Law. For most materials subjected to dielectrophoresis, the response to an externally applied electric field is neither that of a perfect conductor nor that of perfect insulator, but rather behaves as a "leaky dielectric" or "lossy dielectric." For harmonic fields, this property of matter is described using a complex, frequency-dependent permittivity, $\tilde{\varepsilon}$ (Eqn. 2.1). A material subjected to an electric field will respond, or polarize, in a manner that is dependent on its complex permittivity as well as the strength and frequency of the local electric field.

$$\tilde{\varepsilon} = \varepsilon - i\frac{\sigma}{\omega} \tag{2.1}$$

Here, i is $\sqrt{-1}$, σ is the conductivity, and ω is the radial frequency of the electric field. The complex permittivity $\tilde{\varepsilon}$ is a function of electric field parameters (magnitude and frequency), thermodynamic parameters (temperature and pressure), and material parameters (composition) [3]. The real and imaginary components of $\tilde{\varepsilon}$ correspond to displacement and conduction current, respectively, and relate respectively to the local-

ization of bound charge and the motion of free charge. The "leaky-dielectric" model implies that when matter within the system reorients or charge redistributes in response to changes in the external electric field, there is a finite "lag" time, which is a function of frequency, between the electric field and the response of a material.

Fundamentally, dielectrophoretic forces (or torques) result from a non-uniform polarization along an interface between materials with different dielectric properties. This implies two things: i) there is an interface between two materials that respond differently to an imposed electric field (described by different values of the complex permittivity, $\tilde{\varepsilon}$) and ii) the imposed electric field varies significantly along this interface [1]. The *Maxwell-Wagner interfacial* polarization takes the form of electric molecular dipoles within the material. The creation of dipoles manifests at the interface between materials of different complex permittivity, due to different relative dipole strengths, as a "bound charge." Bound charge is distinguished from "free charge" in that it manifests itself only in response to an external field and spatial variation in permittivity (*i.e.,* it is induced) and is not free to move through conducting media.

The electric field exerts a Coulomb force on these bound charges, whose sum along the interface is nonzero only when the field is nonuniform. Thus DEP allows a force to be applied to particles as long as the electric field is nonuniform and $\tilde{\varepsilon}$ is different for the particle as compared to its surrounding medium. The frequency dependence of $\tilde{\varepsilon}$ gives experimenters an extraordinary amount of flexibility with regards to what biological particles can be manipulated with DEP, while the favorable scaling of DEP forces as length scales reduce motivates DEP's use in microfabricated systems.

[1] Interestingly, it is also possible to observe a force with a uniform electric field, if the relative complex permittivities vary significantly along the interface.

2.3 Introduction: Theory of Dielectrophoresis

Now we wish to put the above description in mathematical terms that are relevant to the experimental researcher and recapitulate the canonical equations for F_{DEP}. In order to do this, we consider a particle submerged in an electrolyte, each described using complex permittivities ($\tilde{\varepsilon}_p$ and $\tilde{\varepsilon}_m$, for particle and media, respectively), under the influence of a harmonic electric field, $\vec{E}$. The electric field frequency is assumed to be low enough such that the permittivities, ε_p and ε_m, can be considered constant. The electric field is created by applying a potential at some point in the device, and, as expected, we describe the electric field in general as the gradient of this potential:

$$\vec{E} = -\nabla\phi \tag{2.2}$$

and we have made no assumptions yet as to the temporal or spatial properties of the field, except to say that it is harmonic. Owing to the mathematical simplicities stemming from the use of complex algebra in treating these sinusoidal functions, we represent the electric field as:

$$\vec{E}(\vec{r},\omega,\varphi) = \Re\left[\vec{E}_0(\vec{r})e^{j(\omega t+\varphi)}\right] \tag{2.3}$$

where j is $\sqrt{-1}$, $\vec{r}$ is a position vector, $\vec{E}_0(\vec{r})$ captures the spatial distribution of the electric field (still arbitrary), $\Re[\cdots]$ is the real component of the quantity in brackets, and ω and φ are the angular frequency and phase of the field, respectively. In this sort of complex analysis it is common practice to omit the harmonic portion in notation. As long as the system remains linear, and we consider only the steady state, we can continue to use principles of superposition, mesh analysis, and other analytical tools.

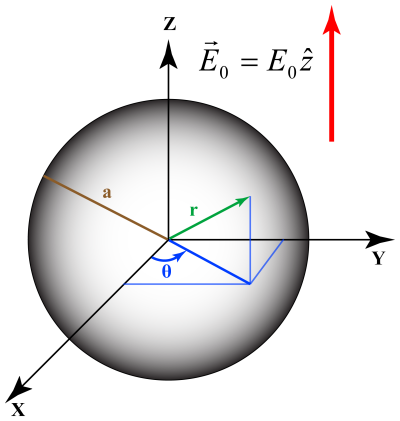

Figure 2.1: A sphere of radius a under the influence of an electric field aligned with the z-axis.

Later, we can include the harmonic portion when we wish to calculate derivatives or time-averages of these harmonic quantities.

Moving forward, we present the basic theory of dielectrophoresis and discuss its limitations. We begin with a brief derivation of the dielectrophoretic force employing the commonly-used dipole approximation for an isolated sphere in an infinite medium. Following this, we expand the discussion to illustrate the limitations of the electrodynamic and fluid-mechanical approximations.

In the most general case, the solution for the electromagnetic force (which includes DEP) on an arbitrary object is found by integrating Maxwell's stress tensor. The Maxwell stress tensor formulation is the most general and powerful, but in problems lacking the appropriate symmetry solutions can only be obtained numerically or as close approximations. For those geometries with suitable symmetry, there are closed-form solutions and approximations available in literature. Relevant analytical [4, 5, 6, 7, 8] and numerical [9, 10, 6, 7, 11, 8, 12] references are summarized in Tables 2.1 & 2.1.

Consider a homogeneous, isotropic sphere in a semi-infinite, homogeneous,

Table 2.1: A brief summary of literature sources that deal with Maxwell Stress Tensor solutions and dielectrophoresis.

No.	*Author. Year*	*Title*	*Technique*	*Application*
[9]	Al-Jarro, A., et al. 2007	Direct calculation of Maxwell stress tensor for accurate trajectory prediction during DEP for 2D and 3D structures.	Numeric	2D and 3D particle trajectories, cell models, cell-cell interactions.
[10]	Jones, T.B. and Wang, K.-L. 2004	Frequency-Dependent Electromechanics of Aqueous Liquids: Electrowetting and Dielectrophoresis	Numeric	Deformation of air-water interface, use of DEP/EWOD for fluid transport.
[6]	Kang, K.H. and Li, D.Q. 2005	Force acting on a dielectric particle in a concentration gradient by ionic concentration polarization under an externally applied DC electric field	Approximate Analytic, Numeric	Concentration polarization force
[7]	Liu, H. and Bau, H.H. 2004	The dielectrophoresis of cylindrical and spherical particles submerged in shells and in semi-infinite media	Analytic	DEP force on a spherical and cylindrical particle
[11]	Liu, Y., et al. 2007	Immersed electrokinetic finite element method	Numeric	Non-spherical particles, particle deformation, numeric technique
[8]	Rosales, C. and Lim, K.M. 2005	Numerical comparison between Maxwell stress method and equivalent multipole approach for calculation of the dielectrophoretic force in single-cell traps	Numeric	DEP force in single-particle traps, non-spherical particles
[12]	Singh, P. and Aubry, N. 2005	Trapping force on a finite-sized particle in a dielectrophoretic cage	Numeric	DEP force on various size particles in a single particle trap

isotropic electrolyte, with an electric field applied along the z-axis, as shown in Figure 2.1. If the external field varies linearly over the characteristic particle dimensions, the polarization of a dielectric sphere in an electric field can be represented by replacing the particle with an equivalent, *effective* dipole located at the center of the particle. Such a dipole consists of two charges of equal magnitude and opposite sign at a position, $\vec{r}$, separated by a vector distance, $\delta\vec{d}$. If the electric field is non-uniform over the dipole length, δd, then the sum for electrostatic forces on the dipole is,

Table 2.1: (Continued).

No.	*Comparison/ Validation*	*Relevant Conclusions*
[9]	effective dipole	MST formulation is necessary when particle size is on the order of electrode size, and particle-particle interactions play a significant role on this length scale
[10]	n/a	MST solution matches experimental behavior for air/water interface. Electrowetting on dielectric is dominant in this case
[6]	numeric solution	MST calculation is used to determine electrical force on a sphere and combined with the hydrodynamic stress tensor to yield net force due to concentration polarization
[7]	effective dipole, numeric solution	Dipole approximation fails when particle size is the same order of magnitude as the characteristic length scale of the electric field. The dipole approximation is worse for a cylinder.
[11]	effective dipole	Dipole approximation becomes increasingly inaccurate as a particle approaches an electrode. MST is used to effectively calculate DEP force and deformation of spheres, CNTs, bacteria, and viruses.
[8]	multipole	The results show that a small number of multipolar terms need to be considered in order to obtain accurate results for spheres. The full MST calculation is only required in the study of nonspherical particles.
[12]	effective dipole	Point dipole model overestimates DEP force by 40% for particles with 10% variation in permittivity and size 25% of electrode size (when particles are "close" to the electrode). As particles approach electrodes or approach electrode size, even the quadrupole term is insufficient.

$$\vec{F} = q\vec{E}(\vec{r} - \overrightarrow{\delta d}) - q\vec{E}(\vec{r}) \tag{2.4}$$

where q is the dipole charge and $\vec{\delta d}$ is the vector from the negative dipole charge to the positive dipole charge, by convention. Expanding the first term in a Taylor series, we obtain:

$$\vec{E}(\vec{r} + \overrightarrow{\delta d}) = \vec{E}(\vec{r}) + \overrightarrow{\delta d} \cdot \nabla \vec{E}(\vec{r}) + \cdots \tag{2.5}$$

If the characteristic length scale of the electric field non-uniformity is large compared to the particle size, then we can neglect terms of higher order in Eqns. 2.5 and substitute Eqn. 2.5 into Eqn. 2.4 to find:

$$\begin{aligned}\vec{F} &= q\overrightarrow{\delta d}\cdot\nabla\vec{E} \\ &= \vec{p}_{\text{eff}}\cdot\nabla\vec{E}\end{aligned} \tag{2.6}$$

Which gives us the force on some unspecified effective dipole moment, but does not intimate how the properties of particle and media contribute to this effective dipole moment. There are several approaches to determine these details; the most common is to examine a homogeneous dielectric sphere in a dielectric media, and solve Laplace's equation for the electric potential inside and outside the sphere, applying the appropriate boundary conditions at the interface. Solution by the separation of variables technique yields Eqn. 2.7 and provides analytical results that are physically intuitive.

$$\vec{p}_{\text{eff}} = -4\pi\varepsilon_m a^3 E_0 \Re\left(\frac{\tilde{\varepsilon}_p - \tilde{\varepsilon}_m}{\tilde{\varepsilon}_p + 2\tilde{\varepsilon}_m}\right) \tag{2.7}$$

$$\langle F_{DEP}\rangle = \pi\varepsilon_m a^3 \Re\left[f_{CM}\right]\nabla\left(\vec{E}_0\cdot\vec{E}_0\right) \tag{2.8}$$

$$f_{CM} = \frac{\tilde{\varepsilon}_p - \tilde{\varepsilon}_m}{\tilde{\varepsilon}_p + 2\tilde{\varepsilon}_m} \tag{2.9}$$

where $\vec{p}_{\text{eff}}$ is the effective dipole moment for a sphere, a is the particle radius, ε_m is the permittivity of the media, $\tilde{\varepsilon}_p$ and $\tilde{\varepsilon_m}$ are the complex permittivities of the particle and media, respectively, and $\Re\left[f_{CM}\right]$ is the real part of the Clausius-Mossotti factor. This analytical expression for dielectrophoretic effects is intuitive, tractable, and is applicable under numerous experimental condition (limitations on the applicability of this form of F_{DEP} will be discussed in §2.3.1). If we expand this analysis to a general electric field with spatially varying phase, we find an additional term that leads to electrorotation effects:

$$\langle \vec{F}_{DEP} \rangle = \pi a^3 \varepsilon_m \Re[f_{CM}] \nabla (\vec{E} \cdot \vec{E}) - 2\pi a^3 \varepsilon_m \Im[f_{CM}] \nabla \times \Re[\vec{E}] \times \Im[\vec{E}] \tag{2.10}$$

The first term in this equation is the well-known result for the time-averaged dielectrophoretic force, and appears in the presence of any non-uniform electric field (of the form prescribed). The second term arises only in the presence of a spatially non-uniform electric field phase, $\varphi \neq 0$, and is the driving term for traveling-wave dielectrophoresis (twDEP). In both terms, forces scale with particle radius cubed, making particle size an important factor in most DEP experiments.

2.3.1 Limiting Assumptions and Typical Experimental Conditions

Though seldom explicitly defined in the literature, there are clear boundaries for the applicability of the dielectrophoretic force equations presented above. Particle shape, characteristic particle dimensions and device length scale, particle concentration, and characteristic length scale of changes in the electric field must be considered[2].

We will examine each of these parameters as variations from our "baseline case" (Eqn. 2.10): a sparse concentration of homogeneous, spherically symmetric particles in an infinite domain, under the influence of an electric field that is well approximated by a first order linearization. We will consider, as they affect dielectrophoretic forces and torques:

i. The limits of the spherical approximation, as particle shape deviates from sphericity and the dipole approximation fails.

[2]Throughout this chapter, however, we will continue to make the assumption that the double layer thickness (Debye length, λ_D) is small in comparison to channel and particle dimensions.

ii. The limits of the dipole approximation as the length scale of variations in the electric field decreases — due to shrinking channel dimensions, shrinking inter-particle spacing, or increasing particle size — and our linearization of the electric field fails.

iii. The limits of the effective permittivity model, and the Maxwellian equivalent body, as particle composition becomes increasingly complex.

We will also consider, as they affect drag forces and terminal particle velocity:

i. The limits of the spherical approximation, as particle shape deviates from sphericity and the drag coefficient takes on a different form.

ii. The limits of the isolated particle approximation, as particle concentration increases.

iii. The limits of the infinite domain assumption, as channel dimensions decrease.

Assumptions and Approximations for F_{DEP}

Spherical Approximation While many of the particles in DEP experiments are not spherical, the spherical approximation, and the simple multi-shell models associated with it, are often used. Spherical symmetry leads to analytical solutions that are intuitive and easy to apply. There are, however, situations where these approximations are inappropriate, e.g., cellular samples of rod-shaped bacteria. We will present analytical solutions for the dipole moment of a elliptical particle and compare this result to the spherical moment presented earlier (Eqn 2.7). In all of these cases we will assume that the major axis of our ellipsoidal particle will be aligned with the applied electric field

and that the field varies only along this direction; a reasonable assumption for isotropic particles in non-rotating fields[3].

The shape of a polarized particle will influence the electric field it creates. As particle shape deviates from spherical, the applicability of the equivalent dipole representation based on a spherical particle rapidly decreases. Consider a prolate ellipsoidal particle with a long axis, a_1, and equivalent minor axes, $a_2 = a_3$. In general, the effective dipole moment will have three components, one along each axis due to the variation of the electric field along that axis. We have assumed that the particle aligns instantaneously with the field, and that the field varies only along the major axis. In this case, the effective dipole moment will be:

$$\begin{aligned} \vec{p}_{\text{effective},1} &= 4\pi a_1 a_2 a_3 \varepsilon_m \tilde{f}_{CM,1} \tilde{E}_{0,1} \\ \tilde{f}_{CM,1} &= \frac{\tilde{\varepsilon}_p - \tilde{\varepsilon}_m}{3\left[\tilde{\varepsilon}_m + (\tilde{\varepsilon}_p - \tilde{\varepsilon}_m) L_1\right]} \\ L_1 &= \frac{a_2^2}{2a_1^2 e^3}\left[ln\left(\frac{1+e}{1-e}\right) - 2e\right] \\ e &= \sqrt{1 - \frac{a_2^2}{a_1^2}} \end{aligned} \tag{2.11}$$

where the subscript 1 denotes a component along the 1 axis[4]. $\vec{p}_{\text{effective},1}$ is the effective dipole moment in the 1-direction. $f_{CM,1}$ is the Clausius-Mossotti factor from our previous representations, but now depends on the axis under consideration. L_1 is the "depolarization factor" along the 1-axis [13].

Under typical experimental conditions ($E_0 = 1V/\mu$m, $2\pi\omega = 1$MHz, $f_{CM} = 0$ when

[3] A particle consisting of an isotropic material (or an effectively isotropic material as will be discussed later in §2.3.1)will obtain three effective moments along its major and semimajor axes and experience a torque on each moment. For isotropic materials, the major axis has the largest moment, leading to a torque that will align the major axis with the external field.

[4] For Cartesian coordinates 1 corresponds to $\{x, y, z\}$

Table 2.2: Typical experimental conditions used to calculate errors associated with the spherical approximation.

Material Property	*Value*
ε_m	$80\varepsilon_0$
ε_p	$2.6\varepsilon_0$
σ_m	$5.5\mu S/m$
σ_p	$100\mu S/m$

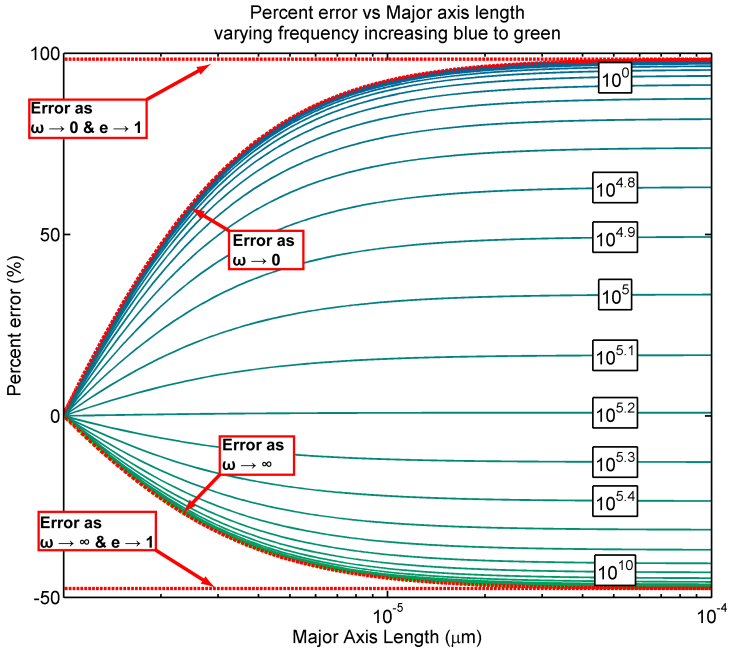

Figure 2.2: Percent error (colorbar) between the effective dipole moments for a spherical and an ellipsoidal particle. Parameters are listed in Table 2.2. Limiting cases are also plotted (red, - -).

$2\pi\omega = 0.1$MHz, $a_2 = a_3 = 1\mu$m), for a prolate ellipsoid with complex permittivity shown in Table 2.2, a 30% variation in major axis length leads to 10% error in the effective dipole moment. This error quickly rises to 50% as the aspect ratio of the ellipse approaches 2:1 (Figure 2.2). In the limiting case of a long, thin, ellipsoid ($e \rightarrow 1$), the relative error between the real f_{CM} and the spherical approximation thereof can be shown to be equal to the spherical approximation of f_{CM}, so the relative errors of the spherical approximation approach zero near crossover points, and can range from 1 to -0.5.

While the errors associated with the spherical approximation can be large, it remains a valuable tool for a first-pass at device design, especially in applications of sorting, screening, or trapping where subtle variations in the magnitude of polarization response are unimportant. In particular, the addition of multipoles and ellipsoidal adjustments does not alter the behavior of the *sign* of f_{CM}.

When performing ROT or DEP spectra experiments in an attempt to draw conclusions about particle structure or composition, a practice common in biological assays, spherical models are generally insufficient — ellipsoidal, cylindrical, or spheroidal models are available and allow for more accurate structural inferences.

Dipole Approximation When considering the electric field produced by a polarized particle of spherical shape, the characteristic length scale of the system is important. Since higher-order multipole effects drop off more rapidly than dipole fields, the field produced by a nonspherical particle becomes equal to that produced by a spherical particle as the distance from the particle center increases. Close to the particle, however, the effects of higher-order multipoles are apparent. As the characteristic length scale of the device, shrinks, owing to reductions in channel dimensions or increases in particle concentration, the contributions of higher-order multipoles becomes significant. Additional multipoles are also important when considering rapidly varying electric fields and non-spherical particles. Several different geometries have been considered in detail in the literature [7, 14, 15, 16, 17, 18, 19, 20, 8]. A selection of these references is summarized in Tables 2.3 and 2.3.

The characteristic length scale of the particle and electric field under consideration must be examined to evaluate the applicability of classical DEP representations such as that shown in Eqn. 2.7. When the electric field varies significantly over the length

Table 2.3: A brief summary of literature sources that deal with multipole moment solutions and particles of various geometries in dielectrophoresis.

No.	*Author. Year*	*Title*	*Technique*
[7]	Liu, R.M. and J.P. Huang. 2004	Theory of the dielectrophoretic behavior of clustered colloidal particles in two dimensions	Multiple image method, Maxwell-Gannet approx, 2D
[14]	Castellarnau, M. et al. 2006	Dielectrophoresis as a tool to characterize and differentiate isogenic mutants of Escherichia coli	Multishell, prolate spheroid
[15]	Ehe, A.Z. et al. 2005	Bioimpedence spectra of small particles in liquid solutions: Mathematical modeling of erythrocyte rouleaux in human blood	Approximate
[16]	Gimsa, J. 2001	A comprehensive approach to electro-orientation, electrodeformation, dielectrophoresis, and electrorotation of ellipsoidal particles and biological cells	Analytic, numeric
[17]	Gimsa, J. et al. 1994	Dielectric-Spectroscopy of Human Erythrocytes - Investigations under the Influence of Nystatin	Analytic, experimental
[18]	Green, N.G. and T.B. Jones. 2007	Numerical determination of the effective moments of non-spherical particles	Analytic, numeric

scale of the particle, then, in order to model the induced moment, we must replace the particle with an equivalent multipole. Green and Jones [18] compare the results from up to 9 moments to analytical solutions for spheres and ellipsoids, and show that higher order moments are necessary to accurately obtain equivalent potential solutions for non-spherical particles.

While multipolar solutions are necessary when attempting to determine the effective moment or potential field surrounding a particle, the spherical approximation retains significant utility in estimating particle behavior in many experimental settings. The application of these approximations should be undertaken with care in light of the ultimate goal of the experiment. When using DEP for transport, trapping, or screening, the spherical approximation often leads to uniform errors (which are obfuscated by experimental uncertainties) and the qualitative correctness of the spherical approximation

Table 2.3: (Continued).

No.	*Application*	*Relevant Conclusions*
[7]	The effective f_{CM} of isolated and randomly clustered spherical and cylindrical particles.	For closely spaced particles (clusters) an effective dipole factor can be defined based on the MIM and MGA.
[14]	An ellipsoidal, multishell model of *E. coli* was used to determine the differences between isogenic mutants.	Experimentally distinguished DEP characteristics of isogenic mutants. Presented a confocal, multishell, ellipsoid model for f_{CM}.
[15]	Erythrocyte dipole moments are modeled using a short-cylinder model as an approximation	Dielectrophoresis of erythrocytes is predicted using the short-cylinder model for field frequencies between 10^7 and 10^8Hz.
[16]	Traditional formulations for DEP and ER with numeric techniques allow for consideration of the interaction of these phenomena	Predicts a discontinuous electrorotation spectra due to the influence of dipole moments along the three coordinate axes.
[17]	Ellipsoidal dielectrophoretic and electrorotation spectra more accurately explained experimental data.	The use of ellipsoidal dielectric models of DEP and ER resulted in more accurate interpretation of results. Changes in cell dielectric properties was observed after 5min of experimentation, a fact that should be considered by other researchers.
[18]	Higher order moments for various particle geometries are calculated. Particle shapes include sphere, oblate- and prolate-ellipsoids, cylinder, and erythrocyte.	Higher order moments can be used to more accurately determine the DEP force, and are particularly important in the case of non-spherical particles. In addition, the approximation of short-cylinders using prolate spheroids in particularly poor in light of the multipolar analysis.

often suffices. In screening or electrorotation studies that depend critically on the magnitude of induced polarization, however, the spherical approximation should be examined critically for accuracy with relations analogous to the one plotted in Figure 2.2.

Maxwellian Equivalent Body An axisymmetric, anisotropic particle can be well-approximated by replacement with a particle with an effective, isotropic, complex permittivity — the Maxwellian equivalent body [21]. Many models assume a homogenous, isotropic (equivalent) material, and in so doing, also assume that particle structure or isotropy is unimportant. For certain applications, this is true — e.g., separations and trapping applications where these components are not of interest — but when at-

tempting to predict behavior (rather than measure) or gain insight into changes in internal structure, particle anisotropy can affect particle response through changes in $\tilde{\varepsilon}_{\text{eff}}$ [22, 23, 24, 25, 26, 27, 28, 29, 30, 17, 31, 32][5]. The complex permittivity, as we have defined previously, applies for isotropic materials only. In general, the permittivity takes on a tensorial character, $\vec{\vec{\varepsilon}}$. We can define our coordinate axes to coincide with the principal axes of $\vec{\vec{\varepsilon}}$, and in so doing, obtain a diagonal matrix. Furthermore, the work of Simeonova et al [21], showed that the Maxwellian equivalent body can be used in cases where the anisotropy is axisymmetric, yielding:

$$\tilde{\varepsilon}_{\text{eff}} = \tilde{\varepsilon}_{1,\text{effective}}\frac{E_1}{|E|} + \tilde{\varepsilon}_{2,\text{effective}}\frac{E_2}{|E|} + \tilde{\varepsilon}_{3,\text{effective}}\frac{E_3}{|E|} \tag{2.13}$$

In the specific case where the electric field is linear and along the direction of the major axis, the permittivity tensor will reduce to a scalar component along the direction of the field.

Assumptions and Approximations for F_{drag}

Spherical Approximation In order to determine the velocity of a particle undergoing DEP, we consider equilibrium between the DEP force and the viscous drag. For low Reynolds number, the viscous drag is given by

[5]These references primarily consider electrorotation phenomena, rather than transport by dielectrophoresis. However, electrorotation spectra and dielectrophoretic spectra are related by the Kramers-Krönig relationships:

$$\begin{aligned}\Re[f_{CM}(\omega)] &= \frac{2}{\pi}\int_0^\infty \frac{x\Im[f_{CM}(x)]}{x^2-\omega^2}dx + \Re[f_{CM,\infty}] \\ \Im[f_{CM}(\omega)] &= \frac{2}{\pi}\int_0^\infty \frac{\Re[f_{CM}(x)]-\Re[f_{CM,\infty}]}{x^2-\omega^2}dx + \Re[f_{CM,\infty}]\end{aligned} \tag{2.12}$$

where $f_{CM,\infty}$ is the limit of the complex Clausius-Mossotti factor as $\omega \to \infty$ [13].

$$F_{\text{drag}} = \frac{1}{2}\rho u^2 A_p C_D \tag{2.14}$$

$$C_{D,\text{sphere}} = \frac{24}{Re} \tag{2.15}$$

$$F_{\text{drag}} = 6\pi\mu u a \tag{2.16}$$

where $A_p = \pi d^2/4$ is the particle cross sectional area perpendicular to the direction of flow, $d = 2a$ is the particle diameter, $Re = \rho u d/\mu$ is the particle Reynolds number, and C_D is the drag coefficient. We also know the analytical form of the DEP force and can balance this against the drag force to give the velocity at equilibrium:

$$F_{DEP} = \pi\varepsilon_m a^3 \Re\left[f_{CM}\right] \nabla\left(\vec{E}\cdot\vec{E}\right) = F_{\text{drag}} \tag{2.17}$$

$$\pi\varepsilon_m a^3 \Re\left[f_{CM}\right] \nabla\left(\vec{E}\cdot\vec{E}\right) = \frac{1}{2}\rho u^2 A_p \frac{24\mu}{\rho u d} \tag{2.18}$$

$$u = \frac{\varepsilon_m a^2}{6\mu} \Re[f_{CM}] \nabla\left(\vec{E}\cdot\vec{E}\right) \tag{2.19}$$

We use an equilibrium relation because the characteristic equilibration time (the time for particles to reach their terminal velocity) is very short compared to experimental time scales. The constant term that relates the dielectrophoretic force to the resulting particle velocity, then, is termed the "dielectrophoretic mobility":

$$\mu_{DEP} = \frac{\varepsilon_m a^2}{6\mu} \Re[f_{CM}] \tag{2.20}$$

When a particle is not spherical, however, the expression for drag coefficient changes as a function of particle shape and orientation. This variation is expressed through changes in both A_p, the cross-sectional area perpendicular to the flow, and C_D, the drag

coefficient based on an *effective* particle diameter. The effective particle diameter is the diameter of a sphere of equivalent volume. For isotropic materials, particles will typically orient with their long axis parallel to the external electric field.

Consider an ellipsoid with axes a_1, a_2, and a_3 ($a_1 > a_2 > a_3$). The dipole moment of such a particle can be broken up into components along each axis. Moments will be proportional to the effective permittivity (along a particular direction) and the electric field along a particular direction.

$$p_i \sim \vec{\varepsilon} \cdot a_i \vec{E} \cdot \hat{a}_i \tag{2.21}$$

p_i is the dipole moment vector along the axis $i = \{1,2,3\}$, $\vec{\varepsilon}$ is the permittivity, $\vec{E}$ is the electric field, and $\hat{a}_i$ is a unit vector along one of the axes $\{1,2,3\}$.

For a non-rotating electric field, the particle will experience torques along each moment, tending to align the particle to the sum of moments. In a rotating electric field, there is still a torque on the particle, however, and orientation is a function of the frequency of rotation in addition to the factors determining the magnitude of torque on each moment of the particle [16].

For the viscous drag on a particle, we present approximate analytic results from [33] for the special case of a prolate spheroid ($a_1 > a_2 = a_3$) — useful due to its similarity to rod-shaped particles:

$$C_{D,\text{ellipse}} = \frac{128}{Re} \frac{(1-e^2)e^3}{2e + (3e^2-1) ln\left(\frac{1+e}{1-e}\right)} \tag{2.22}$$

where we have again used the eccentricity, $e = \sqrt{1 - a_2^2/a_1^2}$. The resulting dielec-

trophoretic mobility for prolate spheroid with its long axis parallel to the direction of the applied electric field is found by combining Eqns. 2.22, 2.11, and 2.6:

$$\mu_{DEP} = \left(\frac{2e + (3e^2 - 1) ln\left(\frac{1+e}{1-e}\right)}{e^3} \right) \frac{a_1 a_2}{24} \frac{\varepsilon_m}{\mu} \left(\frac{\tilde{\varepsilon}_p - \tilde{\varepsilon}_m}{\tilde{\varepsilon}_m + (\tilde{\varepsilon}_p - \tilde{\varepsilon}_m) L_3} \right) \tag{2.23}$$

$$L_3 = \frac{a_2^2}{2a_1^2 e^3} \left[ln\left(\frac{1+e}{1-e}\right) - 2e \right]$$

The first term in parentheses contains geometric corrections to the drag coefficient and in the second term, these corrections are made by including L_3.

For a rod-shaped bacterium with a 2:1 major/minor axis ratio, the electrodynamic correction is on the order of 20–40% far from the crossover point, while the drag correction is roughly 60%.

Infinite Domain Assumption In many fluid mechanics and electromagnetics problems, it is common to invoke "boundary conditions at infinity." For instance, it is useful to argue that as distance from the origin goes to infinity, a parameter of interest (such as velocity potential or electric potential) must converge to an externally imposed value. However, in applications where channel dimensions approach the particle diameter, this assumption is typically poor. The electrodynamics of the problem is influenced by the proximity of the boundaries on the Laplace equation, requiring more terms in the multipole expansion, while the drag relation is influenced by the proximity of the boundaries on the Stokes flow equations, requiring drag adjustments.

As a particle moves through the surrounding fluid, it will exert a pressure on the surrounding fluid. We will consider only incompressible fluids, and so, this pressure will be transduced to fluid velocity. Solutions to the fluid velocity field produced by

a moving particle in an infinite fluid are readily available. However, as the moving particle approaches a wall, the fluid velocity field resulting from the moving particle will be retarded due to the no-slip boundary condition at the wall. When the force, $\vec{F}$, on a particle is directed parallel to the wall, the terminal particle velocity is modified by the scalar coefficient, B:

$$\vec{u} = \frac{B}{6\pi\eta a}\vec{F} \tag{2.24}$$

The scalar coefficient, B, decays to 0 as $x \to a$, and approaches 1 for $x > 10a$. A plot of the mobility coefficient shows the retarding effects of the wall as x increases [34]. At distances greater than one particle radius, the scalar coefficient, B, can be approximated as:

$$B = \left[1 - \frac{9}{8}\frac{a}{x} + \frac{1}{2}\left(\frac{a}{x}\right)^3 + \ldots \mathrm{O}\left(\left(\frac{a}{x}\right)^5\right)\right]^{-1} \tag{2.25}$$

Isolated Particle Assumption As with the infinite domain assumption discussed above, the assumption that particles are isolated in a media may break down at low interparticle spacing distances, caused by high particle concentrations or by particle localization due to hydrodynamic and/or electrokinetic forces. We examine briefly the results of Batchelor [36] and Goldman et al [37], with regard to two interacting spheres. The equation of relative motion is:

$$\frac{d\vec{r}}{dt} = (\vec{\mu}_{2,1} - \vec{\mu}_{1,1}) \cdot \vec{F}_1 + (\vec{\mu}_{2,2} - \vec{\mu}_{1,2}) \cdot \vec{F}_2 \tag{2.26}$$

$$\vec{\mu}_{i,j} = \frac{1}{3\pi\eta(a_i + a_j)}\left[A_{i,j}\frac{\vec{r}\vec{r}}{r^2} + B_{i,j}\left(\vec{\vec{I}} - \frac{\vec{r}\vec{r}}{r^2}\right)\right] \tag{2.27}$$

where $\vec{r}$ is the vector between particle centers, r is the magnitude of $\vec{r}$, $\vec{\vec{I}}$ is the identity tensor, $A_{i,j}$ and $B_{i,j}$ are scalar coefficients that depend on r, and $\{i, j\}$ refer to sphere 1 or sphere 2. Batchelor found that $A_{1,1}$, $A_{2,2}$, $B_{1,1}$, and $B_{2,2}$ decrease sharply as the distance between particles decreases and increase to 1 as $r/a \to 10$. These coefficients correspond to mathematical contributions to the mobility of one particle or the other. The interaction terms, $A_{1,2}$, $A_{2,1}$, $B_{1,2}$, and $B_{2,1}$ decay slowly compared to the rate of increase of $A_{i,i}$ and $B_{i,i}$, but still decay to zero as r grows beyond 10 radii. The importance of these correction factors again comes into play when particle distances are less than 10 times the radius. Since the average particle spacing normalized by the radius is approximately $\sqrt[3]{4\pi/(3\rho)}$, where ρ is the volume fraction of monodisperse particles, these effects are safely neglected at local volume fractions below 0.4%.

2.4 Materials: Equipment for Generating Electric Field Nonuniformities and DEP forces

There are myriad different DEP devices and techniques, so much so that dividing them cleanly into categories proves difficult. The dielectrophoretic effect is fundamentally tied to the electric fields, which can be defined by spatial and temporal characteristics, and so we choose to divide DEP approaches by spatial and temporal characteristics accordingly. We will consider DC or sinusoidal AC fields[6], with variations in temporal (frequency, phase) and spatial (geometry) character, as they relate to the generation of DEP forces.

[6]It is entirely possible to create DEP forces using non-sinusoidal fields, but this is rarely done. A mathematical treatment of these fields is slightly more difficult, and is usually done via Fourier analysis — treating a non-sinusoidal field as a sum (or integral) of sinusoidal fields. We can therefore intuit the properties of non-sinusoidal fields with appropriate knowledge of the frequency response characteristics of sinusoidally-driven DEP forces and the spectral composition of the non-sinusoidal field.

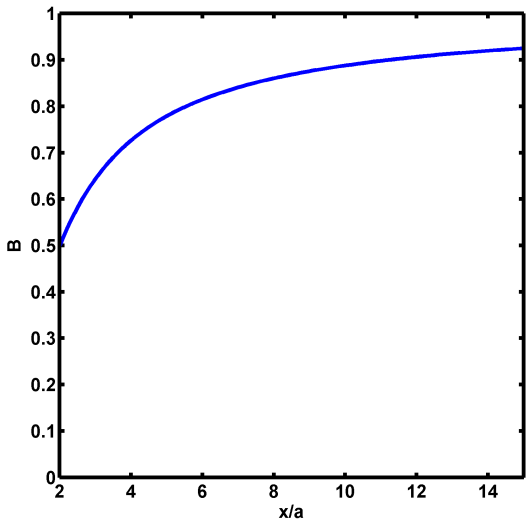

Figure 2.3: Results from [35] show the value of the mobility coefficient, B, as distance from the wall increases. The wall distance has been normalized by the particle radius.

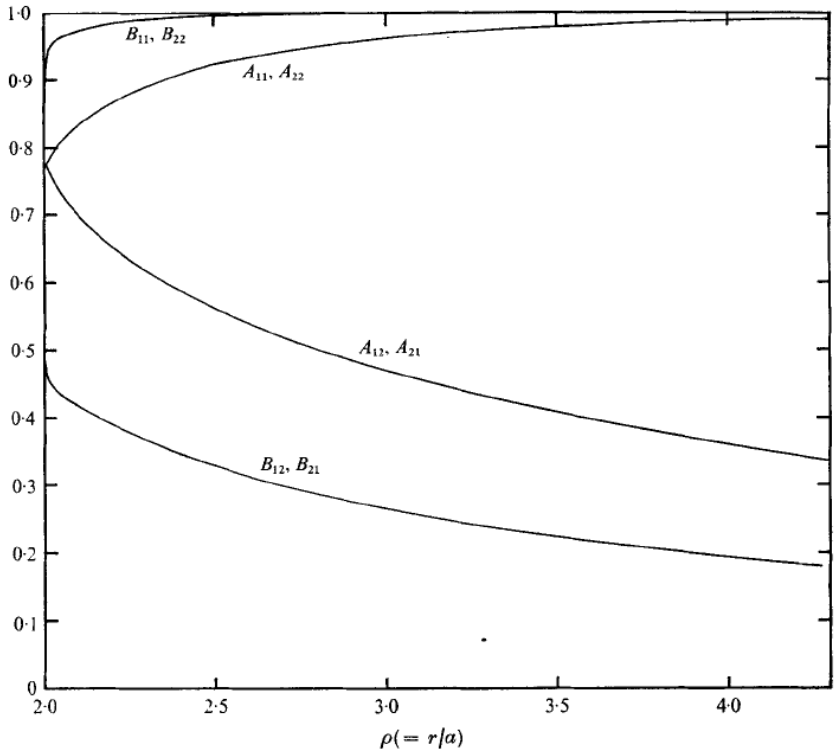

Figure 2.4: Results from [36, 38] show the value of the mobility coefficients, $A_{i,j}$ and $B_{i,j}$, as inter-particle spacing increases. The inter-particle distance has been normalized by the particle radius.

2.4.1 Electric Field Frequency

The frequency dependence of DEP force is perhaps its most alluring feature, and as a result, the majority of DEP techniques employ sinusoidally varying electric fields.

AC Fields

AC electric fields are the primary field type employed in dielectrophoresis applications, owing to the availability of straightforward analysis and experimental implementation techniques. AC fields of high frequency ($> 10^3$Hz) can be safely applied to microfabricated electrodes in microfluidic channels without significant build-up of electrolytic products (hydrogen and oxygen bubble production at the anode and cathode, respectively), significant changes in temperature, or significant changes in pH.

Equipment and Experimental Setup The most common and straightforward method for generating a sinusoidal AC electric field is to employ a function generator connected to electrodes. Function generator performance can range from low to high according to the experimental requirements. Higher quality instruments offer finer control over the characteristics of the output waveform (phase, frequency, amplitude) and offer a wider range of operating parameters, achieving higher frequency and power output. The power output of these devices is typically low, on the order of milliwatts for frequencies in the kilohertz range, and tends to decrease as frequency increases beyond one megahertz. These limitations are primarily the result of component slew rate limitations, which will be higher as performance (and cost) increase. In the kilohertz and megahertz range, it is common for generators to offer a DC-offset option, which will allow for the simultaneous use of AC and DC electric field components. This has been utilized by some

experimenters to actuate DEP and electrophoresis/electrosmosis independently [39].

In general, the DEP frequency response characteristic extends beyond the megahertz range, and for experimental applications requiring field frequencies in the gigahertz range, an RF signal generator must be used.

These signal generators work quite well for low power applications, where microfabricated electrodes are used and can generate high electric field gradients due to their close proximity. There are situations where higher voltage signals must be applied, such as in insulative dielectrophoretic applications, where electrode spacing is necessarily orders of magnitude larger, requiring concomitant increases in applied voltage. General amplification of arbitrary signals is possible for low frequency ($\sim$ 1kHz) signals at a reasonable cost [39]. In order to amplify higher frequency, arbitrary signals (including a DC-bias) to the kilovolt range, more specialized equipment is currently required. Amplification of high frequency *sinusoidal* waveforms can be accomplished using RF-amplification equipment.

In this discussion, we have concerned ourselves with only sinusoidal or DC signals, but this does not represent the limits of possible waveforms. Indeed, some researchers have shown that the addition of multiple frequency components (or the higher frequency spectral distributions present in sawtooth, square, or triangular waveforms) can be beneficial to a particular DEP application [40]. Most function generators can generate these waveforms; more complex waveforms, however, require an arbitrary waveform generator.

DC Fields

While the majority of DEP approaches use sinusoidally varying electric fields with relatively high frequencies, recent advances in microfabrication techniques have made spatial variation of the electric field magnitude possible on relevant length scales (typically in insulative-DEP techniques; see §2.4.3) and opened the door to the applications of low- and zero-frequency electric fields. DC fields are interesting because they allow combination of linear and nonlinear EK effects and offer simplified analysis and straightforward implementation.

Equipment and Experimental Setup DC electric fields offer simplicity of implementation, and combine transport of fluid and particles via electroosmosis and electrophoresis. DC electric fields drive electrophoresis and electroosmosis by the familiar mechanisms, and can also drive dielectrophoresis (see §2.4.3 for an explanation of the mechanism). This combination is convenient, as it allows analyte transport and manipulation with only one field.

DC fields will tend to drive larger currents and lead to the production of electrolytic products at electrode interfaces. For this reason, DC dielectrophoresis applications are typically carried out by placing insulating constrictions in the electric current path and electrodes in external reservoirs, allowing the electrolytic products to escape to the atmosphere [41, 39]. Brask et al, in a non-DEP application, employ palladium electrodes, taking advantage of the high hydrogen permeability of palladium to minimize hydrogen bubble formation at the electrode surface.

Driving DEP via DC fields from external reservoirs usually requires high voltages. These can be generated and controlled relatively easily with a DC high voltage power

supply, though the electrical resistance of the channel should be considered when planning for power and thermal management of the system. A short, wide channel filled with high conductivity buffer (such as 1M phosphate buffered saline) will have a low electrical resistance. This will lead to a larger current draw from the power supply, increased rates of electrolysis, and increased Joule heating. Lower conductivity solutions and long, narrow, shallow channels will ameliorate these difficulties. As electrophoresis and electroosmosis are both dependent on $\vec{E}$ and dielectrophoresis is dependent on $\nabla(\vec{E}\cdot\vec{E})$, these effects can be tuned independently using the field magnitude and the geometry of the device (specific geometries and fabrication techniques will be discussed in detail in §2.4.3).

2.4.2 Electric Field Phase

In addition to the field frequency, the phase (and the spatial variation of phase) can be used in system design as well. If the electric field phase (φ) is spatially uniform, then it can be neglected when calculating steady-state dielectrophoretic effects. However, when the phase is spatially nonuniform, additional force and torque components exist, which open up a wider range of possible applications and measurements.

One particularly useful method for taking advantage of spatial variations in phase is what has become known as "traveling-wave" dielectrophoresis (twDEP), which uses a spatially-varying phase to propel particles down a channel. Recall from §2.3 Eqn. 2.10, that the dielectrophoretic force contains two components: the irrotational, "traditional" dielectrophoresis component and the curl dependent, "traveling-wave" dielectrophoresis component.

The canonical example of twDEP is to use an array of electrodes patterned in a

microfluidic channel. The electrode array is composed of alternating, independently driven electrodes with different phase. The electrode array is aligned at an angle to the direction of flow. These signals — irrespective of phase — are used to levitate particles against gravity within the flow field due to irrotational, negative dielectrophoresis, and the varying phase is used to drive particles transverse to the direction of flow according to the imaginary component of the Clausius-Mossotti factor.

In much the same way that spatially varying phase leads to traveling wave dielectrophoresis, a rotating electric field will induce a particle "electrorotation" response. In this case, the dielectrophoretic effect is instead expressed as a torque and is dependent on a different aspect of the particle's electrical properties, namely the imaginary component of the Clausius-Mossotti factor ($\Im\left[F_{CM}\right]$).

$$\langle \tau \rangle = -4\pi\varepsilon_m a^3 \Im[f_{CM}] \left(\Re[\vec{E}] \times \Im[\vec{E}] \right) \tag{2.28}$$

The results of an electrorotation experiment typically consist of measured particle rotation rates as a function of electric field rotation frequency, or "ROT spectra." ROT spectra are related to DEP spectra by the Kramers-Krönig relation (Eqns. 2.12), and thus ROT spectra have large magnitudes at the frequencies where DEP forces are changing.

Equipment and Experimental Setups Creating spatially varying phase signals in microfluidic systems is most often accomplished using arrays of interdigitated electrodes (see Figure 2.5. By applying a different phase to various electrodes in an array, a spatially varying field is produced. The electrode array itself is often fabricated at an angle to the microfluidic channel, because the twDEP forces that are created drive particles perpendicular to electrode orientation. This configuration leads to sorting as a function of the imaginary component of the Clausius-Mossotti factor transverse to the direction

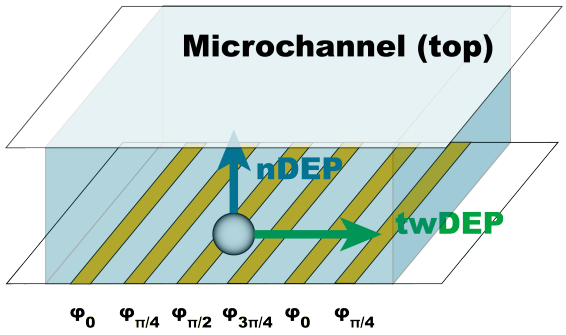

Figure 2.5: Configuration and forces in a twDEP electrode array.

of flow:

The electric signals applied to elements of the electrode array generally consist of four sinusoidal signals with phase magnitudes $\varphi = 0$, $\pi/2$, π, and $3\pi/2$, in order. This ABCD-configuration effectively generates an electric field maximum that propagates perpendicular to the array at a frequency equal to the driving frequency. Chang et al. showed that separating particles with similar (but distinct) $f_{CM}(\omega)$ functions via twDEP techniques can be improved by using two (or more) signals simultaneously, with different frequency. The first frequency is chosen to optimize the levitation of particles above the electrodes (i.e. $\Re[f_{CM}(\omega)] < 0$ for both particles), and the second is chosen to optimize the transport of particles along the array as a function of $\Im[f_{CM}(\omega)]$[40].

The design and fabrication of twDEP devices is slightly more challenging than simpler electrode configurations because of the need for four different signal paths. This requires multilayer fabrication techniques, but these are well understood and can be readily accomplished in appropriate clean-room facilities.

Rotating electric fields can be created by forming a quadrupolar configuration and driving each electrode at a different phase (again, $\varphi = 0$, $\pi/2$, π, and $3\pi/2$ form the components of the ABCD configuration). Fabrication of these devices is single-layer process, and can be accomplished using standard photolithographic techniques. How-

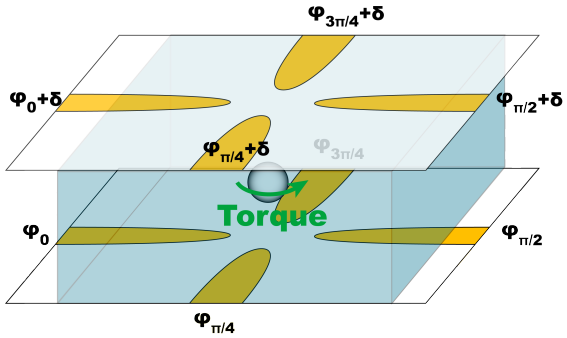

Figure 2.6: An octode cage used for electrorotation studies.

ever, the planar quadrupolar configuration can induce nDEP and force particles away from the electrodes (in the z-axis direction, if the electrodes are in the x-y plane). Particles will then be out of the range of influence of the electrodes or trapped against the microchannel wall, inducing a force that can confound a ROT spectra analysis. This difficulty has been overcome by using an octode cage, such as that shown in Figure 2.6: two planar, quadrupolar electrode arrays are assembled facing one another, displaced in the z-axis direction [42]. This configuration creates an electric field null in the center of the three-dimensional configuration. This is effective for trapping, but a field null yields no net torque. In order to conduct the electrorotation study, one quadrupolar array is offset by a few degrees (rotated about the z-axis in space or by adding a phase increment between the signals driving the quadrupolar arrays), creating a minimum, not a null, in the center of the octode cage [42, 43].

In short, electrorotation and twDEP are two useful techniques that depend on the phase of the electric field and the imaginary component of the Clausius-Mossotti factor, $\Im[f_{CM}]$. Electrorotation studies can be used to gain a large amount of information about an individual particle. ROT spectra can be used to determine $\Im[f_{CM}]$, and $\Re[f_{CM}]$ can be found via the Kramers-Krönig relationships (Eqns. 2.12). Quadrupolar arrays and other ROT measurement techniques work well for single particle studies, but have low throughput, making them inappropriate for sorting applications. twDEP has been

used to successfully separate particles transverse to the direction of fluid flow, making it an effective continuous-flow sorting technique. Combined with multiple frequencies, twDEP can be applied to a wide range of experimental conditions, with judicious choice of the driving waveform [40].

2.4.3 Geometry

The temporal aspects (frequency and phase) of electric fields in DEP systems are, of course, critical. However, the magnitude of the DEP force in micro- and nanoscale systems is central to DEP's burgeoning importance in the last 10 years. Micro- and nanofabrication techniques have opened the door to applications of dielectrophoresis at the cellular length scale, where subtle variations in particle composition and changes in the dielectrophoretic response can be observed on a particle by particle basis. By altering the geometry of energized electrodes or the channel boundaries that define the electric current path, dielectrophoretic effects can be tuned for numerous applications.

Electrode Configurations

As previously discussed, changing the shape and orientation of electrodes, in addition to modulating the frequency and phase applied, can give rise to dielectrophoretic particle trapping, dielectrophoretic sorting, electrorotation, and traveling wave dielectrophoresis effects. Specific geometries will be discussed in the experimental methods section (§2.5).

Castellanos, et al. examined the case of two adjacent electrodes in detail in [44]. Their results detail the relative effects of DEP and hydrodynamics on the motion of

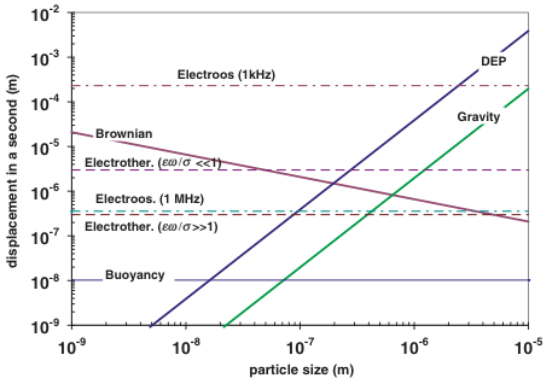

Figure 2.7: Scaling relationships developed in [44] show the relative effects of bouyancy, Brownian motion, electroosmosis, electrophoresis, and dielectrophoresis. Electrodes are separated by 25μm and energized with a 5V potential.

particles adjacent to the electrode array (Figure 2.7). The electrodes were energized with a 5V potential and separated by a distance of 25μm. Their findings concluded that, in general, motion due to gravity and dielectrophoresis vary with particle volume, and dielectrophoresis will dominate provided an appropriate electric potential is chosen (frequency and magnitude). Brownian motion decreases with increasing particle size, depending on $1/a$. For particle sizes in the micron regime, this can be overcome by dielectrophoresis with a relatively low electric field. A similar argument can be made for the effects of buoyancy.

Depending on the depth of the channel, both positive- and negative-dielectrophoresis can be observed in electrode based systems. Positive dielectrophoresis is observed as some fraction of passing particles become trapped on the electrode structures. Negative dielectrophoresis will only be observable if the distance between the electrode array and the opposite channel wall is short, and particles become trapped against the channel wall owing to nDEP and hydrodynamic forces. If the channel is too deep, particles will be forced away from the array (by dielectrophoresis) and across (by hydrodynamic forces, either electrokinetic or pressure driven). In the absence of trapping (i.e. in a deep channel), it can be difficult to characterize the magnitude of nDEP forces, as deflection

toward or away from the viewer is difficult to quantify in traditional microscopy.

Equipment and Experimental Setup The fabrication of arbitrary electrode geometries has been an integral part of the development of dielectrophoresis as a viable technique for particle manipulation. The patterning techniques used are those of the microfabrication or MEMS industry, with electrode structures being fabricated via sputtering or electron-beam evaporation of metals, usually gold[7].

Devices with three dimensional elements must be fabricated in planar configurations and then subsequently aligned using a mask aligner and bonded. The primary difficulty associated with octode cages (and other such three dimensional structures) is the difficulty associated with visualization of trapped or sorted particles. Also, fabricating arrays of these structures can only be accomplished through complicated multilayer fabrication processes. Other geometries — point-lid, ring-dot, and grid-electrode — also require the use of multiple layers of electrodes leading to a concomitant increase in the complexity of device fabrication. *In-situ* fabrication of three dimensional dielectrophoretic traps in an array-able format has been achieved by electroplating gold onto an SU-8 mold [45]. The resulting post-trap configuration (Figure 2.10(b)), allows for easier array fabrication and visualization of trapped particles.

Typically, electrodes are fabricated on glass substrates owing to the well defined deposition process and visualization capabilities. Depositing metal onto the surface, however, limits the efficacy of traditional diffusion-based wafer-to-wafer bonding techniques, and so PDMS covers are generally used to define microfluidic channels [47, 48, 49, 50, 51, 52, 53, 54, 55, 56]. Polymers other than PDMS have also been used, but adhesion remains a difficulty.

[7]Gold is chosen because it offers good conductivity, low production of electrolytic products at a reasonable cost (compared to platinum or palladium), and has well-established protocols for deposition.

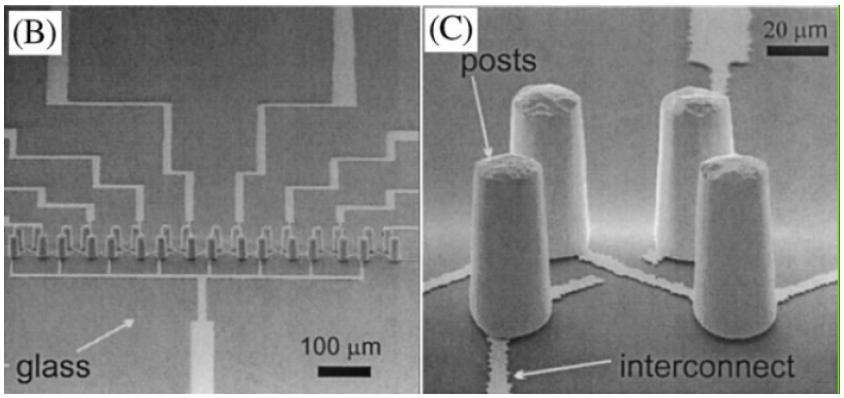

Figure 2.8: The gold post quadrupole trap shown here can be fabricated in a planar configuration and allows for fluorescent or bright-field observation [46].

Insulative Configurations

Insulative dielectrophoresis refers to a subset of DEP techniques that use insulating constrictions in the electric current path to create regions of high or low electric field magnitude. This is done by altering microchannel geometry in a glass, silicone, or plastic substrate. A simple analysis demonstrates the concept: consider a microchannel made of insulating material with two different regions filled with a conducting fluid. Treating each region separately as a one dimensional problem, we can apply Ohm's law and find, for the electric fields in region 1 and 2:

$$\vec{E} = \nabla V \rightarrow \vec{E}_n = E_n \hat{x} = \frac{V_n}{L_n}\hat{x} \tag{2.29}$$

$$E_1 = \frac{V - V_2}{\frac{\sigma L_1}{w_1 d}} \tag{2.30}$$

$$E_2 = \frac{V_2}{\frac{\sigma L_2}{w_2 d}} \tag{2.31}$$

$$\tag{2.32}$$

Solving for V_2 and substituting, we can determine a relationship between E_1 and E_2 as a function of the channel geometry:

$$E_2 = E_1 \frac{w_1}{w_2} \tag{2.33}$$

This is the fundamental principle that leads to the utility of insulative DEP (iDEP) configurations. In addition, there are practical advantages to iDEP; the lack of internal electrodes simplifies fabrication considerably, as electrodes are typically placed in reservoirs external to the microfluidic channel. External electrodes avoid complications due to electrolysis and electrolytic products at low frequencies — which can occur when electrodes are placed inside microfluidic channels — allowing for low frequency operation.

Insulative or electrodeless dielectrophoresis has been primarily used to concentrate samples for later analysis, but we will also explore some designs that accomplish separation based on particle characteristics.

Equipment and Experimental Setup The great appeal of iDEP devices is due to the simplicity of their operation and design. Their fundamental mode of operation does not involve integrated electrodes, inducing variation in electric field gradients via variations in channel geometry. Without integrated electrodes, devices can be fashioned from a single material, greatly simplifying the fabrication process. This process will vary depending on the substrate, but can often be accomplished on the benchtop, outside of a cleanroom.

Substrate choice will depend on the needs of the experiment. Glass devices are well characterized, with well-known physical and electrokinetic properties. Fabrication techniques for glass are well established, but are usually limited to quasi-two-dimensional configurations due to available wet etching techniques. Multi-level glass devices require careful alignment of photomasks to achieve multiple etch steps [57, 58]. Polymeric

devices — polystyrene, Zeonor, TOPAS — have seen increasing use recently, owing to their low cost and greater flexibility. They achieve greater flexibility by leveraging existing silicon fabrication techniques and using the silicon device as a master for hot-embossing [39]. PDMS — a seemingly ubiquitous substrate for microfluidic devices — has not been used to a large degree in iDEP devices. This is due to its geometric variability due to high compliance and relatively high ion permeability — and resulting conductivity — making it a poor insulator. Glass devices, while more difficult to fabricate, can be reused consistently and will perform consistently, given their detailed characterization. Polymeric devices, on the other hand, offer simpler fabrication and lower cost, lending themselves to disposable applications.

2.5 Methods: Data Acquisition, Anticipated Results, and Interpretation

In this section, we provide general recommendations for DEP techniques, followed by specific protocols for select applications. We have divided the protocols into two main classes based on device characteristics: (i) electrode-based and (ii) electrodeless or insulating devices. First, we will outline some general considerations when working with each type of device. Following that, we examine some of the more common, representative experiments and summarize the relevant experimental parameters for each.

General Considerations for Dielectrophoretic Devices

Electrolysis Metal electrodes in aqueous media can lead to the generation of gas bubbles at the electrode-media interface. In order to conduct current through the media

between electrodes, electrons are donated at the anode, creating anions and/or eliminating cations; the reverse then occurs at the cathode to return electrons to the circuit. These Faradaic reactions (often electrolysis of water) generally produce gaseous products near this interface. In many cases, the amount of gas generated is small enough to remain in solution, but the characteristically small volumes used in most eDEP devices lead to decreased storage capacity for these products, and bubbles can form as a result. The specific chemical reaction that is responsible for gas generation depends on the media and the metal used in electrode fabrication. The relevant parameter for estimating the magnitude of these effects is typically current or current density per half cycle, so high-frequency techniques have little or no problems, while low frequency techniques can be challenging. iDEP devices have fewer problems with bubble generation due to electrolysis because electrodes are placed in relatively large, open, external reservoirs.

Media Conductivity Electrolyte concentration influences media conductivity (and therefore electric current and electrolysis), as well as the viability of biological samples. When working with cells or other biological samples, suspending solutions generally contain high concentrations of salts ($\sim 1M$). High conductivity buffers have low electrical resistance, thus requiring more current to maintain an applied electric potential. Two major confounding effects are associated with large electric currents in dielectrophoresis devices: Faradaic reactions (discussed above) and Joule heating. Joule heating is the result of ions flowing through the media, leading to a volumetric heat transfer rate that is proportional to the media conductivity and the square of the applied potential[8]:

$$q''' \sim (\nabla\phi)^2 \sigma_m \tag{2.34}$$

[8]It is important to note that "high conductivity" buffers are still poor conductors when compared to the conductivity of metal electrodes. Because of this, electric potential changes occur almost entirely across the media, driving the electric field source term (Eqn. 2.34) in the metal electrode to zero.

where q''' is the volumetric heat transfer rate to the fluid as the result of the applied electric potential ϕ. The total heat transfer increases with increasing conductivity, and the total integrated heat transfer will increase over time as the system heats up[9].

Electrode configurations in iDEP and eDEP devices vary — eDEP devices have closely spaced electrodes in a microfluidic channel; iDEP devices have electrodes placed in external reservoirs. The large inter-electrode distance in iDEP devices means that the applied electric potential may be orders of magnitude larger than in eDEP devices; however, the electric field magnitude will tend to be comparable in both types of devices, and Joule heating can occur in both cases.

Thermal Effects Variations in temperature, in both iDEP and eDEP devices, can influence a number of experimental parameters, *e.g.,* conductivity, viscosity, and cell viability. We will briefly outline potential sources for temperature variation, possible outcomes, and strategies for maintaining isothermal conditions. Most researchers consider isothermal conditions within their devices — as we have above. Depending on experimental parameters, however, heating may become important, and the isothermal assumption may fail to explain certain results.

Given the electric field source term of Joule heating (Eqn. 2.34), any device region with high field magnitude is a potential source of thermal fluctuations. iDEP techniques can experience local changes in temperature in constricted regions, far from electrodes. Electrode-based DEP techniques can also generate temperature changes, especially near electrodes where current densities are typically highest.

[9]This equation only models the heat transferred *to* the fluid media; a complete analysis will include the heat transferred from the fluid to its surroundings. This relationship is intended to illustrate the dependence of heating on potential and media conductivity. A full solution will also consider the dependence of conductivity on temperature.

Changes in temperature lead to myriad changes in experimental parameters, including fluid viscosity and conductivity. Changes in viscosity change the particle drag coefficient, making measurements of dielectrophoretic or electrophoretic particle mobilities inaccurate. Local changes in viscosity, η, due to temperature variation, lead to changes in the local fluid Reynolds number and complicates the normally tractable low-Reynolds number Navier-Stokes equations. Even a 5°K temperature change will lead to a 10% difference in the viscosity of water [59]. Fluid conductivity is also a function of temperature; the conductivity of electrolyte solutions at 25°C increases approximately $2\%/^{\circ}$K. Impurities tend to buffer these variations in conductivity, so variations should be verified experimentally in temperature sensitive experiments. Local changes in conductivity create locally varying electric fields, which can complicate dielectrophoretic force predictions and lead to nonlinear fluid currents and vorticies [60, 61].

There are a few strategies for avoiding thermal variations in dielectrophoresis experiments. Lower conductivity buffer solutions can ameliorate the effects of high electric fields; many DEP experiments use deionized water as the running buffer for this reason. The dependence of dielectrophoretic effects on the gradient of the electric field also suggests that decreasing the characteristic length scale of a particular device may improve performance at lower electric field magnitudes [44]. Finally, choice of substrate can also improve thermal performance. A material that readily absorbs and dissipates heat (such as glass) will offer improved thermal performance over plastics (polycarbonate, cyclic-olefin polymers, etc.).

Particle Adhesion Depending on the substrate and particle, particle adhesion left unmanaged may be significant and, in some cases, prohibitive. Many techniques are available to ameliorate the effects of adhesion, such as surface coatings or surfactants in solution. An in-depth discussion of this topic is beyond the scope of this text, indeed

there is a large body of literature on the subject [62], but we discuss a few common adhesion mechanisms, such as hydrophobic, electrostatic, and chemical interactions.

The hydrophobic properties of a particle-substrate system can affect particle adhesion. In an aqueous solution, hydrophobic substrates will promote adhesion of hydrophobic particles. Polystyrene particles are hydrophobic and can adhere to hydrophobic substrates such as polycarbonate, cyclic-olefin polymers (TOPAS, Zeonor), and PDMS as a result. Finally, biological samples present a complicated set of interactions that will depend on the specific analyte, which can be either hydrophobic or hydrophilic, positively or negatively charged, and have complicated chemical interactions with the substrate. Bioparticle adhesion is a broad topic that is covered extensively in the literature and remains an active area of research [63, 64].

Charge carrying particles and surfaces will interact with one another electrostatically. Carboxylate-modified polystyrene particles carry a negative surface charge, which will repel them from negatively charged surfaces. The opposite is true for some amine-functionalized particles. Biological particles are invariably zwitterionic but usually net negative. Charge characteristics will also vary as a function of solvent pH, which will change the charge state and surface potential of both particle and substrate.

Certain applications, such as antibody assays and ELISA tests, purposely promote the adhesion of specific particles via chemical interactions. Such adhesion reactions depend on a number of conditions: pH, concentration of product and reactants, temperature, and interaction time.

Transport In both iDEP and eDEP devices, analyte transport can impact device operation. A fundamental challenge when dealing with small planar electrodes in eDEP devices is how to bring particle suspensions into close enough proximity that the electric

field variations caused by the electrode can manipulate the particles. Potential solutions are to use small channels or particle focusing techniques. Transport of fluid and analyte in iDEP systems is also of critical importance. Where pressure driven flow is used, variations in channel geometry that create electric field gradients can break the similitude of electrical and fluidic potential field solutions, leading to difficulties in predicting particle paths. Alternatives are to use very low flow rates in pressure driven flow, or to use electroosmotic/electropohretic effects for media and analyte transport.

Small channel dimensions are the most common solution to ensure that particles interact with DEP forces. However, as channel dimensions shrink, the point approximation for particles (meaning particle motion does not impact fluid behavior) becomes less applicable. A good rule of thumb is that if the bulk DEP relations presented in this chapter are to be used, channel dimensions should be at least ten times larger than particle diameter[10].

Particle focusing techniques can be used, in both eDEP and iDEP devices, to ensure interaction between particles and DEP forces. Fluid flow focusing techniques use variable volumetric flow rates in multiple input channels to control the location of particles in the flow downstream of the intersection. Three (or more) channels converge near the dielectrophoretic section of the device. Two channels contain "sheath fluid" which does not contain any particles while the third channel contains the analyte particles. By setting the volumetric flow rates of the sheath fluid channels higher than the flow rate of the analyte channel, the fluid injected from the analyte channel will be focused by a factor of the ratio of volumetric flow rates [65].

[10]If trapping of particles becomes significant and agglomeration occurs, the effective diameter of agglomerates must be considered.

Fabrication Uncertainty Insulative or electrodeless DEP techniques rely on variations in channel geometry defined by an electrically insulating substrate. Changes in channel geometry leading to changes in electric field magnitude can be estimated by defining a characteristic "constriction ratio" of bulk channel dimensions over constricted channel dimensions. The increase in electric field magnitude due to constrictions in channel geometry will be proportional to the constriction ratio [39]. Variations in channel geometry from manufacturing defects or mechanical strain before or during testing can lead to significant operational changes within the device. Due to the potential significance of these defects, substrate choices should include consideration of material properties such as hardness and modulus. A low modulus material, such as PDMS, might "sag" in wide, long channels (over $1cm^2$). The quality of channels fabricated in high modulus materials such as polycarbonate or Zeonor avoid this issue. Esch et al., examined the quality of devices fabricated with hot-embossing techniques — often used to fabricate devices in these high-modulus materials — is a function of master material choice (e.g. silicon, SU-8, copper) and device design [66]. They found that wet etching of the master material will yield nm-scale surface roughness that will transfer to the plastic, and is not recommended for dielectrophoresis applications. Also, high aspect ratio features and designs with high feature density will be prone to defects at corners and near features on the order of $5\mu m$. Similar confounding effects are observed in eDEP devices. Variations in channel geometry, due to channel "sag," or imperfections in electrode geometry can also lead to erratic electrokinetic effects.

2.5.1 Electrode-based Dielectrophoresis

Given the general considerations above, we will now examine more specific applications. We will cover canonical electrode-based dielectrophoresis techniques and de-

scribe example experimental recipes. For each technique, we will summarize the general configuration of the experiment and then describe what the reader might expect to observe while conducting the experiment. Throughout this section, we will refer to Tables 2.4 and 2.5, which summarize experimental device parameters and solution parameters, respectively. Each experimental technique is identified with a number that corresponds to entries in Tables 2.4 and 2.5 at the end of this section.

Filtering/Binary Sorting

Binary sorting or filtering is one of the most common applications of dielectrophoresis. In these experiments, dielectrophoresis is used to separate one type of particle from a flowing solution based on size or material properties. In this way, a subset of particles (or all particles) are removed from a flowing solution. The goal of these experiments is either to remove a contaminant from solution or to capture particles for analysis.

Experiment ID #1: Interdigitated Electrode Array

Discussion The interdigitated electrode array is one of the most common electrode configurations used in DEP studies. The electrode array consists of two sets of electrodes, grounded and energized, that alternate spatially. This creates a non-uniform field in the region of the electrode array that can be used to trap particles against a flow (Figure 2.9).

Interdigitated electrode arrays have been used extensively to retain particles of interest from a microchannel flow, or to filter out unwanted particles from an analyte stream. Electrodes are typically gold and patterned on a glass substrate via a lift-off procedure. There are only a few relevant design parameters to optimize: electrode width, inter-

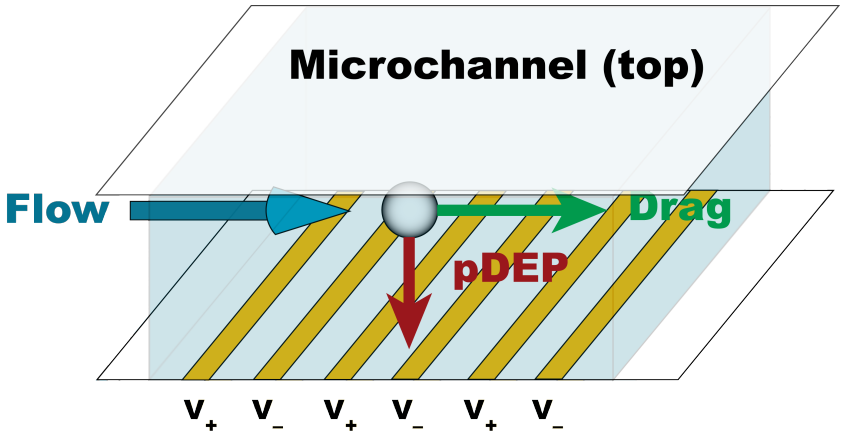

Figure 2.9: An interdigitated electrode array.

electrode distance, electrode length, and fluidic channel depth. With these parameters set, variations in applied electric field magnitude and frequency are left to vary in the experiment.

Electric fields and particle motion are easily modeled (and have been calculated analytically in [67]) in electrode systems and can lead to consistent results when accurate particle models are used [68, 44]. The advantages associated with planar, interdigitated electrode arrays are simplicity of fabrication and analysis. Disadvantages of the interdigitated electrode array are the potential for permanent particle adhesion during positive dielectrophoresis and the inherent "binary" separation achieved under a particular set of experimental conditions.

Trapping in these devices is usually due to pDEP, which attracts particles to electrodes. Occasionally, these devices will operate via nDEP, repelling particles from the array and trapping them against the opposing channel wall, but this regime is less common and more difficult to quantify. The interdigitated electrode array is enclosed in a channel of some sort to sustain pressure driven flow. A common and well-characterized channel can be fabricated using a silicon master and PDMS. Fabrication of the PDMS channel is covered elsewhere in the text. Bonding the PDMS channel to the glass sub-

strate is generally carried out by plasma cleaning, taking care to align the channel perpendicular to the electrode array. Once the channel is bonded to the glass device, particles can be introduced in a dilute suspension via a syringe pump.

Methods For the device characteristics described in Table 2.4 and solution characteristics described in Table 2.5, we would typically observe the following. As particles flow past the interdigitated electrode array, application of an electric field at a frequency of 10kHz will induce positive dielectrophoresis, attracting particles from the fluid to the electrodes. Particle accumulation may be observed via bright field or fluorescence microscopy. Changing the electric field frequency to 1MHz will induce positive dielectrophoresis, reversing the direction of dielectrophoresis and forcing particles into the stream; accumulated particles will be effectively released.

Trapping

Several electrode configurations have been used by investigators to trap single particles or small populations for close observation or manipulation [69, 70, 71, 42, 46, 45]. In general, these devices are used to examine the response of samples to changes in buffer solution or other external stimulus on a particle-by-particle basis.

Experimental ID #2: Quadrupole Traps

Discussion Quadrupole traps consist of four electrodes placed in an "$\times$" or "cross" configuration. Opposite electrodes are energized, with the remaining two grounded or energized 180° out of phase. This configuration creates an electric field minimum in the center of the array and a maximum at the region of closest interaction between

adjacent electrodes. A device in this configuration will trap particles via positive dielectrophoresis in the high field regions. Particles repelled from the high field regions by negative dielectrophoresis may be observable near the central minimum, but typical channel dimensions are large such that particles will be forced away from the plane of the electrodes. A channel depth of approximately 10μm would be necessary to observe particle aggregation via nDEP for micron-scale particles and the experimental parameters listed in Table 2.4. The quadrupole trap is typically used to trap particles via positive dielectrophoresis from a static suspension. Therefore, the channel geometry is largely irrelevant for pDEP, quadrupole trap configurations.

Methods Quadrupolar traps tend to aggregate particles in the high field regions between adjacent electrodes due to positive dielectrophoresis. Particles are introduced using a syringe pump or by applying pressure by hand, but observation takes place at zero flow rate. For device parameters found in Table 2.4 and particle and solution details found in Table 2.5, particle aggregation will be observed between the electrodes for electric field frequencies between 10kHz and 1MHz. Below 8kHz, no aggregation will be observed, due to dissipation from negative dielectrophoresis, unless channel depth is small, as discussed above.

Experiment ID #3: Circle/Dot Traps

Discussion Electrode-based DEP traps generally consist of geometries that tend to trap single particles. The goal is usually to create a system of addressable particle traps to observe individual particle responses to a stimulus or to study biological particle interactions as a function of distance. Methods used to achieve addressable trapping include point-lid, quadrupole cages, ring-dot, and "DEP microwell" geometries (Figure

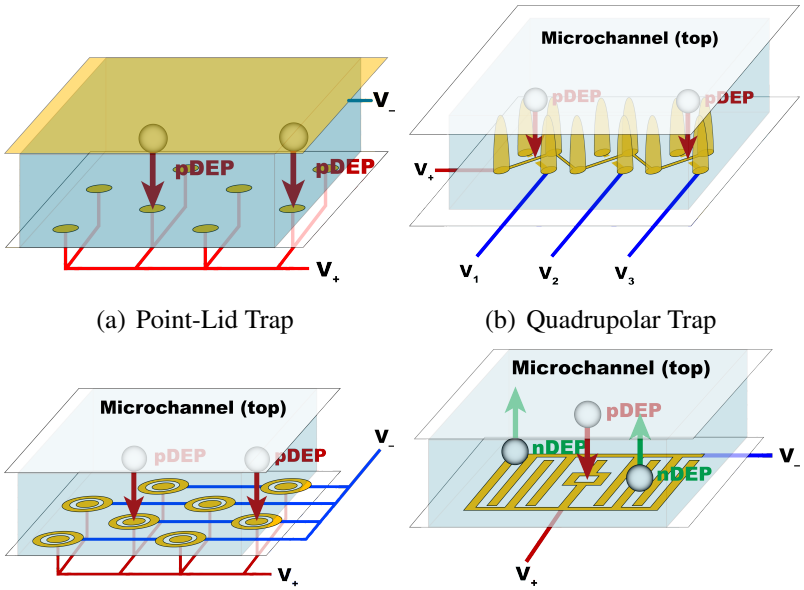

(a) Point-Lid Trap (b) Quadrupolar Trap

(c) Ring-Dot Trap (d) "Micro-well" Trap

Figure 2.10: Various electrode-based DEP trap geometries.

2.10) [72].

Common to all of these geometries is the goal of trapping an individual particle or a small number of particles in one location. To achieve this, electrode geometries are designed to create point-like regions of high (or low) electric field magnitude. Individual addressing is possible in many cases, but usually limited by fabrication of control lines or addressing traces [73].

Circle/Dot traps are a single-particle trapping technique that benefits from easy multiplexing and parallelization. Traps are formed by a two layer lithographic technique and consist of a conducting "dot" exposed on one layer, surrounded by a ring fabricated on a second layer. This configuration traps particles via positive dielectrophoresis, drawing particles into the high field region in the center (dot). A key advantage of this technique is that particles of interest can be released into the flowing buffer by grounding a particular row and column, and collected in an output reservoir or via another collection scheme. This allows easier addressing of individual traps in large arrays. Typical ad-

dressing scales with the number of traps, but in this case, it scales with the square root of the number of traps [73].

Methods Device operation involves sample loading, trapping, extra sample clearing, and release phases. Sample can be loaded by filling the device with particles and energizing ring electrodes (columns) to $+2V_{peak}$ and dot electrodes (rows) to $-2V_{peak}$ at a frequency of 1MHz[11]. The dielectrophoretic trapping force can be modulated by changing the voltage on the ring and/or the dot. The strongest trapping forces will occur when both the dot and ring are energized. If either the ring or the dot is grounded, the dielectrophoretic force will be reduced, but not zero. The analyte suspension can be introduced until all traps are filled. After the loading phase, the excess analyte can be removed by flowing buffer solution over the array at a relatively low flow rate (0.06mL/hr). This flow should continue through the release phase. If both ring and dot are grounded, then the dielectrophoretic force will be zero, and any particle in the trap will be released. This configuration will release only particles at the intersection of a grounded row and a grounded column. Observations can be made on a particle-by-particle basis in each of these traps while varying the buffer solution.

Experiment ID #4: Castellated Electrode Traps

Discussion Castellated electrode arrays have been used to align or trap particles. They consist of interdigitated electrodes with "castellations" along their length (Figure 2.11). This creates alternating regions of high and low electric field magnitude, corresponding to regions of close proximity between castellations and regions of separation in between castellations, respectively. Arrays can be formed by aligned or offset castel-

[11] This is equivalent to a 180° phase differential between the ring and dot.

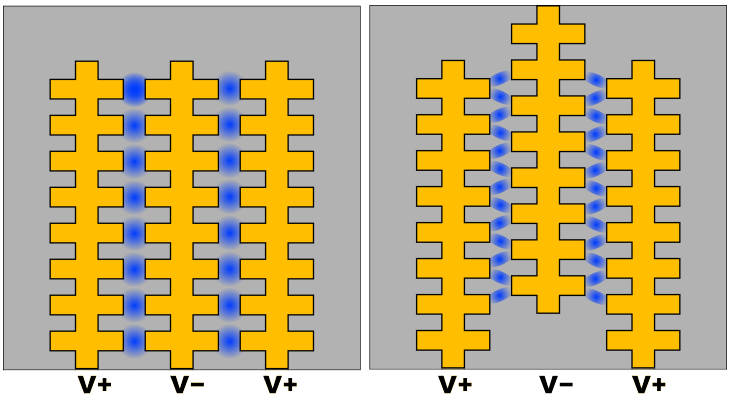

Figure 2.11: A castellated, interdigitated electrode array.

lated electrodes placed adjacent to one another as pictured in Figure 2.11.

Castellated electrode arrays have been used to focus particles from a well-mixed solution into a line of particles for subsequent analysis. This technique has been used in DEP sorting devices and micro-scale dielectric spectroscopy experiments, where the electrical response of individual particles is examined [74, 75]. Both straight and castellated interdigitated electrode arrays can sustain a fluid flow and potentially trap particles against fluid drag forces using DEP. This characteristic has been used to measure not only the sign, but also the magnitude, of DEP forces as a function of frequency. This is accomplished by measuring the number of particles collected by the array at varying electric field frequencies. Castellated electrode arrays, however, are most typically used to concentrate samples (in the high electric field regions, under positive DEP) or to pattern particles at a specific location. The advantage of castellated interdigitated electrodes is the localization of high electric field regions.

In our experimental example, Sebastian et al. utilized aligned, castellated electrode arrays to create localized aggregates of mammalian cells. Such aggregates "could be used as artificial microniches for the study of interactions between cells" [76]. Experimenters trapped layers of stromal cells and Jurkat T-lymphocytes in the high field

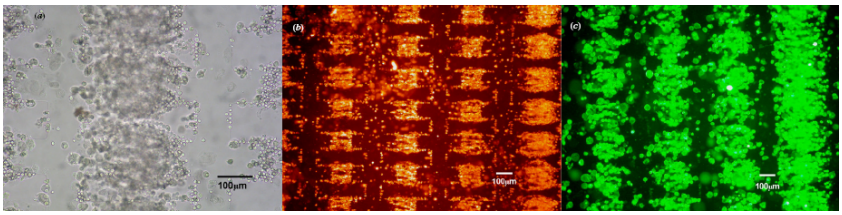

Figure 2.12: (a) Bright field image of cell aggregates formed between castellated electrodes. (b) Red fluorescent labeled Jurkat cells trapped close to the castellated electrode array. (c) Green fluorescent labeled stromal cells trapped on top of Jurkat cells. From [76].

regions between castellations. Trapping fields were maintained until three dimensional aggregates were formed containing both cell types.

Methods Aggregation of mammalian cells (described in Table 2.4) using this array (described in Table 2.5) can be demonstrated in two phases: sample loading and sample aggregation. During the sample loading phase, cell suspensions can be introduced to a flow chamber via a syringe pump. In the aggregation phase, the electrodes can be energized at 1MHz, to voltages ranging from $0V_{peak}$ to $20V_{peak}$, and the cells can aggregate between castellations for $5-12$ minutes. During this time, low conductivity, 480mM D-sorbitol solution should be slowly circulated throughout the flow chamber to wash away ions released from the cells — preventing changes in the local conductivity that would confound dielectrophoretic trapping effects [76].

Sorting

Electrode-based designs used to sort particles based on size or frequency-response are less common than trapping techniques, but have still been well characterized in the literature [77, 78, 79]. These designs typically involve a spatially varying parameter such as electrode geometry or electric field phase that leads to a corresponding distribution

of particles. We present two of the most conceptually illustrative techniques.

Experiment ID #5: Angled or Curved Electrodes

Discussion Angled electrodes can be used to separate particles based on DEP response or as a pre-concentration system to create a localized stream of particles. Castellated electrodes have been used as "concentrators" as well, but the mechanism is slightly different. Castellated electrodes act on particles using negative dielectrophoresis (referring to the sign of f_{CM}, meaning particles are directed away from regions of high electric field) and focus by the cumulative action of a series of high field regions generated between two parallel castellated electrodes. Angled electrodes, in contrast, rely on negative dielectrophoresis to trap particles against fluidic drag forces. Dielectrophoretic forces and fluidic drag forces parallel to the direction of flow balance, and a net force parallel to the electrode results.

The parameters that determine particle behavior in this case are particle size (nearly always a significant contributor to DEP response, see Eqn. 2.10 and §2.3.1), flow velocity, particle position within flow (fluid velocity will vary with distance from channel walls in Poiseuille flow), electric potential, electric field frequency (through f_{CM}), and particle properties (again, through f_{CM}).

Angled electrodes have a few advantages that have led researchers to utilize them to preferentially guide particles or trap them. By angling the electrodes, with reference to the channel, it is possible to take particles trapped against a channel wall by nDEP (see §2.5.1) and displace them transverse to the direction of flow. In this manner, they have been used to preferentially direct particles to different outlets or focus particles into concentrated streams [80, 81, 82, 83].

Schnelle et al., extended the concepts of angled electrodes and achieved a continuous flow separation by creating curved electrodes patterned on the top and bottom of a microfluidic channel. The curved electrodes were aligned with each other on top and bottom and shaped as shown in Figure 2.13 [42].

This curved electrode configuration balances negative dielectrophoresis against fluidic drag forces to achieve spatial separation of analytes in a continuous flow regime. The nDEP force generated at the electrodes is directed parallel to the radius of curvature of the electrode while the fluid drag force is directed parallel to the channel walls. The component of the nDEP force parallel to the direction of fluid flow will tend to trap or stop the forward motion of the particle. The component of the nDEP force perpendicular to the direction of flow will tend to move particles along the electrode. As the local angle of the electrode changes, the nDEP force opposing fluid drag decreases, eventually allowing the particle to pass the electrodes.

Methods This configuration can be used to achieve continuous-flow separation of polystyrene particles as a function of size [77]. Sample experimental device and solution parameters are listed in Tables 2.4 and 2.5. A phosphate buffered saline solution with polystyrene particles of varying diameter can be introduced to the channel by constant pressure-driven flow. Electrodes with angled and curved geometries can be energized to 5.3V_{DC} to manipulate the particles. As the particles enter the device, they can be concentrated into a stream at the edge of the channel via a straight angled electrode "aligner." The mechanism here is similar to that described for interdigitated electrodes above. The "aligning" electrode pair can be designed to be wider than the sorting (curved) electrode pair, leading to higher nDEP forces at the same voltage compared to the narrower curved electrodes [77]. Once aligned at the edge of the channel, particles can then be deflected by the sorting (curved) electrode pair, resulting in a spatial separation that depends on

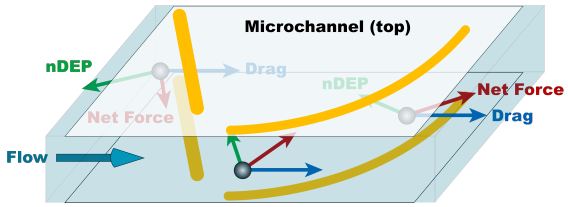

Figure 2.13: Schematic of aligning and sorting electrode pairs used to achieve size-based separation. Particle representations are not to scale. [77]

the local fluid drag and dielectrophoretic forces. Depending on device design, output flow can be divided into a number of separate outlets. Schnelle et al. divided the output of their device into four separate channels.

Experiment ID #6: Traveling-wave Dielectrophoresis

Discussion Travelling-wave dielectrophoresis (twDEP) is the result of an electric field with a spatially varying phase, and is typically created by using an interdigitated electrode array with four separate electric potentials of varying phase applied to individual electrodes (§2.4.2). This leads to a levitation force as well as a transverse force that can be used to sort particles according to Eqn. 2.10. Cui and Morgan designed such a device and demonstrated motion of polystyrene particles via twDEP [84].

Methods Sample experimental device and solution parameters are listed in Tables 2.4 and 2.5, respectively. In this example, the experiment proceeds in two phases: loading and sorting. Initially, a suspension of particles can be introduced to the channel via pressure driven flow. Once the channel is filled, the flow can be stopped and the particles allowed to come to rest. At this point, the electrode array can be energized to $1V_{peak}$ and 1Mhz. When the array is energized, particles will experience a negative dielectrophoresis force levitating them above the array. In addition, the spatial variation

in phase will tend to drive the particles perpendicular to the array (in either direction, depending on the sign of $\Im[f_{CM}]$). Terminal particle velocity can also be measured, and will be directly related to the magnitude of $\Im[f_{CM}]$.

ROT Spectra

Electrorotation techniques provide information about electrical phenotypes on a particle-by-particle basis. Because they trap particles in one position and can measure frequency dependent properties *in situ*, electrorotation is an ideal technique for observing the electrical response of a single particle to various stimuli.

Experiment ID #7: Electrorotation

Discussion In order to measure the rotation spectra of a sample, individual particles must be trapped and examined under a wide range of frequencies. This is typically accomplished using a quadrupolar set of electrodes.

Chan et al., utilized a polynomial electrode array (§2.5.1) to conduct electrorotation studies on uni- and multi-lamellar liposomes [25]. Liposome membranes were constructed from the phospholipid 1,2-dioleoyl-*sn*-glycero-3-phosphocholine (DOPC) and cholesterol. Liposomes encapsulated a solution of Percoll, which increased their density and made handling easier. The use of constructed liposomes was designed to validate multilayer, effective permittivity models[12].

Based on their data, Chan et al., determined that a single-shell effective permittivity

[12]The effective permittivity technique replaces ε_p for a homogeneous particle with $\varepsilon_{p,\text{effective}}$. The derivation involves several iterations of the Laplace equation solution technique. Ultimately, the dipole moment becomes proportional to $\varepsilon_{p,\text{effective}}$. A more detailed discussion can be found in [13].

model can be used for uni- and multi-lamellar liposomes. However, if the liposome contains distinct compartments, the single-shell model fails, and multi-shell modeling must be employed. In addition, it was confirmed that the electrorotation response is a function of internal as well as membrane properties.

Methods Electrorotation experiments involve trapping a particle in a single location, subjecting it to a rotating external electric field, and observing the rate of particle rotation as a function of the electric field frequency. Consider the experimental conditions summarized in Tables 2.4 and 2.5. A polynomial, quadrupolar electrode array can be fabricated, after which particles can be introduced to the chamber surrounding the electrode array at a low concentration (10^6 lipsomes/mL). Once introduced, particles can be allowed to settle. After settling, the trap can be energized, liposomes can be trapped within the array, and the trapped liposomes can be observed to measure their rate of rotation. As the frequency changes, particles will go through regimes where the rotation rate matches the electric field as well as regimes where particle rotation lags electric field rotation or does not rotate at all. When conducting these measurements, only the liposomes that are many diameters from one another and near the center of the array should be recorded. These precautions ensure that particle-particle interactions are minimized and that the electric field near the rotating particles is spatially uniform.

2.5.2 Insulative Dielectrophoresis

Insulative techniques, which rely on compressions or expansions in channel geometry to generate electric field non-uniformities, have been used for a number of applications. Constrictions create locally high electric field regions that can induce deflection [85, 86], trapping [58, 87, 88, 89], or sorting via negative dielectrophoresis [90, 39].

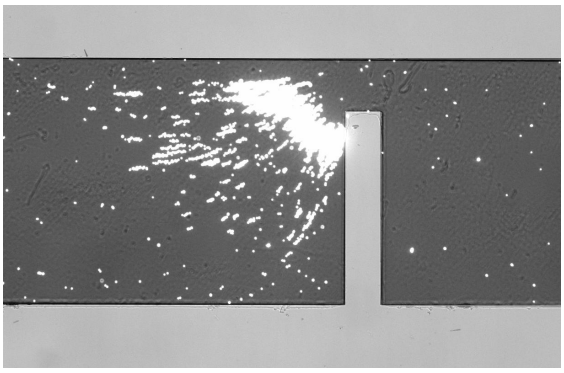

Figure 2.14: nDEP trapping of carboxylate modified fluorescent polystyrene beads. Channel width is 1mm, 200μm in the constricted region, and channel depth is 100μm. [From the authors' lab; unpublished work].

In order to understand iDEP systems it can be beneficial to examine a simple constriction in the electric current path (similar to the theoretical development presented in §2.4.3) and from there build up our understanding of more complicated systems such as an angled constriction and finally our experimental example: a curved constriction.

Perpendicular Constriction In a system with a simple constriction (Figure 2.14), there are two modes that can be explored: trapping particles against fluid drag via negative DEP [39] or deflection of particles from a known, controlled position to another output position based on positive- or negative-dielectrophoretic response [85].

Constriction configurations such as these are useful for trapping or concentrating particles against fluid drag forces using negative dielectrophoresis, but trapped particles must be released before forming a bolus that may clog or alter fluid flow patterns. Constrictions such as these have also been used to alter the flow patterns of particles passing through the constriction [85]. A variable constriction was constructed by introducing an immiscible fluid in a side channel. As the immiscible (insulating) fluid was introduced in the side of the main flow channel, surface tension formed a circular constriction. The amount of constriction could be varied by changing the amount of immiscible fluid in

the side channel, changing the size of the "bubble" constricting the main channel [91].

Angled Constriction Angled constrictions are an extension of the rectangular constrictions considered earlier. A constriction in channel width can become a constriction in channel depth with a simple change of variables. However, practical fabrication considerations lead to an additional degree of freedom that was not possible with constrictions in width: the angle of incidence. The DEP forces generated by the insulating constriction act primarily perpendicular to the constriction, while fluid flow (in the low Reynolds number limit) retains its direction. A summation of forces at the constriction yields an expression that depends on the magnitude of the dielectrophoretic force and the angle of the constriction. If the DEP force is large enough, e.g.:

$$|\vec{F}_{DEP}|\cos\theta > |\vec{F}_{\text{Drag}}| \tag{2.35}$$

particles will be stopped at the constriction and "deflected" parallel to the constriction. Angled constrictions have been used to preferentially separate particles and concentrate particles of interest in a single step [90].

Experimental ID #8: Post Array

Discussion Trapping experiments using post-array type devices offer the most common example of insulative dielectrophoretic techniques. Post array configurations have been used for microbe isolation and detection [58, 87, 88].

The mechanism of action in a post array is largely similar to that of a perpendicular constriction: a constriction in the current path causes a concomitant increase in the local

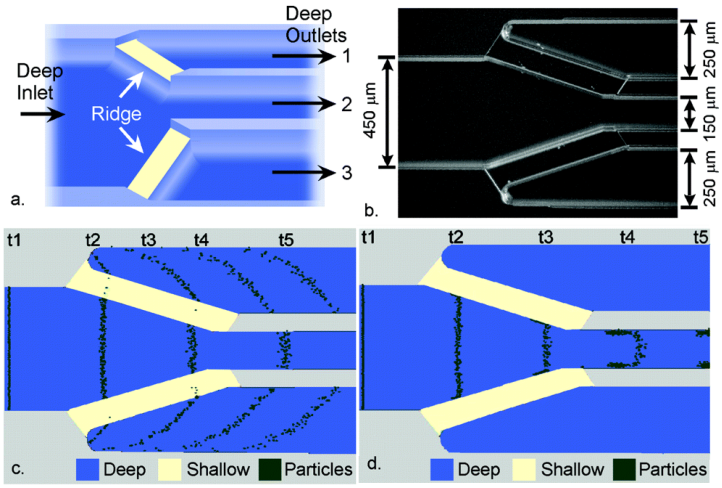

Figure 2.15: Barrett et al [90], fabricated an angled constriction in a glass microchannel. The constriction preferentially segregated particles into different outlet channels.

electric field magnitude, leading to an electric field gradient which drives DEP (§2.4.3). Post array trapping techniques involve flow of a suspension of analyte past a large array of insulating posts. Fluid flow can be either pressure driven from a syringe pump or electrokinetically driven via an external electric field. The advantage of electrokinetically driven flow is that a single DC voltage can be applied to induce fluid flow as well as dielectrophoretic trapping. This approach was used successfully by Lapizco-Encinas et al., to separate live and dead *Escherichia coli*.

Like electrode-based devices, iDEP devices have a wide range of variability in the geometry used to shape electric fields. In the case of post-array type devices, the geometric variables that affect the electric field are the post shape (circular, elliptical, square, etc), gap between posts, and the array angle to the applied electric field. The post shape affects the rate of change of the local electric field between the posts; the gap itself determines the magnitude of the electric field between the posts; and the angle will have a relatively minor impact on the variation of the electric field magnitude[13]. Lapizco-

[13]Since dielectrophoresis depends on the gradient of the squared electric field magnitude, changes in either the peak value of the electric field — between the posts — or the bulk value — "away" from the posts — will alter the dielectrophoretic force. In this case, the angling of the array will tend to

Encinas et al., report that a square array of circular posts yielded the best results (See Tables 2.4 and 2.5).

Methods Trapping and separation of live and dead *E. coli* can be observed in an insulating post array, given device and solution characteristics summarized in Tables 2.4 and 2.5, respectively. Once the device is fabricated and filled with particle solution, care must be taken — *as must always be done in such experiments* — to eliminate pressure driven flow due to reservoir height differences and/or surface tension phenomena. Once the reservoirs are loaded and pressure differences eliminated, flow can be initiated by applying an electric field via electrodes in the external reservoirs. As the applied potential increases, fluid flow rates will also increase ($\propto \vec{E}$) as well as dielectrophoretic forces ($\propto \nabla(\vec{E}\cdot\vec{E})$). As the applied potential reaches 160V ($|\vec{E} = |$16V/mm), nDEP forces will begin to dominate fluid drag forces, and live bacteria will trap between posts in the array. Increasing the potential to 400V ($|\vec{E} = |$40V/mm) will lead to trapping of both live and dead cells. Finally, at a potential of 600V ($|\vec{E}| = 60$V/mm), discrete banding of samples based on differences in dielectrophoretic mobility should appear.

Recall that the dielectrophoretic force is proportional to the permittivity and conductivity of both particle and media, as well as the frequency of the applied electric field. Closer examination of Eqn. 2.1 yields that as $\omega \to 0$, the complex permittivity becomes $j\sigma$, and f_{CM} becomes:

$$f_{CM} = \frac{\sigma_p - \sigma_m}{\sigma_p + 2\sigma_m} \tag{2.36}$$

shift insulating posts into what would normally be the "bulk" region for subsequent posts in the array. This will lead to an increase in the "bulk" value of the electric field, and a decrease in the gradient, leading to a minor decrease in the dielectrophoretic force. Lapizco-Encinas et al., do not report significant variation in performance as a function of the angle of the electrode array. In non-trapping regimes, however, Cummings and co-workers have found that the angle of the array will play a significant role in the "streaming" dielectrophoresis effects observed under non-trapping conditions [92, 41].

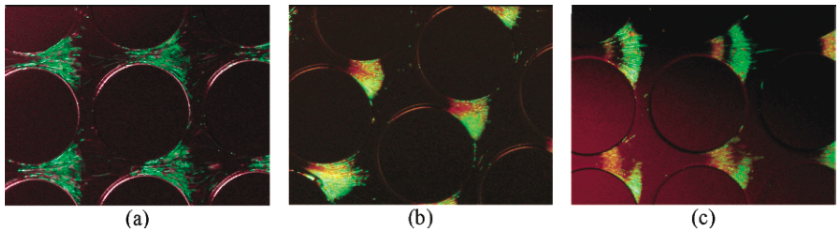

Figure 2.16: Trapping and subsequent separation of live (green) and dead (red) *Escherichia coli* in an insulating post array. (a) 16V/mm, live cells only are trapped; (b) 40V/mm, trapping both live and dead cells with observable banding; (c) 60V/mm, trapping of both live and dead cells with separation of populations. From [87].

It has been reported that, in de-ionized water, the membrane conductivity of live cells is significantly lower than that of dead cells, leading to a significant difference in f_{CM} for the two populations and an observable separation (Figure 2.16).

The key advantages of post array techniques stem from their simplicity of operation. After fabrication, the only necessary component is a power supply which will drive flow and preferential trapping.

Safety Considerations In order to obtain the electric fields required for separation (on the order of 200V/mm) a high voltage (on the order of 2kV) power supply must be used. High voltages are hazardous; experimenters should be trained in the proper usage of all equipment and safety measures.

Experimental ID #9: Curved Constriction

Discussion Further refinement of the angled constriction in channel depth leads to a continuously varying angle of constriction throughout the channel. The resulting curved constriction in channel depth (Figure 2.17) operates on the same basic principle. Dielectrophoretic forces are still perpendicular to the constriction, but now this force

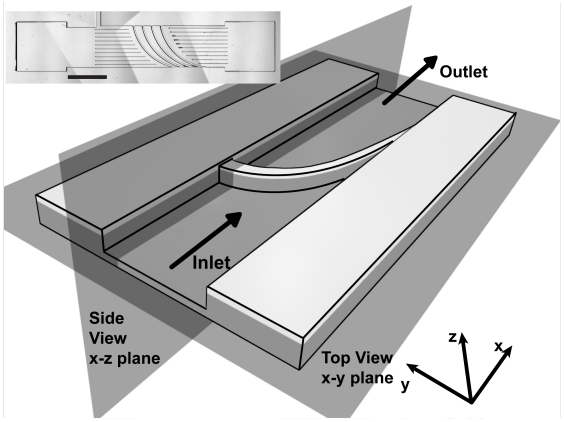

Figure 2.17: A schematic of a constriction in channel depth. Input and output reservoirs, channel top not shown. Inset: a top view of device fabricated in Zeonor 1020R polymer substrate. From [39].

is directed along the radius of constriction curvature. Particles are either trapped and "deflected" at the constriction or allowed to pass. Again, summing forces on a deflected particle at the constriction yields a component parallel to the constriction. As a deflected particle traverses the constriction, the angle θ changes, until the inequality (Eqn. 2.35) is violated or until the particle reaches the channel wall [39].

Hawkins et al. [39] demonstrated particle trapping in a system with a simple constriction using a relatively low-voltage DC signal to drive electrokinetic flow and a high-voltage AC signal to achieve particle trapping via negative dielectrophoresis. They also demonstrated a separation utilizing a curved constriction in channel depth to separate polystyrene particles on the basis of size.

Methods Sample experimental parameters used to separate particles using a curved constriction in channel depth are similar to those described above for trapping in an insulating post array and are listed in Tables 2.4 and 2.5. External reservoirs can be utilized for sample introduction and application of electric potential via platinum electrodes. As with the post-array experiment (§2.5.2), pressure-driven flow due to reservoir

height mismatching or surface tension effects should be eliminated by careful observation and the use of large external reservoirs.

Once the sample is loaded, a low, DC potential of 25V can be applied to induce electrophoretic and electroosmotic flow. After flow is established, an AC signal at 1kHz can be applied in addition to the DC potential. The magnitude of the AC signal is typically 5 to 10 times larger than the DC signal ($125 - 250\mathrm{V}_{\mathrm{peak}}$. At low AC potentials ($> 100\mathrm{V}_{\mathrm{peak}}$), little change will be observed. As the AC potential is increased, deflection of particles at the perpendicular section of the curved constriction will be observed. Once particle deflection is observed, the field amplitude can be increased further to observe additional deflection of particles. In an experiment where two particle populations (e.g. 1.75- and 2μm diameter) are initially uniformly mixed and distributed throughout the channel, deflection will lead to three distinct regions in the output section of the device. Low θ values will lead to downstream regions containing no particles, as they have all been deflected by the constriction. The next region, with higher values of θ will contain smaller particles only. The lower dielectrophoretic force associated with smaller diameters will lead to less deflection. The last region, downstream of higher θ values, will contain both particle types, with a higher population of larger particles due to deflection.

2.5.3 Summary of Experimental Parameters

Tables 2.4, 2.4, 2.5, and 2.5 summarize sample experimental parameters for devices discussed in this section.

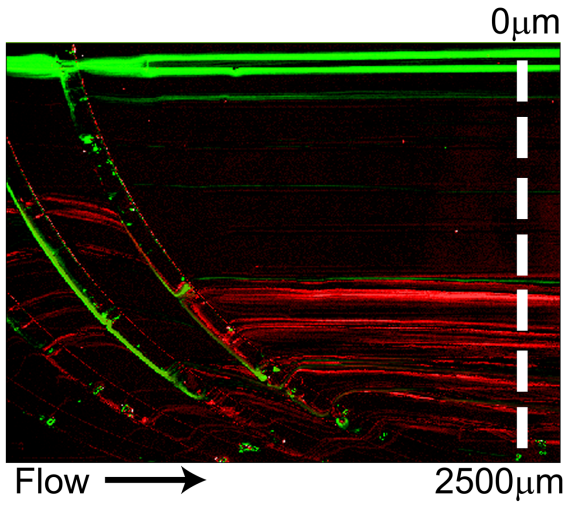

Figure 2.18: Time-lapse (60sec) fluorescence microscopy image. 1.75μm diameter polystyrene spheres (green) are sorted to the center of the channel. 2μm diameter polystyrene spheres (red) are sorted to the bottom of the channel.

2.6 Troubleshooting

Tables 2.6, 2.6, and 2.6 summarize a few of the common problems associated with microfluidic dielectrophoresis experiments and some potential solutions.

2.7 Application Notes

Dielectrophoresis applications range from fractionating particles based upon their "electrical phenotype" [72] to precise manipulation of single particles for property interrogation to new strategies for the creation of engineered tissues and organs. With the emergence of multi-step lab-on-a-chip devices and the use of miniaturized bioanalytical techniques in a microdevice, DEP has become an attractive option for particle and cell manipulation. Owing to the favorable scaling of dielectrophoretic effects at shrinking length scales, the utility of electrokinetically driven flows at these length scales, and the flexibility of microfabrication techniques, integration of these effects is common.

Table 2.4: Experimental device characteristics for DEP applications described in §2.5. ID's correspond to data listed in table 2.5.

ID	*Application*	*Configuration*	*Substrate*
1	Binary Sorting	Interdigitated Electrode Array	Gold electrodes on glass, channel in PDMS
2	Trapping	Quadrapolar Electrode Array	Gold electrodes on glass, channel in PDMS
3	Trapping	Ring-Dot Electrode Array	Gold electrodes on Si/SiO_2 (double layer fabrication); Channel in 3M tape/glass coverslip
4	Trapping	Aligned Castellated Electrode Array	ITO Electrodes on glass; Channel in tape/glass coverslip
5	Sorting	Paired Curved Electrodes	Gold electrodes on glass; channel in glass
6	Sorting	Traveling-wave dielectrophoresis	Gold electrodes on glass/Si_3N_4 insulator (double layer fabrication); channel in SU-8 and PDMS
7	Electrorotation	Polynomial quadrupolar electrodes	Gold electrodes on glass
8	Concentration	Insulating Post Array	Isotropically etched glass, channel in bonded glass coverslip
9	Sorting	Curved Insulating Constriction	Zeonor 1020R

We categorize applications in this section based upon the goals of the user. The first category includes applications that control the relationship between the particle location and the fluid, - e.g. holding or trapping particles relative to a fluid volume. The second category includes applications which control the relationship between particle types, usually dynamically, as the particles progress through a device or fluid stream - e.g. particle sorting and fractionation. The third category includes applications in which control the position of particles relative to each other. While many examples overlap two or more of these categories, these categories nonetheless serve as a framework for classifying relevant applications based upon user goals. This section will serve only as an overview for readers, highlighting specific examples rather than providing a com-

Table 2.4: (Continued).

ID	$V_{0-\text{peak}}$	*Channel (length x width x depth)*	*Characteristic Length Scale*
1	1V	2cm x 100μm x 50μm	Interelectrode spacing, 10μm
2	1V	Not Applicable	Interelectrode Spacing, 25μm
3	2V	Not Applicable	Electrode width, 10μm; Ring diameter, 50μm
4	$0-20\text{V}_{\text{peak}}$	Not Applicable	Electrode width, $50-250\mu$m; Electrode spacing, $50-250\mu$m
5	5.3V	(~ 1)cm x 300-800μm x 40-140μm	Alignment electrode width, 15μm; Curved electrode width, 7μm
6	1V_{peak}	((~ 1)cm x 300μm x 70μm	Electrode width, 10μm; Electrode spacing, 10μm
7	Not Available[a]	Not Applicable	Diagonal electrode spacing, 400μm
8	160-600V_{DC}	10.2mm x Not Applicable x 10μm	Post diameter, 200μm; Center-to-center distance, 250μm
9	50V_{DC}, 750V_{AC}	1cm x 2500μm x 100μm	Constriction, 10μm; Constriction ratio, $r = 10:1$

[a]It is the author's opinion that volatages on the order of 1V or lower should be sufficient.

prehensive review of the applications of DEP. These examples provide context for the detailed discussions throughout the chapter on the methods used to implement DEP.

2.7.1 Particle Trapping

The most common use of DEP is to fractionate a particle suspension by statically trapping particles within a fluidic channel. Variations in electric field are induced in a fluid channel and exert a positive or negative DEP force, causing the particle of interest to be statically confined at or near a peak or valley in the electric field distribution. Particle confinement often occurs as a colloidal suspension propagates through the channel. While positive DEP (pDEP) is most frequently used, owing to the simplicity of system design, negative DEP (nDEP) has been used as well, owing to the lower fields it applies to cells. In order to hold or trap specific populations of particles from a fluid suspension,

Table 2.5: Experimental solution characteristics for DEP applications described in §2.5. All solution percentages are w/v. ID's correspond to data listed in table 2.4.

ID	*Particle*	*Size*	*Concentration*
1	Carboxylate-modified polystyrene	1μm diameter	1.9×10^9 particles/mL
2	Carboxylate-modified polystyrene	2μm diameter	2.4×10^7 particles/mL
3	Silver-coated polystyrene	20μm diameter	Not Applicable
4	Jurkat and AC3 stromal cells	$(\sim 10)\mu$m	5×10^5 cells/mL
5	Unmodified Latex	6.4,10, 15, and 20μm diameter	Not Available
6	Unmodified polystyrene	10μm diameter	Not Available
7	Uni-, multi-lamellar lipsomes	Variable, 2.5-12μm[a]	Not Applicable, 10^6 liposomes/mL
8	Viable and heat-treated *Escherichia coli* cells	$\sim 1\mu$m	6×10^6 cells/mL
9	Carboxylate-modified polystyrene	1.75μm and 2μm diameter	$2 \rightarrow 2.4 \times 10^7$ particles/mL

[a]The expression for electric torque contains a^3 dependence, but this balances against the viscous torque (drag), leading to a rotation rate that is independent of size.

Table 2.5: (Continued).

ID	*Fluid*	*Flow Rate*
1	Deionized water	0.05mL/hr
2	Deionized water	0mL/hr
3	50% sucsrose/DI water, 1% BSA, 1% Triton X-100	0mL/hr for trapping; $0.6 - 3.0$mL/hr for clearing; 0.06mL/hr for release
4	450mM D-sorbitol	Not Applicable (Slow)
5	Deionized water[a]	800μm/s[b]
6	Deionized water[c]	0mL/hr
7	5% mannitol	Not Applicable
8	Deionized water	Variable, electrokinetically driven
9	Deionized water	Variable, electrokinetically driven

[a]Phosphate buffered saline solution was added to stabilize the conductivity of the solution at 1.7 mS/m.
[b]Volumetric flow rates were not available for this experiment.
[c]An electrolyte solution was added to bring the solution conductivity to 1mS/m.

Table 2.6: Tips and suggestions for common problems encountered in dielectrophoresis experiments.

Problem	*Potential Causes*	*Solutions*
Inconsistent flow rate	In pressure driven flow: • check pump for failure • check pump flow rate • check device for bubbles at inlet, outlet, and electrodes	In pressure driven flow: • fix pump • use pump rated for low flow rates • fill device with compatible, low surface tension fluid (e.g. methanol), then thoroughly flush with working fluid • for bubbles forming at electrodes: – reduce fluid conductivity – choose different electrode material (see §2.5)
	In electrokinetic flow: • check power supply • check electrodes for contact • check for bubbles in device • check for bubbles at electrode	In electrokinetic flow: • make sure load (channel) resistance is high for high voltage applications – use a lower conductivity working fluid – reduce channel cross section – increase channel length • remove bubbles from current path (see above) • if electrode contact area is small, bubbles here can also break the current path, take measures to reduce electrolysis – reduce fluid conductivity – choose different electrode material (see §2.5)

(i) the DEP forces on the particles of interest must be greater than the hydrodynamic and gravity forces on the particles and (ii) differences in dielectrophoretic mobility must exist to discriminate populations of particles.

Becker et al created an "electroaffinity column" based upon differences in dielectrophoretic mobility by separating leukaemia cells from blood [93]. They created a wide channel with offset, castellated electrodes (see §2.5.1) along the bottom and injected diluted human blood that was spiked with HL-60 leukemia cells. Erythrocytes (red blood

Table 2.6: (Continued).

Problem	*Potential Causes*	*Solutions*
Particle adhesion	• electric field too high • hydrophobic interactions	• lower applied potential • see §2.5
No or low particle DEP response	$f_{CM} \approx 0$ • check fluid conductivity • check particle conductivity • check electric field frequency	• change σ_m (usually decrease) • change ω
	In trapping experiments: • if $f_{CM} > 0$, channel depth too large • if $f_{CM} < 0$, flow rate too high	• decrease channel depth • decrease flow rate
	Particles not close enough to electrodes (or constrictions in iDEP)	Flow focusing (see §2.5)
Particle aggregation/ clogging	• particle concentration too high • DEP chaining	• dilute particles • lower $\lvert\vec{E}\rvert$
Bubble generation during experiment	• Electrolysis or boiling • Leaking channel	• see §2.5 • seal channel completely

cells) and leukaemia cells were captured from the blood with the application of a $5V_{peak}$, 200kHz AC electrical signal to the electrodes. An elution volume was flowed through the device and the frequency of the electrical signal was decreased to 80kHz causing the release of blood cells but retention of leukaemia cells. At 80kHz, Becker et al calculated the polarizabilities of the leukemia cells to yield a strongly positive DEP force and the erythrocytes to have a repulsive force. As a result, blood cells were eluted and the retained leukaemia cell population was of high purity. The prototype electroaffinity

Table 2.6: (Continued).

Problem	*Potential Causes*	*Solutions*
Particle response/ aggregation via DEP too high or unexpected[a]	Non-uniformities or defects in channel or electrode geometry leading to locally large ∇E^2	• refine fabrication process, use flat surfaces for embossing and remove sharp corners in design • see §2.5
Recirculating flow near electrodes or constrictions	• $\|\vec{E}\|$ too high, leading to thermal variation in σ_m • iDEP constrictions too close together ($\vec{E}$ not decaying fully to bulk value between constrictions) • AC electroosmosis • closely spaced angled constrictions in pressure-driven flow	• lower $\|\vec{E}\|$ • increase feature spacing • decrease σ_m • increase feature spacing

[a] It is difficult to address all experimental challenges. Here we attempt to point the experimenter toward a few *potential* sources of problems.

column created by Becker et al, was able to sort approximately 1000 cells/sec. This technology is scalable, enabling higher throughput of cell sorting by increasing the size of the channel and electrode area and thus allowing a greater volumetric flow rate of sample through the device.

Another application of DEP was demonstrated by Yasukawa et al [83] who used an nDEP "cage" to confine particles within a desired volume and subsequently perform an enzyme-linked immunosorbent assay (ELISA). An ELISA is a quantitative assay that involves the conjugation of fluorophores or chromogens to target surface molecules by antibody coupling for the measurement of selected molecules. The authors patterned electrodes on the top and bottom surface of a channel to create a "caged" area. The downstream electrodes were activated, and polystyrene latex microspheres were con-

centrated into a stream using preliminary focusing electrodes (see §2.5.1). Once the desired quantity of microspheres was collected, the upstream DEP electrode was activated to close the "cage" and prevent additional particles from entering. The authors then performed an immunoreaction to attach antibodies and subsequently fluorphores to the microspheres by adding reagents to the fluid stream. Fluorescence intensity was measured with conventional microscopic techniques. At the conclusion of the assay, both electrodes were deactivated and the labeled particles were released down the channel in the fluid stream.

In a variation on the typical pDEP capture of particles, Urdaneta and Smela [94] used electrodes at multiple frequencies to capture two separate populations of yeast cells (live and dead) from a heterogenous cell suspension. Urdaneta and Smela took advantage of being able to tune the effective Clausius-Mossotti factor (f_{CM}) or frequency response and thus create regions of p- and nDEP that were opposite for each cell type. They created 3 planar electrodes, one grounded and two electrodes at varying frequencies and amplitudes, in two different geometries within a fluidic compartment. An equal part mixture of live and dead yeast cells was injected into the device and the two cell populations were separated with applied signals at 5kHz and 5MHz, respectively. MFDEP has been used for electro-rotational spectra [95], particle levitation [96], and traveling wave DEP (twDEP) [97] applications.

Separation and trapping of cells by their electrical phenotype using DEP enables the efficient capture of a high purity population of cells. As mentioned above, using the "electroaffinity" column Becker et al, as well as others, have demonstrated the ability to separate different cell types from each other, including the clinically applicable separation of tumor cells from non-pathologic cells [93]. In addition to separating a specific cell type from a heterogenous population, DEP has also been utilized to separate same

cell populations to discern physiologic differences such as activation of mitosis [98, 99], exposure to drugs [100, 101, 102, 103], induced cell differentiation [4, 104, 105], and cell death [106, 107, 94, 108]. Using DEP-based devices to potentially separate the same type of cells based upon physiologic parameters is a powerful tool to identify responses of cells to various soluble agents. Besides the direct application of DEP trapping to biological problems, capturing cells also enables a practical method of manipulating cells and particles within a multistep microfluidic lab-on-a-chip device. Investigators have used DEP "gate" electrodes to enable to passage of selected particles based upon dielectrophoretic mobility [109]. This idea can be extended to incorporate multiple gate electrodes to control spatial and temporal particle motion through a microfluidic chip. Likewise, the ability to localize cells within a specified area either on a 2D surface or within a 3D cage, potentially creates a platform to investigate responses of a population of phenotypically similar cells to different chemical environments.

2.7.2 Particle Sorting and Fractionation

Many continuous flow separation techniques use dielectrophoresis to sort, fractionate, or enrich particle populations dynamically within a fluid stream. These methods use either positive or negative DEP (or both) in microfluidic devices to deflect particles transversely such that an enriched population of the desired particles passes into one of several downstream exits. The heterogenous electric fields are created either though variations in fluidic channel geometry (insulative DEP, iDEP) or electrodes (electrode-based DEP, eDEP) along the channel in various configurations. Application of a voltage across a channel with varying geometry, or across electrodes along the length of the fluidic channel, creates locally non-uniform fields and a resulting DEP response from the particles or cells in the fluid stream (see §2.3 and §2.4).

Many continuous flow dielectrophoresis systems utilize insulative configurations. Cummings and Singh [92] explored iDEP using a insulating post arrays and dc electric fields to trap particles or align them in streams (Figures 2.19, 2.17, and §2.5.2). The authors used posts of various shapes and adjusted the orientation of the post arrays within the electric field to induce a p- or nDEP response and thus concentrate or deplete streams of microspheres or reversibly immobilize the microspheres on the insulating posts. In another application, Hawkins et al [39] used a curved ridge to create an insulative constriction region within a microchannel to separate 1.75μm from 2μm microspheres in a heterogenous population (Figure 2.19). Electrokinetically driven flow within the device was established via a dc-offset, ac electric field and particles were deflected along the curved constriction to change the particle's position within the channel (see §2.5.2). The particle deflection depends on the orientation of the constriction and thus Hawkins et al created a tunable system to separate particles based upon dielectrophoretic mobility.

Continuous flow separations have also been demonstrated in electrode-based systems. Hu et al., [80] devised a device that uses DEP to sort cells in a manner analogous to a fluorescence-activated cell sorting (FACS) device (Figure 2.20). In a manner analogous to fluorescent staining for FACS, the authors conjugated beads to some bacterial cells via antibody coupling and mixed the bead conjugated bacteria with non-conjugated bacterial cells. The newly made bead-bacterial cell conjugates are sensitive to a DEP force due to the increased size of the complex. Hu et al injected the bacterial cell suspension into their device and utilized angled electrodes (see §2.5.1) to induce a nDEP force on the labeled bacterial cells to deflect them into a separate collection channel. Their device collected 95% of the labeled cells with a throughput of $2-3\times10^7$ cells/h, a rate comparable to conventional cell sorters. Braschler et al [110] introduced fine control of a particle's deflection along the length of a channel using multiple frequency eDEP (Figure 2.20). Two electrode arrays are patterned on either side of a fluidic channel with

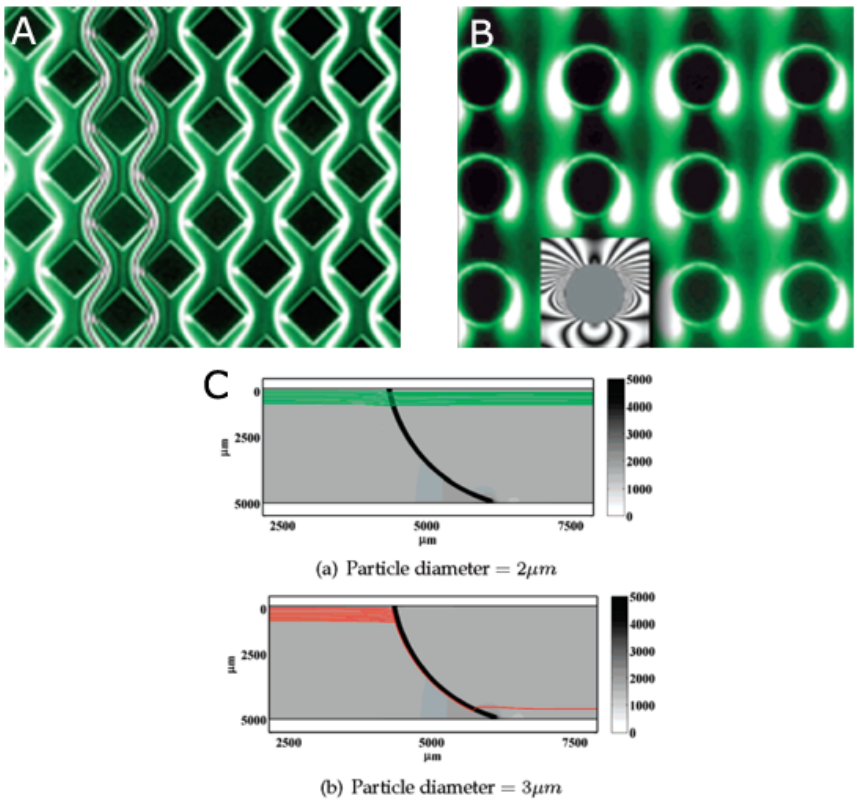

Figure 2.19: A post array using insulative DEP was used by Cummings et al [92] to separate particles into streams (A) or capture them at the posts (B). Hawkins et al [39] created a device using iDEP and a curved constriction (Figure 2.17) to separate 2 μm from 3 μm microspheres (C).

each array excited at different frequencies. The difference in frequencies and the ability to tune the system allows the user to balance the DEP forces on the particle and control a particles' position within the channel as it travels down the length of the electrode array.

Continuous flow techniques have also been used to create temporal separation of particles within a flow. Taking advantage of differing dielectrophoretic mobilities, several groups have used DEP for field flow fractionation (FFF-DEP) [111, 112]. As a particle stream progresses through a microfluidic channel, DEP forces oppose sedimentation (gravity) forces, particles with a weaker DEP response will settle to a lower-velocity streamline within the Poiseuille flow profile. Differences in fluid velocity across the

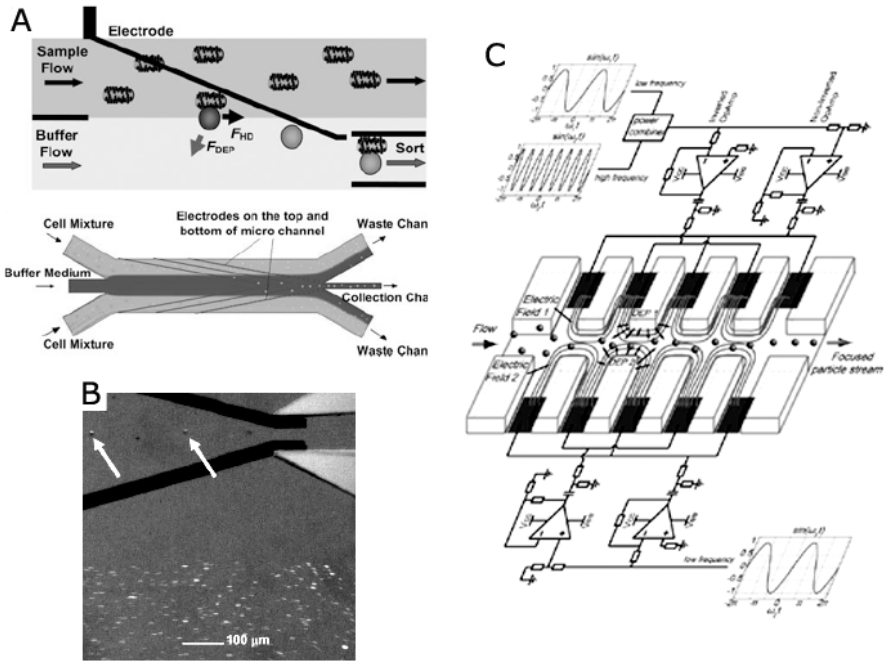

Figure 2.20: DEP was used to continuously separate bacteria conjugated with beads from a heterogenous sample (A) by Hu et al [80]. Angled electrodes deflect bacteria conjugated beads into a buffer stream that exits the device through a collection channel (B). Braschler et al [110] used MFDEP to focus a stream of particles within a channel (C). The differential application of two frequencies to electrodes along each side of a channel enables tunable control of a particle's position.

cross-section of the channel cause elution of the DEP responsive particles at different times. So, in a manner similar to a separation column, particles with high DEP response will be eluted from the device subsequent to those with less of a response.

An advantage of DEP is the ability to separate particles or cells without the need for secondary affinity coupling steps to achieve separation. Traditional techniques such as FACS, flow cytometry, ELISA and affinity chromatography require a pretreatment with fluorescent molecules (FACS, flow cytometry), or specific antigens conjugated to the particles (ELISA, flow chromatography) prior to separation. This bypass of pre-labeling eliminates use of additional reagents and saves processing time. Like many of the commonly cited benefits of microfluidic systems – low Reynolds number, lam-

inar flow, low reagent volumes — dielectrophoresis benefits from the same favorable scaling at small scales. The DEP force is proportional to the gradient of the electric field squared, or the inverse of the characteristic length cubed, and thus the DEP force increases dramatically in these microfluidic environments.

The use of DEP as a continuous flow separation technique has been demonstrated for several types of particles including polymeric spheres [39, 85], bacteria [113], yeast [114], and mammalian cells [115]. Similar to trapping applications, investigators have used DEP in continuous flow applications to separate populations of the same cell with physiologic differences. Examples include separation of stem cells from their differentiated progeny [116] and mammalian cells based upon their cell-cycle phase [115]. These continuous-flow, DEP fractionation devices enable rapid sorting of cells and particles which can be scaled up to fractionate larger populations. Separation of large populations of phenotypically similar cells is of great interest to biologists and tissue engineers who investigate drug interactions with phenotypically varied cells and create in vitro tissue models from pure cell populations.

2.7.3 Single Particle Trapping

In addition to bulk processing of large numbers of particles, the appropriate electrode design enables manipulation of single particles or small groups thereof. These methodologies have enabled significant advances in micro-scale bioanalytical techniques. From a biological perspective, the utility of DEP to manipulate individual particles for the discrimination of properties is promising and opens up new tools to investigate single cells or cell-cell interactions. In general, strategies to address the fine manipulation of particles involve either (1) the use of electrode arrays that are individually addressable or (2)

the use of light on photosensitive conducting materials to dynamically alter the electrode configuration.

An electrode post array was used by Voldman et al [46] to create a microfabricated cytometer to trap and release individual cells with temporal control (Figures 2.21 and 2.10(b), §2.5.1). They used an array of posts to create several quadrupole DEP traps. The nDEP traps captured calcein labeled HL-60 cells and maintained the position of the cell for more than 40 minutes. While the cells were trapped, the investigators were able to perform fluorescence measurements in the device and selectively release individual cells at different time points. Similarly, Taff and Voldman [73] improved on the original cell sorting array by creating addressable traps using a ring-dot pDEP electrode design that is highly scalable (see §2.5.1). Shih et al [117] developed a device for sorting particles with trapping, detection, and sorting regions. The cells were captured in quadrupolar traps, analyzed in real time in a second region of the chip, and then passed into a wide channel with several electrodes patterned on the lower surface (Figure 2.21). The electrodes are addressed appropriately to create nDEP in all areas except a path to the correct outlet channel. The authors were able to successfully sort microspheres with a protein coating from uncoated microspheres into one of five output channels.

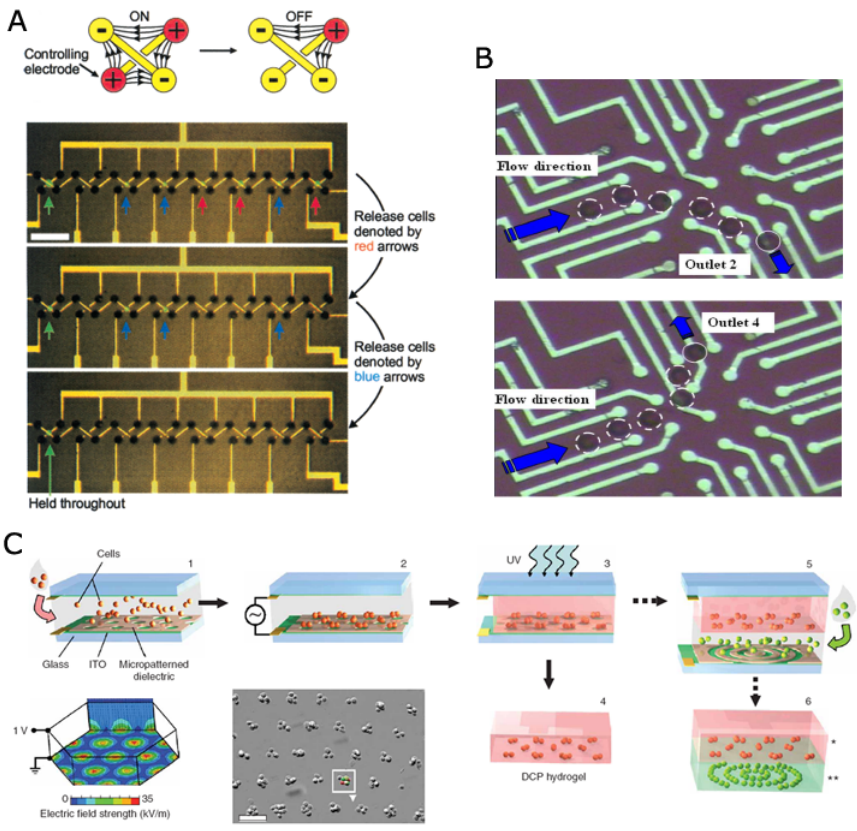

Figure 2.21: A dynamic cytometer was created by Voldman and colleagues [46] with an array of quadrupole traps (A). Individual cells were captured within the respective traps, fluorescence measurements made, and then selectively released. Shih et al [117] used nDEP to dynamically control which outlet particles are sorted into (B). DEP has also been used to pattern cells with controlled spacing in a 3D environment (C) for the investigation of the role of cell signaling on cell growth and tissue formation. Albrecht and colleagues [118] created aggregates of cells with a patterned electrode with evenly spaced trapping regions. Prepolymer was flowed into the channel and photopolymerized to create a hydrogel encasing the cell aggregates. Serial patterning and polymerization can then be used to create engineered tissue analogs with controlled cell localization within a 3D environment.

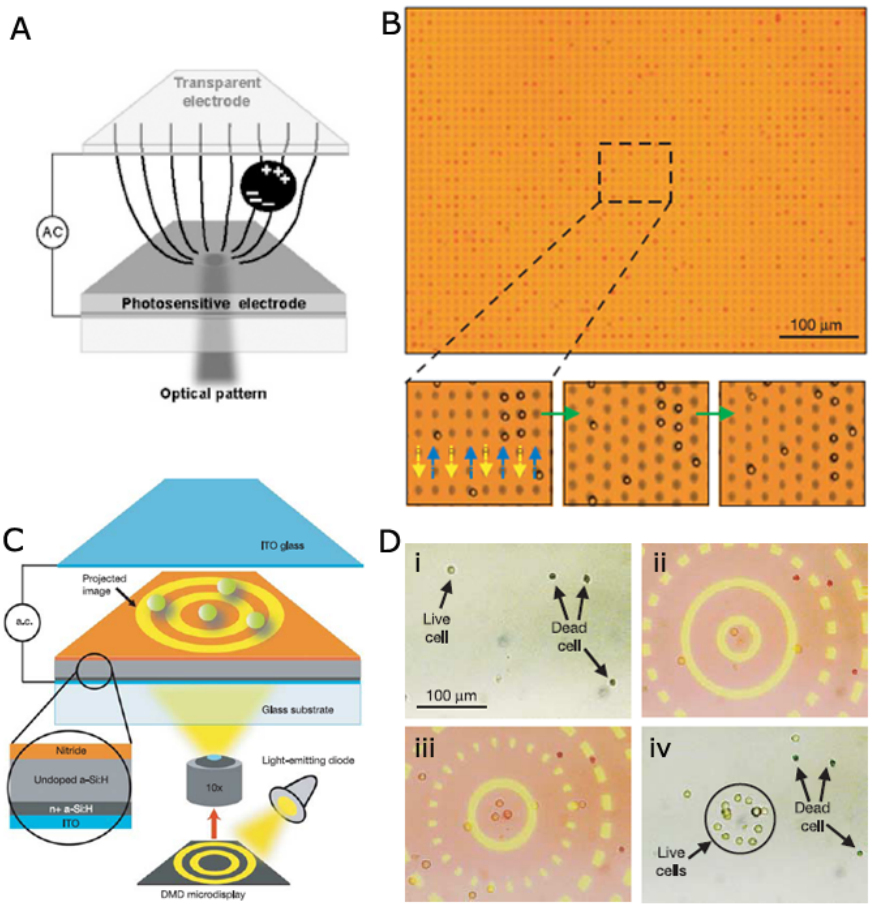

Figure 2.22: Wu and colleagues [119, 120] use light to dynamically create DEP electrode configurations on photosensitive materials (A, C). These "optoelectronic tweezers" have been shown to enable massive parallelization with the ability to move large numbers of particles simultaneously (B) and separate and confine DEP responsive live cells from dead ones (D).

While electrode arrays are usually implemented in a 2D configuration, Albrecht et al [118] used pDEP and photopolymerizable hydrogels to precisely position chondrocytes within a 3D environment (Figure 2.21). They injected cells within a prepolymer solution between two plates patterned with electrodes. The electrodes were energized and DEP caused clusters of cells to form based upon the electrode geometry. Once the cells were patterned, the prepolymer was polymerized using UV light, locking cells into position within a hydrogel. This methodology of using DEP to spatially control cell-cell spacing is a significant step forward in the field of tissue engineering, because conventional techniques are not able to control inter-cell spacing. These 3D, in vitro models allow the investigation of local micro-scale cell signaling and the resulting impact on cell growth and tissue formation.

As evinced by these examples, DEP's strength is in manipulation at the single-particle/single-organism level. While techniques such as optical tweezers and ultrasonic particle manipulation already exist to trap and isolate single particles, DEP systems, in addition to being simpler, cheaper, and potentially more parallelizable, have the advantage of inducing either positive or negative forces. Under the appropriate experimental conditions, this ability leads to selective trapping or controlled aggregation of particles within novel trap designs or 3D cages. In addition to these direct applications, DEP has also proven useful to control cells and particles in multiple-process lab-on-a-chip devices using gates, traps, and particle aligners to regulate spatial and temporal trafficking through microdevices [121, 122].

BIBLIOGRAPHY

[1] Benjamin G. Hawkins, Jason P. Gleghorn, and Brian J. Kirby. *Dielectrophoresis for Particle and Cell Manipulations*, chapter 6, pages 133–182. Artech House, Boston, 2009.

[2] Herbert A. Pohl. The motion and precipitation of suspensions in divergent electric fields. *Journal of Applied Physics*, 22(7):869–871, July 1951.

[3] Herbert A. Pohl. *Dielectrophoresis: The behavior of neutral matter in nonuniform electric fields*. Cambridge University Press, New York, NY, 1978.

[4] X. B. Wang, Y. Huang, F. F. Becker, and P. R. C. Gascoyne. A unified theory of dielectrophoresis and traveling-wave dielectrophoresis. *Journal of Physics D-Applied Physics*, 27(7):1571–1574, Jul 14 1994.

[5] X. J. Wang, X. B. Wang, and P. R. C. Gascoyne. General expressions for dielectrophoretic force and electrorotational torque derived using the maxwell stress tensor method. *Journal of Electrostatics*, 39(4):277–295, Aug 1997.

[6] K. H. Kang and D. Q. Li. Force acting on a dielectric particle in a concentration gradient by ionic concentration polarization under an externally applied dc electric field. *Journal of Colloid and Interface Science*, 286(2):792–806, Jun 15 2005.

[7] H. Liu and H. H. Bau. The dielectrophoresis of cylindrical and spherical particles submerged in shells and in semi-infinite media. *Physics of Fluids*, 16(5):1217–1228, May 2004.

[8] C. Rosales and K. M. Lim. Numerical comparison between maxwell stress method and equivalent multipole approach for calculation of the dielectrophoretic force in single-cell traps. *Electrophoresis*, 26(11):2057–2065, Jun 2005.

[9] A. Al-Jarro, J. Paul, D. W. P. Thomas, J. Crowe, N. Sawyer, F. R. A. Rose, and K. M. Shakesheff. Direct calculation of maxwell stress tensor for accurate trajectory prediction during dep for 2d and 3d structures. *Journal of Physics D-Applied Physics*, 40(1):71–77, Jan 7 2007.

[10] T. B. Jones, K. L. Wang, and D. J. Yao. Frequency-dependent electromechanics of aqueous liquids: Electrowetting and dielectrophoresis. *Langmuir*, 20(7):2813–2818, Mar 30 2004.

[11] Y. Liu, W. K. Liu, T. Belytschko, N. Patankar, A. C. To, A. Kopacz, and J. H. Chung. Immersed electrokinetic finite element method. *International Journal for Numerical Methods in Engineering*, 71(4):379–405, Jul 23 2007.

[12] P. Singh and N. Aubry. Trapping force on a finite-sized particle in a dielectrophoretic cage. *Physical Review E*, 72(1), Jul 2005.

[13] Thomas B. Jones. *Electromechanics of Particles*. Cambridge University Press, New York, NY, 1995.

[14] M. Castellarnau, A. Errachid, C. Madrid, A. Juarez, and J. Samitier. Dielectrophoresis as a tool to characterize and differentiate isogenic mutants of escherichia coli. *Biophysical Journal*, 91(10):3937–3945, Nov 2006.

[15] A. Z. Ehe, A. Ramirez, O. Starostenko, and A. Sanchez. Bioimpedance spectra of small particles in liquid solutions: Mathematical modeling of erythrocyte rouleaux in human blood. *Cross-Disciplinary Applied Research in Materials Science and Technology*, 480-481:251–255, 2005.

[16] J. Gimsa. A comprehensive approach to electro-orientation, electrodeformation, dielectrophoresis, and electrorotation of ellipsoidal particles and biological cells. *Bioelectrochemistry*, 54(1):23–31, Aug 2001.

[17] J. Gimsa, T. Schnelle, G. Zechel, and R. Glaser. Dielectric-spectroscopy of human erythrocytes - investigations under the influence of nystatin. *Biophysical Journal*, 66(4):1244–1253, Apr 1994.

[18] N. G. Green and T. B. Jones. Numerical determination of the effective moments of non-spherical particles. *Journal of Physics D-Applied Physics*, 40(1):78–85, Jan 7 2007.

[19] K. Maswiwat, D. Wachner, R. Warnke, and J. Gimsa. Simplified equations for the transmembrane potential induced in ellipsoidal cells of rotational symmetry. *Journal of Physics D-Applied Physics*, 40(3):914–923, Feb 7 2007.

[20] N. J. Rivette and J. C. Baygents. A note on the electrostatic force and torque acting on an isolated body in an electric field. *Chemical Engineering Science*, 51(23):5205–5211, Dec 1996.

[21] M. Simeonova and J. Gimsa. Dielectric anisotropy, volume potential anomalies and the persistent maxwellian equivalent body. *Journal of Physics-Condensed Matter*, 17(50):7817–7831, Dec 21 2005.

[22] S. Archer, H. Morgan, and F. J. Rixon. Electrorotation studies of baby hamster kidney fibroblasts infected with herpes simplex virus type 1. *Biophysical Journal*, 76(5):2833–2842, May 1999.

[23] T. S. Bakirov, V. M. Generalov, A. A. Chepurnov, G. I. Tyunnikov, and V. D. Poryavaev. Analysis of cell depolarization mechanism at the initial stages of virus-cell interaction. *Doklady Akademii Nauk*, 363(2):258–259, Nov 1998.

[24] F. F. Becker, X. B. Wang, Y. Huang, R. Pethig, J. Vykoukal, and P. R. C. Gascoyne. Separation of human breast-cancer cells from blood by differential dielectric affinity. *Proceedings of the National Academy of Sciences of the United States of America*, 92(3):860–864, Jan 31 1995.

[25] K. L. Chan, P. R. C. Gascoyne, F. F. Becker, and R. Pethig. Electrorotation of liposomes: verification of dielectric multi-shell model for cells. *Biochimica Et Biophysica Acta-Lipids and Lipid Metabolism*, 1349(2):182–196, Nov 15 1997.

[26] M. Egger and E. Donath. Electrorotation measurements of diamide-induced platelet activation changes. *Biophysical Journal*, 68(1):364–372, Jan 1995.

[27] C. D. Falokun and G. H. Markx. Electrorotation of beads of immobilized cells. *Journal of Electrostatics*, 65(7):475–482, Jun 2007.

[28] C. D. Falokun, F. Mavituna, and G. H. Markx. Ac electrokinetic characterisation and separation of cells with high and low embryogenic potential in suspension cultures of carrot (daucus carota). *Plant Cell Tissue and Organ Culture*, 75(3):261–272, Dec 2003.

[29] P. Gascoyne, C. Mahidol, M. Ruchirawat, J. Satayavivad, P. Watcharasit, and F. F. Becker. Microsample preparation by dielectrophoresis: isolation of malaria. *Lab on a Chip*, 2(2):70–75, 2002.

[30] J. Gimsa, P. Marszalek, U. Loewe, and T. Y. Tsong. Dielectrophoresis and electrorotation of neurospora slime and murine myeloma cells. *Biophysical Journal*, 60(4):749–760, Oct 1991.

[31] Y. Huang, X. B. Wang, F. F. Becker, and P. R. C. Gascoyne. Membrane changes associated with the temperature-sensitive p85(gag-mos)-dependent transformation of rat kidney cells as determined by dielectrophoresis and electrorotation. *Biochimica Et Biophysica Acta-Biomembranes*, 1282(1):76–84, Jun 13 1996.

[32] Y. Huang, X. B. Wang, R. Holzel, F. F. Becker, and P. R. C. Gascoyne. Elec-

trorotational studies of the cytoplasmic dielectric-properties of friend murine erythroleukemia-cells. *Physics in Medicine and Biology*, 40(11):1789–1806, Nov 1995.

[33] A.T. Chwang and T.Y. Wu. Hydromechanics of low-reynolds-number flow. 4. translation of spheroids. *Journal of Fluid Mechanics*, 75:677–689, June 1976.

[34] H. Brenner. The slow motion of a sphere through a viscous fluid towards a plane surface. *Chemical Engineering Science*, 16:242–251, 1961.

[35] Sangtae Kim and Seppo J. Karrila. *Microhydrodynamics: Principles and Selected Applications*. Dover Publications, Inc, Boston, MA, 2005.

[36] G.K. Batchelor. Brownian diffusion of particles with hydrodynamic interaction. *Journal of Fluid Mechanics*, 74:1–29, 1976.

[37] A.J. Goldman, R.G. Cox, and H. Brenner. The slow motion of two identical arbitrarily oriented spheres through a viscous fluid. *Chemical Engineering Science*, 21:1151–1170, 1966.

[38] W.B. Russel, D.A. Saville, and W.R. Schowalter. *Colloidal Dispersions*. Cambridge University Press, New York, NY, 1 edition, 1989.

[39] B. G. Hawkins, A. E. Smith, Y. A. Syed, and B. J. Kirby. Continuous-flow particle separation by 3d insulative dielectrophoresis using coherently shaped, dc-biased, ac electric fields. *Analytical Chemistry*, 79(19):7291–7300, Oct 1 2007.

[40] D. E. Chang, S. Loire, and I. Mezic. Separation of bioparticles using the traveling wave dielectrophoresis with multiple frequencies. In *Proceedings of the 42nd IEEE Conference on Decision and Control*, volume 6, pages 6448–6453, Maui, Hawaii, USA, 9-12 December 2003.

[41] E. B. Cummings and A. K. Singh. Dielectrophoresis in microchips containing arrays of insulating posts: Theoretical and experimental results. *Analytical Chemistry*, 75(18):4724–4731, Sep 15 2003.

[42] T. Schnelle, T. Muller, and G. Fuhr. Trapping in ac octode field cages. *Journal of Electrostatics*, 50(1):17–29, Sep 2000.

[43] T. Schnelle, T. Muller, C. Reichle, and G. Fuhr. Combined dielectrophoretic field cages and laser tweezers for electrorotation. *Applied Physics B-Lasers and Optics*, 70(2):267–274, Feb 2000.

[44] A. Castellanos, A. Ramos, A. Gonzalez, N. G. Green, and H. Morgan. Electrohydrodynamics and dielectrophoresis in microsystems: scaling laws. *Journal of Physics D-Applied Physics*, 36(20):2584–2597, Oct 21 2003.

[45] J. Voldman, M. Toner, M. L. Gray, and M. A. Schmidt. Design and analysis of extruded quadrupolar dielectrophoretic traps. *Journal of Electrostatics*, 57(1):69–90, Jan 2003.

[46] J. Voldman, M. L. Gray, M. Toner, and M. A. Schmidt. A microfabrication-based dynamic array cytometer. *Analytical Chemistry*, 74(16):3984–3990, Aug 15 2002.

[47] M. D. Armani, S. V. Chaudhary, R. Probst, and B. Shapiro. Using feedback control of microflows to independently steer multiple particles. *Journal of Microelectromechanical Systems*, 15(4):945–956, Aug 2006.

[48] S. Choi and J. K. Park. Microfluidic system for dielectrophoretic separation based on a trapezoidal electrode array. *Lab on a Chip*, 5(10):1161–1167, 2005.

[49] C. Dalton and K. V. I. S. Kaler. A cost effective, re-configurable electrokinetic microfluidic chip platform. *Sensors and Actuators B-Chemical*, 123(1):628–635, Apr 10 2007.

[50] E. T. Lagally, S. H. Lee, and H. T. Soh. Integrated microsystem for dielectrophoretic cell concentration and genetic detection. *Lab on a Chip*, 5(10):1053–1058, 2005.

[51] S. Li, N. Y. Liu, M. B. Chan-Park, Y. A. Yan, and Q. Zhang. Aligned single-walled carbon nanotube patterns with nanoscale width, micron-scale length and controllable pitch. *Nanotechnology*, 18(45), Nov 14 2007.

[52] Y. S. Liu, T. M. Walter, W. J. Chang, K. S. Lim, L. J. Yang, S. W. Lee, A. Aronson, and R. Bashir. Electrical detection of germination of viable model bacillus anthracis spores in microfluidic biochips. *Lab on a Chip*, 7(5):603–610, 2007.

[53] S. Rajaraman, H. Noh, P. J. Hesketh, and D. S. Gottfried. Rapid, low cost microfabrication technologies toward realization of devices for dielectrophoretic manipulation of particles and nanowires. *Sensors and Actuators B-Chemical*, 114(1):392–401, Mar 30 2006.

[54] M. Varshney, Y. B. Li, B. Srinivasan, and S. Tung. A label-free, microfluidics and interdigitated array microelectrode-based impedance biosensor in combination

with nanoparticles immunoseparation for detection of escherichia coli o157 : H7 in food samples. *Sensors and Actuators B-Chemical*, 128(1):99–107, Dec 12 2007.

[55] L. Wang, L. Flanagan, and A.P. Lee. Side-wall vertical electrodes for lateral field microfluidic applications. *Journal of Microelectromechanical Systems*, 16(2):454–461, April 2007.

[56] L. J. Yang, P. P. Banada, M. R. Chatni, K. S. Lim, A. K. Bhunia, M. Ladisch, and R. Bashir. A multifunctional micro-fluidic system for dielectrophoretic concentration coupled with immuno-capture of low numbers of listeria monocytogenes. *Lab on a Chip*, 6(7):896–905, 2006.

[57] E. B. Cummings, B. A. Simmons, R. V. Davalos, G. J. McGraw, B. H. Lapizco-Encinas, and Y. Fintschenko. Fast and selective concentration of pathogens by insulator-based dielectrophoresis. *Abstracts of Papers of the American Chemical Society*, 230:U404–U405, Aug 28 2005.

[58] B. H. Lapizco-Encinas, R. V. Davalos, B. A. Simmons, E. B. Cummings, and Y. Fintschenko. An insulator-based (electrodeless) dielectrophoretic concentrator for microbes in water. *Journal of Microbiological Methods*, 62(3):317–326, Sep 2005.

[59] Frank M. White. *Fluid Mechanics*. McGraw Hill, New York, NY, 5 edition, 2003.

[60] X Xuan. Joule heating in electrokinetic flow. *Electrophoresis*, 298:33–43, 2008.

[61] N. G. Green, A. Ramos, A. Gonzalez, A. Castellanos, and H. Morgan. Electrothermally induced fluid flow on microelectrodes. *Journal of Electrostatics*, 53(2):71–87, Aug 2001.

[62] W.Q. Ding. Micro/nano-particle manipulation and adhesion studies. *Journal of Adhesion Science and Technology*, 22(5-6):457–480, 2008.

[63] S.M. Kim, S.H. Lee, and K.Y. Suh. Cell research with physically modified microfluidic channels: A review. *Lab on a Chip*, 8(7):1015–1023, 2008.

[64] M. Radisic, R.K. Iyer, and S.K. Murthy. Micro- and nanotechnology in cell separation. *International Journal of Nanomedicine*, 1(1):3–14, 2006.

[65] J. Taylor, G.D. Stubley, and C.L. Ren. Experimental determination of sample stream focusing with fluorescent dye. *Electrophoresis*, 29(14):2953–2959, 2008.

[66] M. B. Esch, S. Kapur, G. Irizarry, and V. Genova. Influence of master fabrication techniques on the characteristics of embossed microfluidic channels. *Lab on a Chip*, 3(2):121–127, 2003.

[67] T. Sun, H. Morgan, and N. G. Green. Analytical solutions of ac electrokinetics in interdigitated electrode arrays: Electric field, dielectrophoretic and traveling-wave dielectrophoretic forces. *Physical Review E*, 76(4), Oct 2007.

[68] A. Sanchis, A. P. Brown, M. Sancho, G. Martinez, J. L. Sebastian, S. Munoz, and J. M. Miranda. Dielectric characterization of bacterial cells using dielectrophoresis. *Bioelectromagnetics*, 28(5):393–401, Jul 2007.

[69] M. Abe, M. Orita, H. Yamazaki, S. Tsukamoto, Y. Teshima, T. Sakai, T. Ohkubo, N. Momozawa, and H.ora Sakai. Three-dimensional arrangements of polystyrene latex particles with a hyperbolic quadruple electrode system. *Langmuir*, 20(12):5046–5051, Jun 8 2004.

[70] G. Fuhr, T. Muller, V. Baukloh, and K. Lucas. High-frequency electric field trapping of individual human spermatozoa. *Human Reproduction*, 13(1):136–141, Jan 1998.

[71] I. Ikeda, S. Tsukahara, H. Monjushiro, and H. Watarai. Fabrication of planar multipole microelectrodes for dielectrophoresis by laser ablation. *Bunseki Kagaku*, 51(9):767–772, Sep 2002.

[72] J. Voldman. Electrical forces for microscale cell manipulation. *Annual Review of Biomedical Engineering*, 8:425–454, 2006.

[73] B. M. Taff and J. Voldman. A scalable addressable positive-dielectrophoretic cell-sorting array. *Analytical Chemistry*, 77(24):7976–7983, Dec 15 2005.

[74] D. Mietchen, T. Schnelle, T. Muller, R. Hagedorn, and G. Fuhr. Automated dielectric single cell spectroscopy - temperature dependence of electrorotation. *Journal of Physics D-Applied Physics*, 35(11):1258–1270, Jun 7 2002.

[75] H. Morgan, T. Sun, D. Holmes, S. Gawad, and N. G. Green. Single cell dielectric spectroscopy. *Journal of Physics D-Applied Physics*, 40(1):61–70, Jan 7 2007.

[76] A. Sebastian, A. M. Buckle, and G. H. Markx. Formation of multilayer aggregates of mammalian cells by dielectrophoresis. *Journal of Micromechanics and Microengineering*, 16(9):1769–1777, Sep 2006.

[77] T. Schnelle, T. Muller, S. Fiedler, and G. Fuhr. The influence of higher moments on particle behaviour in dielectrophoretic field cages. *Journal of Electrostatics*, 46(1):13–28, Mar 1999.

[78] X. B. Wang, Y. Huang, X. J. Wang, F. F. Becker, and P. R. C. Gascoyne. Dielectrophoretic manipulation of cells with spiral electrodes. *Biophysical Journal*, 72(4):1887–1899, Apr 1997.

[79] M. D. Vahey and J. Voldman. An equilibrium method for continuous-flow cell sorting using dielectrophoresis. *Analytical Chemistry*, 80(9):3135–3143, May 1 2008.

[80] X. Y. Hu, P. H. Bessette, J. R. Qian, C. D. Meinhart, P. S. Daugherty, and H. T. Soh. Marker-specific sorting of rare cells using dielectrophoresis. *Proceedings of the National Academy of Sciences of the United States of America*, 102(44):15757–15761, Nov 1 2005.

[81] D. Holmes and H. Morgan. Cell sorting and separation using dielectrophoresis. *Electrostatics 2003*, (178):107–112, 2004.

[82] D. Holmes, H. Morgan, and N. G. Green. High throughput particle analysis: Combining dielectrophoretic particle focussing with confocal optical detection. *Biosensors & Bioelectronics*, 21(8):1621–1630, Feb 15 2006.

[83] T. Yasukawa, M. Suzuki, T. Sekiya, H. Shiku, and T. Matsue. Flow sandwich-type immunoassay in microfluidic devices based on negative dielectrophoresis. *Biosensors & Bioelectronics*, 22(11):2730–2736, May 15 2007.

[84] L. Cui and H. Morgan. Design and fabrication of travelling wave dielectrophoresis structures. *Journal of Micromechanics and Microengineering*, 10(1):72–79, Mar 2000.

[85] K. H. Kang, Y. J. Kang, X. C. Xuan, and D. Q. Li. Continuous separation of microparticies by size with direct current-dielectrophoresis. *Electrophoresis*, 27(3):694–702, Feb 2006.

[86] K. H. Kang, X. C. Xuan, Y. J. Kang, and D. Q. Li. Effects of dc-dielectrophoretic force on particle trajectories in microchannels. *Journal of Applied Physics*, 99(6), Mar 15 2006.

[87] B. H. Lapizco-Encinas, B. A. Simmons, E. B. Cummings, and Y. Fintschenko.

Dielectrophoretic concentration and separation of live and dead bacteria in an array of insulators. *Analytical Chemistry*, 76(6):1571–1579, Mar 15 2004.

[88] B. H. Lapizco-Encinas, B. A. Simmons, E. B. Cummings, and Y. Fintschenko. Insulator-based dielectrophoresis for the selective concentration and separation of live bacteria in water. *Electrophoresis*, 25(10-11):1695–1704, Jun 2004.

[89] P. Mela, A. van den Berg, Y. Fintschenko, E. B. Cummings, B. A. Simmons, and B. J. Kirby. The zeta potential of cyclo-olefin polymer microchannels and its effects on insulative (electrodeless) dielectrophoresis particle trapping devices. *Electrophoresis*, 26(9):1792–1799, May 2005.

[90] L. M. Barrett, A. J. Skulan, A. K. Singh, E. B. Cummings, and G. J. Fiechtner. Dielectrophoretic manipulation of particles and cells using insulating ridges in faceted prism microchannels. *Analytical Chemistry*, 77(21):6798–6804, Nov 1 2005.

[91] I. Barbulovic-Nad, X. Xuan, J.S.H. Lee, and D. Li. Dc-dielectrophoretic separation of microparticles using an oil droplet obstacle. *Lab on a Chip*, 6:274–279, 2006.

[92] E. B. Cummings. Streaming dielectrophoresis for continuous-flow microfluidic devices. *Ieee Engineering in Medicine and Biology Magazine*, 22(6):75–84, Nov-Dec 2003.

[93] F. F. Becker, X. B. Wang, Y. Huang, R. Pethig, J. Vykoukal, and P. R. C. Gascoyne. The removal of human leukemia-cells from blood using interdigitated microelectrodes. *Journal of Physics D-Applied Physics*, 27(12):2659–2662, Dec 14 1994.

[94] M. Urdaneta and E. Smela. Multiple frequency dielectrophoresis. *Electrophoresis*, 28(18):3145–3155, Sep 2007.

[95] W.M. Arnold, H.P. Schwan, and U. Zimmermann. Surface conductance and other properties of latex-particles measured by electrorotation. *Journal of physical chemistry*, 91(19):5093–5098, 1987.

[96] K. V. I. S. Kaler, J. P. Xie, T. B. Jones, and R. Paul. Dual-frequency dielectrophoretic levitation of canola protoplasts. *Biophysical Journal*, 63(1):58–69, Jul 1992.

[97] R. Pethig, M. S. Talary, and R. S. Lee. Enhancing traveling-wave dielectrophore-

sis with signal superposition. *Ieee Engineering in Medicine and Biology Magazine*, 22(6):43–50, Nov-Dec 2003.

[98] Y. Huang, X. B. Wang, P. R. C. Gascoyne, and F. F. Becker. Membrane dielectric responses of human t-lymphocytes following mitogenic stimulation. *Biochimica Et Biophysica Acta-Biomembranes*, 1417(1):51–62, Feb 4 1999.

[99] X. Hu, W.M. Arnold, and U. Aimmermann. Alterations in the electrical-properties of lymphocyte-t and lymphocyte-b membranes induced by mitogenic stimulation - activation monitored by electro-rotation of single cells. *Biochimica et biophysica acta*, 1021(2):191–200, 1990.

[100] F. H. Labeed, H. M. Coley, H. Thomas, and M. P. Hughes. Assessment of multidrug resistance reversal using dielectrophoresis and flow cytometry. *Biophysical Journal*, 85(3):2028–2034, Sep 2003.

[101] KF Hoettges, Y Hubner, LM Broche, SL Ogin, GEN Kass, and MP Hughes. Dielectrophoresis-activated multiwell plate for label-free high-throughput drug assessment. *Analytical chemistry*, 80(6):2063–2068, 2008.

[102] L Duncan, H Shelmerdine, MP Hughes, HM Coley, Y Hubner, and FH Labeed. Dielectrophoretic analysis of changes in cytoplasmic ion levels due to ion channel blocker action reveals underlying differences between drug-sensitive and multidrug-resistant leukaemic cells. *Physics in medicine and biology*, 53(2):N1–N7, 2008.

[103] M. P. Hughes and K. F. Hoettges. Dielectrophoresis for drug discovery and cell analysis: novel electrodes for high-throughput screening. *Biophysical Journal*, 88(1):172A–172A, Jan 2005.

[104] P. R. C. Gascoyne, R. Pethig, J. P. H. Burt, and F. F. Becker. Membrane-changes accompanying the induced-differentiation of friend murine erythroleukemia-cells studied by dielectrophoresis. *Biochimica Et Biophysica Acta*, 1149(1):119–126, Jun 18 1993.

[105] S Chin, MP Hughes, HM Coley, and FH Labeed. Rapid assessment of early biophysical changes in k562 cells during apoptosis determined using dielectrophoresis. *International journal of nanomedicine*, 1(3):333–337, 2006.

[106] A. Docoslis, N. Kalogerakis, L. A. Behie, and K. V. I. S. Kaler. A novel dielectrophoresis-based device for the selective retention of viable cells in cell culture media. *Biotechnology and Bioengineering*, 54(3):239–250, May 5 1997.

[107] A. Docoslis, N. Kalogerakis, and L. A. Behie. Dielectrophoretic forces can be safely used to retain viable cells in perfusion cultures of animal cells. *Cytotechnology*, 30(1-3):133–142, 1999.

[108] F. H. Labeed, H. M. Coley, and M. P. Hughes. Differences in the biophysical properties of membrane and cytoplasm of apoptotic cells revealed using dielectrophoresis. *Biochimica Et Biophysica Acta-General Subjects*, 1760(6):922–929, Jun 2006.

[109] C. D. James, M. Okandan, P. Galambos, S. S. Mani, D. Bennett, B. Khusid, and A. Acrivos. Surface micromachined dielectrophoretic gates for the front-end device of a biodetection system. *Journal of Fluids Engineering-Transactions of the Asme*, 128(1):14–19, Jan 2006.

[110] T Braschler, N Demierre, E Nascimento, T Silva, AG Oliva, and P Renaud. Continuous separation of cells by balanced dielectrophoretic forces at multiple frequencies. *Lab on a chip*, 8(2):280–286, 2008.

[111] G. H. Markx, J. Rousselet, and R. Pethig. Dep-fff: Field-flow fractionation using non-uniform electric fields. *Journal of Liquid Chromatography & Related Technologies*, 20(16-17):2857–2872, 1997.

[112] Y. Huang, X. B. Wang, F. F. Becker, and P. R. C. Gascoyne. Introducing dielectrophoresis as a new force field for field-flow fractionation. *Biophysical Journal*, 73(2):1118–1129, Aug 1997.

[113] G. H. Markx and R. Pethig. Dielectrophoretic separation of cells - continuous separation. *Biotechnology and Bioengineering*, 45(4):337–343, Feb 20 1995.

[114] J. Q. Li, Q. Zhang, Y. H. Yan, S. Li, and L. Q. Chen. Fabrication of carbon nanotube field-effect transistors by fluidic alignment technique. *Ieee Transactions on Nanotechnology*, 6(4):481–484, Jul 2007.

[115] Y. Kim, S. Hong, S. H. Lee, K. Lee, S. Yun, Y. Kang, K. K. Paek, B. K. Ju, and B. Kim. Novel platform for minimizing cell loss on separation process: Droplet-based magnetically activated cell separator. *Review of Scientific Instruments*, 78(7), Jul 2007.

[116] LA Flanagan, J Lu, L Wang, SA Marchenko, NL Jeon, AP Lee, and ES Monuki. Unique dielectric properties distinguish stem cells and their differentiated progeny. *Stem cells*, 26(3):656–665, 2008.

[117] T. C. Shih, K. H. Chu, and C. H. Liu. A programmable biochip for the applications of trapping and adaptive multisorting using dielectrophoresis array. *Journal of Microelectromechanical Systems*, 16(4):816–825, Aug 2007.

[118] D. R. Albrecht, G. H. Underhill, T. B. Wassermann, R. L. Sah, and S. N. Bhatia. Probing the role of multicellular organization in three-dimensional microenvironments. *Nature Methods*, 3(5):369–375, May 2006.

[119] P. Y. Chiou, A. T. Ohta, and M. C. Wu. Massively parallel manipulation of single cells and microparticles using optical images. *Nature*, 436(7049):370–372, Jul 21 2005.

[120] A. T. Ohta, P. Y. Chiou, T. H. Han, J. C. Liao, U. Bhardwaj, E. R. B. McCabe, F. Q. Yu, R. Sun, and M. C. Wu. Dynamic cell and microparticle control via optoelectronic tweezers. *Journal of Microelectromechanical Systems*, 16(3):491–499, Jun 2007.

[121] S. Fiedler, S. G. Shirley, T. Schnelle, and G. Fuhr. Dielectrophoretic sorting of particles and cells in a microsystem. *Analytical Chemistry*, 70(9):1909–1915, May 1 1998.

[122] T. Muller, G. Gradl, S. Howitz, S. Shirley, T. Schnelle, and G. Fuhr. A 3-d microelectrode system for handling and caging single cells and particles. *Biosensors & Bioelectronics*, 14(3):247–256, Mar 15 1999.

CHAPTER 3

CONTINUOUS-FLOW PARTICLE SEPARATION BY 3D INSULATIVE DIELECTROPHORESIS USING COHERENTLY SHAPED, DC-BIASED, AC ELECTRIC FIELDS

3.1 Abstract

We present the development of a continuous-flow, "dielectrophoretic spectrometer" based on insulative DEP techniques and 3-dimensional geometric design. Hot-embossed thermoplastic devices allow for high-throughput analysis and geometric control of electric fields via high width-to-depth aspect ratio (250:1), ridged microstructures patterned in a larger channel. We manipulate particles with DC-biased, AC electric fields and generate continuous output streams of particles with a transverse outlet position specified by linear and nonlinear particle mobilities. We show, with simulation and experiment, that characteristic shape factors can be defined which capture the effects of constrictions in channel depth and that modulating the angle of these constrictions changes the resulting local DEP force. Microdevices are fabricated with an insulative constriction in channel depth, whose angle of incidence with the direction of flow varies continuously, across the channel width. The resulting electric field gradients enable demonstration of a "dielectrophoretic spectrometer" that separates particles and controls their transverse position in the device.

[0]The content of this chapter was submitted and accepted for publication as a research article "Continuous-Flow Particle Separation by 3D Insulative Dielectrophoresis using Coherently Shaped, DC-biased, AC Electric Fields" in the journal *Analytical Chemistry*. Reproduced with permission from [1].

3.2 Introduction

Dielectrophoresis (DEP) based techniques offer a number of significant advantages over traditional methods for particle separation such as FACS, flow cytometry, ELISA, or affinity chromatography. The dielectrophoretic force – force on a dipole due to electric field gradients[2, 3] – requires no secondary affinity coupling steps to achieve continuous flow separation, because it is a direct function of particle characteristics such as size, charge, conductivity, and permittivity. When applied to cells, the DEP force is a direct function of these parameters; thus defining a cell's "electrical phenotype"[4]. This character makes DEP especially useful for effecting separation of cells based on size, species, growth cycle, viability, and morphotype. Morphotypic discrimination of cellular analytes is a necessary step in many drug development applications and biological studies, particularly for bacterial species whose pathogenicity is closely tied to morphotype, such as *Mycobacterium tuberculosis* and *Mycobacterium avium complex* (MAC)[5]. At present, morphotypic discrimination and separation is primarily accomplished by direct visual inspection.

Electrode-based dielectrophoretic techniques (eDEP) are the most widely. While offering flexibility in electrode geometry, they are limited by fouling and the generation of electrolytic products. Electrodes create high electric fields and field gradients with a relatively low applied potential, making them compatible with higher frequencies [6, 7, 8, 9, 10, 11, 12, 13, 14, 15, 16, 17, 18]. Electrode geometries are defined by lithographic processes, and therefore numerous planar electrode configurations exist. However, electrodes can foul with use and are limited to higher frequencies due to electrolysis.

Electrodeless or insulative DEP (iDEP) techniques are becoming more widely used

because they can be actuated with both low and high frequency fields, avoid failure due to fouling, and are compatible with high-volume manufacturing techniques such as injection molding. iDEP techniques use constrictions in the electrical current path to change the electric field, and can therefore require higher applied potentials.

The majority of eDEP and iDEP techniques reported to date are batch process techniques, which ultimately limit device throughput. Reported continuous flow techniques [19, 20, 21, 22, 23, 24] show considerable promise for rapid separation, filtering, or screening applications, but typically result in binary separations centered around a single value of DEP mobility (or ratio of mobilities, as in [21] and [22]).

We show that a simplified model adequately predicts particle behavior and that continuous flow particle separation in our device is relatively sensitive to DEP mobility. We overcome the limitations of traditional iDEP by (i) applying a DC-offset, AC electric field to decouple linear and non-linear electrokinetic effects, and (ii) rationally designing insulative structures to actuate nonlinear forces, and noting that samples of interest respond to low-frequency applied fields. The output particle separation in our device uniquely exhibits continuous variation of dielectrophoretic mobility perpendicular to the direction of flow.

3.3 Theory and System Design

Most iDEP devices trap particles by countering bulk particle motion (the result of electrosmosis, electrophoresis, or pressure-driven flow) with local, dielectrophoretic forces, creating a point where the net particle velocity is zero. Insulting constrictions in the width of a microfluidic channel are traditionally used to modulate local DEP forces [19, 20, 25]. Constricting the depth of a channel, rather than the width introduces an

additional degree of freedom: the angle of incidence between bulk migratory forces and opposing DEP forces. Extending this idea further, we vary the angle of incidence continuously across the channel width, transverse to the direction of flow, by using a curved constriction in depth (Figure 3.1).

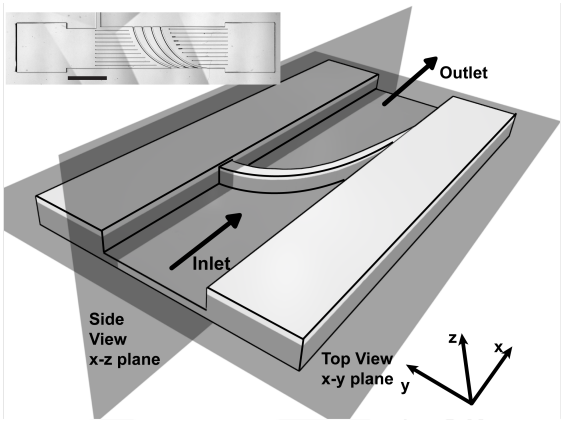

(a)

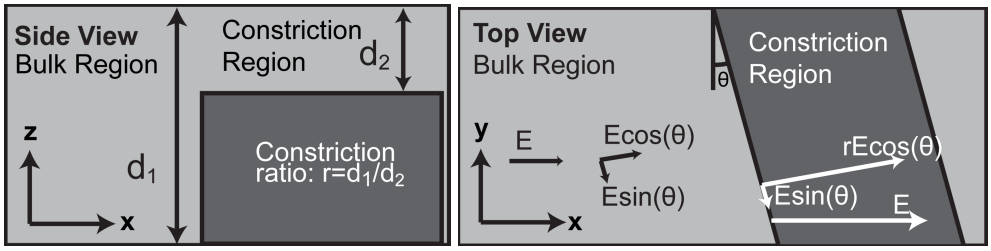

(b) (c)

Figure 3.1: 3.1(a) is a 3D schematic of channel geometry. Inset shows embossed device; note redundant ridges included to reinforce particle deflection (scale bar is 2500μm). In 3.1(b) and 3.1(c), we define relevant geometric factors based on cross-sections of the constriction region along the x-y and x-z planes.

The path of a particle through this system is governed by the relative magnitudes of electrophoretic, electroosmotic, and dielectrophoretic forces. A particle far upstream of the constriction in depth is carried along by electrosmotic fluid flow and electrophoretic particle transport. As a the particle approaches the constriction, DEP forces are applied *perpendicular* to the constriction (nDEP dominates at low field frequencies, which we show in section 3.3.2). Depending on the ratio of linear to nonlinear forces, the particle

will either pass the ridge or be deflected by the ridge. In the case of a trapped particle, there will be a *net* force tangent to the ridge. As the trapped particle moves tangent to the ridge, the angle of incidence changes, and the ratio of linear to nonlinear forces changes; eventually the particle will pass the ridge, at a point determined by the ratio of a particles characteristic linear to nonlinear mobilities.

To mathematically describe this behavior, we present simplified, 3D mobility models for the dominant electrokinetic phenomena: electroosmotic flow, electrophoresis of particles, and dielectrophoresis of particles. These phenomena are actuated by a DC-offset, AC electric field with a single AC frequency, ω_0 (Equation 3.2).

$$\alpha = \frac{|\vec{E}_{AC}|}{|\vec{E}_{DC}|} \tag{3.1}$$

$$\vec{E} = \vec{E}_{DC} + \vec{E}_{AC} \sin \omega_0 t = \vec{E}_{DC} (1 + \alpha \sin \omega_0 t) \tag{3.2}$$

where α is the ratio of AC to DC electric field amplitudes, and $\vec{E}$ describes the electric field specified by voltage applied to reservoirs. The mobility relationships that we use to describe theoretical particle motion are predicated on three main assumptions: thermal motion is small compared to other particle velocity components and can therefore be neglected, particles reach terminal velocity almost instantaneously, and ion concentrations can be described by Boltzmann statistics with a characteristic decay length (characterizing the double layer thickness) that is small compared to particle and channel dimensions.

3.3.1 Linear Electrokinetics

Electroosmosis is the bulk flow of fluid owing to the motion of mobile ions in the double layer, induced by the application of an external electric field. Assuming (i) that the double layer thickness is small compared to characteristic channel dimensions and (ii) that ion distributions can be described by Boltzmann statistics, we obtain the following result to describe the velocity of fluid outside the double layer [26]:

$$\vec{u}_{EO,bulk} = -\frac{\varepsilon_m \zeta}{\eta} \nabla \phi_e = \mu_{EO} \vec{E} \tag{3.3}$$

Equation 3.3 defines an electroosmotic mobility, μ_{EO}, that is dependent on the properties of the fluid and the interface between fluid and channel.

Electrophoresis is the motion of particles in a fluid induced by the application of an external electric field. Applying the same assumptions as above, with the additional condition that a particle reaches terminal velocity against Stokes drag instantaneously, we find [26]:

$$\vec{u}_{EP} = -\frac{\varepsilon_m \zeta_p}{\eta} \vec{E} = -\mu_{EP} \vec{E} \tag{3.4}$$

Equation 3.4 defines an electrophoretic mobility, μ_{EP}, that is dependent on the properties of the fluid and the interface between fluid and particle.

3.3.2 Non-Linear Electrokinetics

Dielectrophoresis refers to the movement of particles as a result of induced or intrinsic particle and fluid multipoles interacting with a non-uniform electric field. We use a dipole approximation and neglect higher order terms in the multipole expansion. We can describe the force on an electric dipole using the conventional dipole moment vector:

$$\vec{F} = (\vec{p} \cdot \nabla)\vec{E} \tag{3.5}$$

For a homogeneous sphere of finite size in a semi-infinite, continuous fluid domain under the influence of a quasi-static, external electric field, we can determine an effective dipole moment, p_{eff} [2] and [3]:

$$\vec{p}_{\text{eff}} = 4\pi\varepsilon_m a^3 \Re[f_{CM}]\vec{E} \tag{3.6}$$

$$f_{CM} = \frac{\varepsilon_p^* - \varepsilon_m^*}{\varepsilon_p^* + 2\varepsilon_m^*} \tag{3.7}$$

$$\varepsilon^* \equiv \varepsilon - \frac{\mathbf{i}\sigma}{\omega} \tag{3.8}$$

Asterisks in the definition of the Clausius-Mossotti factor, f_{CM}, denote the use of complex permittivities as defined in equation 3.8 [2]. The applied electric fields in our simulations and experiment are small in magnitude and frequency such that, as in Equation 3.6, we assume frequency independent values of permittivity, ε, and conductivity, σ, and consider interfacial polarization as a function of complex permittivity, ε^* [2]. By combining this effective dipole moment with the equation for force on a dipole, in an electric field, we obtain:

$$\vec{F}_{DEP} = \pi\varepsilon_m a^3 \Re\left[f_{CM}\right] \nabla\left(\vec{E}\cdot\vec{E}\right) \tag{3.9}$$

This formulation describes the instantaneous dielectrophoretic force. Observed particle motion, however, is the result of the time-averaged force, and is defined by:

$$\left\langle \vec{F}_{DEP} \right\rangle = \frac{1}{T}\int_0^T \pi\varepsilon_m a^3 \Re\left[f_{CM}\right] \nabla\left(\left|\vec{E}_{AC} sin\left(\omega t\right) + \vec{E}_{DC}\right|^2\right) dt \tag{3.10}$$

where T is the period of electric field oscillation and a is the particle radius. The expectation value for the average forces due to electroosmosis and electrophoresis are dependent only on the constant component of the electric field, E_{DC}. If we define the AC to DC ratio as α (Equation 3.1), we can carry out the integration and find:

$$\left\langle \vec{F}_{DEP} \right\rangle = \left(\alpha^2 + 2\right) \pi\varepsilon_m a^3 \Re\left[f_{CM}\right] \nabla\left(\left|\vec{E}_{DC}\right|^2\right) \tag{3.11}$$

Equation 3.11 is cast in terms of a DC electric field and an AC to DC ratio in anticipation of experimental results to follow. The Reynolds number based on the characteristic size of the particle is $\ll 1$, implying Stokes flow. The terminal velocity due to dielectrophoretic forces is thus found by balancing F_{DEP} with the typical formulation for Stokes drag (Equation 3.12), resulting in a definition for the DEP mobility, μ_{DEP}:

$$\begin{aligned} \vec{u}_{DEP} &= \left(\alpha^2 + 2\right) \frac{\varepsilon_m a^2 \Re\left[f_{CM}\right]}{6\eta} \nabla\left(\left|\vec{E}_{DC}\right|^2\right) \\ \vec{u}_{DEP} &= \left(\alpha^2 + 2\right) \mu_{DEP} \nabla\left(\left|\vec{E}_{DC}\right|^2\right) \end{aligned} \tag{3.12}$$

While DEP is most often associated with AC fields, it should be noted at this point

that the dielectrophoretic velocity has contributions from both AC and DC electric fields. The DC component of DEP can be illustrated by setting the AC to DC ratio to zero:

$$\alpha = 0 \Rightarrow \vec{u}_{DEP} = 2\mu_{DEP}\nabla\left(\left|\vec{E}_{DC}\right|^2\right) \tag{3.13}$$

3.3.3 Particle Transport

We have cast electrokinetic velocity components in terms of characteristic mobilities, which we will refer to exclusively throughout the remainder of this paper. We recognize that the relationships between system parameters and mobilities (equations 3.3, 3.4, and 3.12) may, physically, be different from those presented here, but we will reserve examination of those cases for future work.

$$\vec{u} = \vec{u}_{DEP} + \vec{u}_{EO} + \vec{u}_{EP}$$
$$\vec{u} = \mu_{DEP}\nabla\left(\vec{E}\cdot\vec{E}\right) + (\mu_{EO} + \mu_{EP})\vec{E} \tag{3.14}$$

The above equation is composed of (i) terms dependent on the linear electric field and (ii) the DEP term that is dependent on the gradient of the squared electric field. The first order dependence of electroosmosis and electrophoresis on $\vec{E}_{DC}$ leads us to refer to these effects as "linear electromigatory effects." Similarly, the second order dependence of dielectrophoresis on $\vec{E}_{DC}$ leads us to refer to it as a "non-linear electromigratory effect." From equation 3.14, it can be shown that particle velocity is dependent on the DEP, EO, and EP mobilities; the electric field; the gradient of the electric field squared; and the AC to DC ratio α. Inserting the average DEP velocity, we obtain:

$$\vec{u} = \left(\alpha^2 + 2\right)\mu_{DEP}\nabla\left(|E_{DC}|^2\right) + \left(\mu_{EO} + \mu_{EP}\right)\vec{E}_{DC} \tag{3.15}$$

Examining the high and low frequency limits of this equation, we recover the expected relationships for particle dielectrophoretic behavior:

$$\lim_{\alpha\to 0}\vec{u} = 2\mu_{DEP}\nabla\left(|E_{DC}|^2\right) + \left(\mu_{EO} + \mu_{EP}\right)\vec{E}_{DC} \tag{3.16}$$

$$\lim_{\alpha\to\infty}\vec{u} = 2\mu_{DEP}\nabla\left(\frac{\alpha^2}{2}|E_{DC}|^2\right) = 2\mu_{DEP}\nabla\left(|E_{\mathrm{AC,rms}}|^2\right) \tag{3.17}$$

We can safely exclude linear phenomena if the AC to DC ratio, α, is high, as dielectrophoretic effects dominate linear electromigratory effects. At DC however, when the AC to DC ratio is zero, all effects must be retained.

Electric Field Solution

In order to achieve continuous flow particle separation, we modulate electric potential in three dimensions. Accordingly, the complete solution for the electric potential is a three dimensional field that obtained through numerical analysis by solving:

$$\nabla \cdot d^*\nabla\phi^* = 0 \tag{3.18}$$

where d refers to local channel depth and asterisks denote non-dimensionalized parameters. This is a modified laplace equation, developed in [27], that is computationally inexpensive and allows us to obtain a three dimensional solution by parameterizing the third dimension and solving the resulting 2-D equation. We take the gradient of poten-

tial, redimensionalize, and use this solution as $\vec{E}_{DC}$. We then apply equation 3.15 to model particle motion.

While this solution is complete, we recognize that simpler solutions facilitate engineering design. In order to model the effects of various geometric factors, we use a set of simplified solutions, which garner physical insight and allow straightforward comparison between experimental observations and simulated results. We consider two particular cases: (i) an applied potential gradient normal to an infinite constriction in channel depth, that results in particle stagnation and trapping and (ii) an infinite constriction in channel depth at an angle to the applied potential (Figure 3.1(c)) which results in particle motion tangent to the constriction.

Particle Stagnation and Trapping

Particle motion in the presence of an infinitely long constriction in depth normal to the applied potential is simulated with two dimensional techniques and mimicked experimentally with straightforward 2-D fabrication as a constriction in channel width. This allows direct comparison between simulation and experiment, which leads us to a straightforward linearization that aids extension of our 2-D engineering model to three dimensions.

Device operation involves tuning the AC/DC ratio α so that particle motion normal to the ridge is eliminated, causing particles to be deflected by surface ridges in a manner that leads to continuous-flow sorting. We therefore develop relations in this section that specify the α required to stagnate particles at a specific location (α_s) and the α required to stagnate all of the particles in a cross-section of the flow (α_d). The α_d relation, applied normal to a ridge, defines the α required to cause particles to be deflected and sorted by

surface ridges.

The AC/DC ratio α_s required to eliminate the particle velocity component in the x_i direction is a scalar field and can be found by taking the x_i-component of Equation 3.15 and setting the result equal to zero:

$$\alpha_s = \sqrt{-\frac{\hat{x}_i \cdot \vec{E}_{DC}}{\frac{\partial}{\partial x_i}\left(\vec{E}_{DC} \cdot \vec{E}_{DC}\right)} \frac{\mu_{EO} + \mu_{EP}}{\mu_{DEP}} - 2} \tag{3.19}$$

This condition specifies particle stagnation in a specific direction owing to offsetting contributions from the linear and nonlinear electromigratory contributions. A particle is deflected by the surface ridge when its instantaneous velocity normal to the ridge is zero. α_s is small only in regions where the electric field gradients are high (*i.e.,* near the edges of surface ridges), indicating that these regions are the locations where particles will be deflected at AC/DC ratios accessible to experiments.

Complete particle deflection requires that, at the experimental conditions, there be a surface that transects the flow on which the particle motion normal to the ridge is zero. This condition can only be determined in general by solving the Laplace equation for the specified geometry (as specified in the previous section), determining the α required for such a surface to exist, and terming this result α_s. Similar trapping results have been observed and modeled in work by [28, 25, 29]. This exact solution can also be approximated by linearizing the gradient of the electric field magnitude squared:

$$\nabla\left(|\vec{E}|^2\right) \sim \frac{|E_r|^2 - |E|^2}{\gamma} \tag{3.20}$$

which captures the spatial variations of the electric field, approximately, via a shape factor γ (E_r is the electric field in the constriction region, $\propto rE$). With this relation, the

deflection AC to DC ratio α_d is approximated (for a ridge normal to the electric field) by:

$$\alpha_d \sim \sqrt{\frac{1}{|\vec{E}_{DC}|}\frac{\mu_{EO}+\mu_{EP}}{\mu_{DEP}}\frac{\gamma}{(r^2-1)}-2} \tag{3.21}$$

Later results will show that γ is only weakly dependent on ridge height and width, and thus serves as a useful parameter for engineering design. α_d facilitates comparison between numerically simulated and experimentally observed particle behavior.

This representation allows us to clearly deliniate three parameters of interest: $\frac{1}{|\vec{E}_{DC}|}$, the applied electric field, which is an experimental input; $\frac{\gamma}{(r^2-1)}$, geometric factors, which are dictated by the channel geometry; and $\frac{\mu_{EO}+\mu_{EP}}{\mu_{DEP}}$, the mobility ratio, which we are interested in measuring.

The mobility ratio captures electroosmotic, electrophoretic, and dielectrophoretic mobilities, and sorting by this ratio is useful in the biological systems of interest because the perturbations that we are concerned with predominantly affect the DEP mobility rather than electrophoretic mobility [30, 31, 4].

Particle Sorting

The particle stagnation and trapping described in the previous section allows for batch concentration of particles, but not continuous-flow sorting; however, since constrictions in this device are in depth, the geometry allows for another degree of freedom: the angle of incidence. By varying the angle of incidence of the channel constriction spatially, the DEP effects can be used to generate continuous particle sorting. Equation 3.21, above, states that a particle will be repelled from the constriction region by DEP forces

perpendicular to the cross section of a constriction in depth. Applying this description to an angled constriction, we can decompose the bulk electric field and the electric field in the constriction region into normal and tangential components and in the process introduce a dependence on the constriction angle, θ (Figure 3.1(c)). As we did for the 2-D stagnation case, we can define a deflection AC to DC ratio based on the *normal* components of the electric field, by setting the *normal* particle velocity to zero:

$$\alpha_s = \sqrt{-\frac{\hat{n}\cdot\vec{E}_{DC}}{\frac{\partial}{\partial n}\left(\vec{E}_{DC}\cdot\vec{E}_{DC}\right)}\frac{\mu_{EO}+\mu_{EP}}{\mu_{DEP}} - 2} \tag{3.22}$$

Linearizing the gradient term as before, α_d, becomes:

$$\alpha_d \sim \sqrt{\frac{1}{|\vec{E}_{DC}|}\frac{\mu_{EO}+\mu_{EP}}{\mu_{DEP}}\frac{\gamma}{(r^2-1)\cos\theta} - 2} \tag{3.23}$$

For a normal ridge, $\theta = 0^\circ$, and we recover the 2-D solution. We briefly examine the case of two otherwise identical particles with different μ_{DEP} introduced to the same device under identical experimental conditions. We can compare the deflection angles of these particles by equating α_d for the two cases.

$$\cos\theta_2 = \cos\theta_1\frac{\mu_{DEP,1}}{\mu_{DEP,2}} \tag{3.24}$$

The scaling relationships developed in equations 3.21 and 3.23 are important simplifications that allow us to make qualitative predictions regarding the behavior of particles and engineer channel geometries that efficiently accompish our goal of designing a continuous-flow particle sorting device. We show later, that these simplifications are supported by experimental data.

As suggested by equation 3.23, the point at which particles pass the curved ridge is uniquely dependent on the ratio of a particle's electrophoretic and electroosmotic mobilities to dielectrophoretic mobility. By varying the angle of incidence, we modulate the dielectrophoretic component of velocity and couple DEP mobility to transverse position, effectively sorting particles by their mobility ratio. Equation 3.21 allows us to rationally design the constriction ratio of the device such that values of α_d lie within the operability range of our experimental apparatus. Equation 3.23 also suggests that the output distribution of particles is a *continuous* function of DEP mobility, rather than a binary or otherwise discretized output.

3.4 Materials and Methods

3.4.1 Device Fabrication

Device geometries were defined using L-Edit CAD software (Tanner Research). Two mask patterns were created for different etch depths: one to define the channel itself and one to define a pattern of ridges in the channel. Masks were created using standard protocols using GCA/MANN 3600F Optical Pattern Generator and processed with a Hamatech-Steag HMP900 Mask Processor. p-type [100] silicon wafers with 1000nm of thermal oxide (University Wafer) were coated with Shipley 1813 photoresist, spun at 3000rpm for 30 seconds and placed on a hot plate (115°F) for 1 minute. The wafer was then exposed using the depth mask in soft contact using an EV 620 (EV Group) alignment tool. Resist was developed in a Hamatech-Steag Wafer processor with 300MIF developer for 1 minute. The thermal oxide was then chemically etched using 6:1 Buffered Oxide Etch for 15 minutes. The wafer was then cleaned and the resist stripped. The

wafer was recoated and the channel outline pattern exposed. The resist was again developed using 300MIF resist developer and thermal oxide etched again. Now, oxide covers only the regions of the wafer that correspond to regions of full depth; resist covers regions of features in the channel. The wafer was then etched using a Unaxis 700 Bosch etch tool to the desired feature depth. Resist was stripped and the wafer was etched a second time, to the desired channel depth. Remaining thermal oxide was then removed. The wafer was then glued to a glass back for use as a device master.

We have designed and fabricated functional microfluidic devices in polymeric substrates with aspect ratios (250:1) and depths (100μm), higher than previously reported [32][33]. Fabrication was based on procedures adapted from [32] and [33] and employ hot embossing and chemical bonding of Zeonor thermoplastic devices. Plaques of Zeonor 1020R cyclo-olefin copolymer substrate (Zeon Chemicals) were cut using a band saw into 1.5 inch square chips. The silicon device master and a Zeonor chip were aligned and placed in a hot press (Fortin CRC Prepreg) and 1000 lbf was applied at 240°F. The set point temperature was immediately decreased to 195°F and the chip was allowed to cool under load (30 minutes). After the device was removed from the press, access holes were drilled using a drill press and a 1mm end mill at 620rpm to prevent burring and melting. The Zeonor chip was then treated in a solution of 20%vol. *cis- trans*-decahydronaphthalene (Sigma Aldrich) and 80%vol. ethyl alcohol for 30 seconds. Another, blank, Zeonor chip was treated in the same solution for 1 minute. Both were cleaned with ethyl alcohol and dried using compressed nitrogen. The pieces were then immediately placed and aligned in the hot press for bonding. PDMS (poly(dimethylsiloxane)) backing on both sides was used to correct for any deviations in the flatness of the press. PDMS backing material was fabricated using a standard Sylgard 184 Elastomer kit (Dow Corning) and a 5:1 ratio of elastomer to curing agent. After curing, channel shaped holes were cut into the PDMS and aligned with the device

in the press. Bonding was carried out at 140°F, 356lbf for 40 minutes, and the PDMS backing is then discarded.

Reservoirs were fashioned out of 1000μL pipette tips and bonded to the Zeonor plaque using chloroform.

3.4.2 Particle Experiments

Channels were first filled with isopropyl alcohol to facilitate the removal of air bubbles. Deionized water (pH=7) was then run through the devices using positive pressure several times to remove the isopropyl alcohol. 1.7μm FluoresBrite^{TM}(Polysciences) and 2μm Fluosphere^{TM}(Molecular Probes, Invitrogen) carboxylate modified fluorescent polystyrene spheres were introduced in the form of a 100:1 diluted solution of water and spheres. 1.7μm and 2μm spheres fluoresce at different spectra (486nm and 415nm) and were observed using a X-Cite 120 fluorescent source and a Nikon TE2000U inverted microscope. Images and movies were obtained using a Q-Imaging Retiga EXi FAST camera and Phylum software. WaveImage analysis was carried out in MATLAB (MathWorks).

Throughout all experiments, extreme care was taken to eliminate pressure driven flow by equalizing reservoir heights. Observation of stagnant particles was used as an indicator of pressure equalization.

Electric potentials were generated using an Agilent 33220A arbitrary waveform generator and amplified with a Matsusada Precision AP/AS amplifier. Potentials were applied to reservoir solutions through pure platinum electrodes to minimize electrolytic products and measured with a HP 54501A digital oscilloscope.

3.5 Results

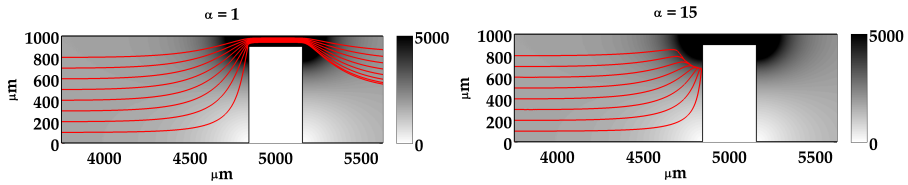

(a) Simulation for $\alpha = 1$.

(b) Simulation for $\alpha = 15$.

Figure 3.2: Simulated particle streamlines (red line) for high and low AC to DC ratios. Background color table corresponds to electric field magnitude. Simulation parameters were: $\phi_{inlet} = 50V$, constriction ratio $= 10:1$, particle radius = $1\mu m$.

We conducted two sets of simulation and experiments. Taken together, these results (i) demonstrate continuous flow particle sorting, (ii) show the effectiveness of the mobility model and approximations in predicting particle behavior, and (iii) provide tools for future engineering design of similar systems. First, we simulated a 2-D geometry with a constriction in depth, using numerical techniques, and determined values for α_s as a function of constriction ratio, r, and constriction shape, γ. Experimentally, we mimicked this geometry with a similar constriction in channel width and measured α_d as a function of constriction ratio and shape. Second, we simulated a curvilinear constriction in channel depth, again using numerical techniques, and determined relative values of θ for different particles. Experimentally, we implemented the same geometry and introduced particles with different μ_{DEP} and measured deflection (θ). The resulting deflection in continuous-flow allowed for particle separation that is a continuous function of μ_{DEP} and transverse channel position.

3.5.1 Particle Trapping

Simulated and experimental observation of the particle trapping response in the presence of a constriction in channel dimensions is consistent with the particle velocity model developed in equation 3.15. We assess the results of simulations using this model to experimental results by comparing α_t values and fitting results with γ as a free parameter in equation 3.21.

Simulation

Applying the 3D particle velocity model derived above and a 2-D electric potential field solution to the microchannel geometry of interest, we can rapidly simulate particle trapping behavior in the presence of a constriction in channel depth. Equation 3.15 predicts that particles will experience deflection in the presence of the constriction, and will pass through the constriction region for low values of α (Figure 3.2(a)) while being excluded from the constriction region for high values of α (Figure 3.2(b)). Simulations were conducted in parametric fashion, varying the constriction ratio, r, from 2 to 20, and the width of the ridge over two orders of magnitude (1 to 100μm). The determination of the trapping AC to DC ratio, α_s, according to equation 3.19, was made by examining particle velocity in the x-direction at $y = 1000\mu m$ (Figure 3.2). This ensures that when the $u_x \leq 0$, particles are completely excluded from the constriction region, defining the trapping threshold for that system. A range of channel constrictions were considered ($2 \leq r \leq 20$), and the simulated data was fit by allowing γ to vary in equation 3.21.

Simulations show that the width is not a significant factor in determining α_t. The critical AC to DC ratio, α_s varies less than 10% as a function of constriction width for each constriction ratio. AC to DC ratios show a strong dependence on the constriction

ratio, and vary in a manner consistent with the scaling arguments presented in equation 3.21. R^2 values for simulated α_s are ≥ 0.98 (Figure 3.3).

Experiment

Microfluidic channels were fabricated in Zeonor 1020R polymer with constrictions in width, corresponding to variations in constriction ratio in simulated geometries. Subsequently, the motion of $2\mu m$ diameter polystyrene spheres was observed at increasing AC to DC ratios. α_t values where particles were excluded from the constriction region were recorded and compared to those predicted from 3D analytical results and 2-D simulation. Comparison between experimental values of α_t and those predicted by equation 3.21 show good correspondence (Figure 3.3). The agreement between theory, simulation, and experiment supports the use of equation 3.21 as a design tool for future work.

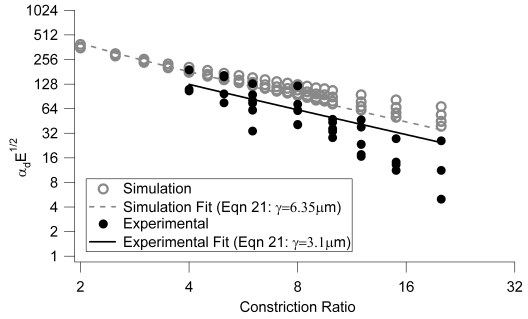

Figure 3.3: Simulated and experimental values of $\alpha_t \sqrt{E_{DC}}$ show good fit quality and expected dependence on r and γ. Multiplication of α_t by $\sqrt{E_{DC}}$ emphasizes the dependence of E and α_t on factors determined by channel geometry: γ and r. Scatter in simulated data points is attributable to minor effects of constriction width (Section 3.5.1).

3.5.2 Single Particle Deflection

The particle velocity model, from section 3.3.3, in addition to predicting trapping in the presence of a simple constriction, predicts particle deflection along an angled ridge, which we observe in simulation and experiment by varying the AC to DC ratio, α.

Simulation

Particle deflection behavior (i.e., particle motion along an angled ridge) was simulated by applying the 3D particle velocity model and a quasi-2D electric potential field solution technique to the microchannel geometry of interest. The geometry of interest is a curved constriction in channel depth described in section 3.3.3 and Figure 3.1. Using equation 3.15, derived above, and a numeric solution for equation 3.18 over the geometry of interest, we simulate particle motion in the presence of a curved constriction in channel depth. Appropriate redimensionalization requires values for particle and wall zeta potentials, which we obtain through light scattering (Malvern Zetasizer) and streaming potential [25, 34, 35], respectively. The Clausius-Mossotti factor, f_{CM}, for these particles is assumed to be -0.5 in the low frequency limit, since $\sigma_{\text{polystyrene}} \ll \sigma_{\text{fluid}}$. Plotting streamlines from the velocity solution, we show that particle deflection along the y-axis is dependent on the AC to DC ratio, α, as described in section 3.3.3, above (Figure 3.4).

Experiment

A microchannel with a curved constriction in channel depth was fabricated and particle deflection along the y-axis as a function of the AC to DC ratio was observed. The degree of transverse (y-axis) deflection as a function of θ and α is characterized by

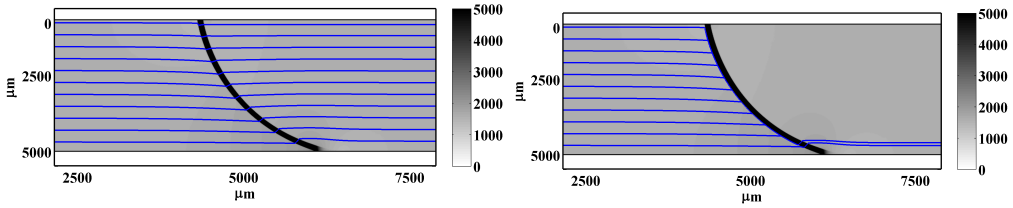

(a) $\alpha = \alpha_{low}$ (b) $\alpha = 3.16 * \alpha_{low}$

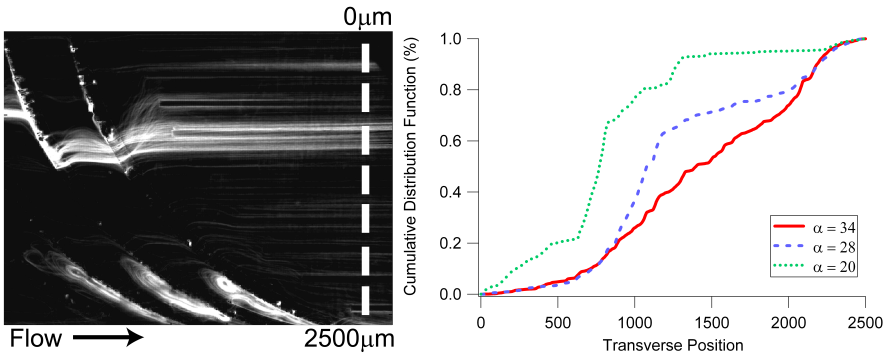

(c) 2μm particles (d)

Figure 3.4: Varying the value of the AC to DC ratio, α, causes increased transverse (y-axis) deflection. Simulated particle pathlines in 3.4(a) show no net particle deflection at ridge with a low AC to DC ratio. 3.4(b) shows particle deflection tangent to a curved constriction in channel depth, transverse to the direction of flow for a high AC to DC ratio. 3.4(c) shows experimental deflection of an input particle stream by multiple, redundant ridges. 3.4(d) shows experimental distribution functions of intensity along dashed line in 3.4(c) for three values of α.

measuring time lapse ($\geq$ 30 frames, Figure 3.4(c)) fluorescence image intensity along the y-axis at the channel outlet and computing a running integral of image intensity. Curves for several AC to DC ratios compare the degree of separation and demonstrate the predicted dependence of deflection of the AC to DC ratio, α (Figure 3.4(d)). The cumulative distribution function is computed as a running integral of normalized image intensity and corresponds to a percentage of total exiting particles as a function of y-axis position.

3.5.3 Particle Separation

Particle deflection behavior in continuous-flow (as opposed to stagnation/trapping presented above) is dependent on individual particle characteristics; specifically, the ratio of linear to non-linear electrokinetic mobilities 3.22.

Simulation

Particle deflection behavior is dependent on a number of particle-specific properties that determine the electrophoretic and dielectrophoretic mobilities and is controlled by the magnitudes of the DC and AC electric field components (E_{DC} and E_{AC}). Based on this dependence, and equation 3.15 combined with quasi-2D electric potential solutions, we predict particle sorting behavior that is a function of differences in the ratio of dielectrophoretic to electrophoretic and electroosmotic mobility. A dimensional simulation, carried out as described in section 3.3.3, for a constant AC to DC ratio, shows deflection that is dependent on particle size (Figure 3.4).

Experiment

Separation of 2- and 3μm particles was accomplished in continuous flow using the device shown in Figure 3.1. As described in section 3.5.2, deflection can be characterized by calculating a cumulative distribution function for time lapse fluorescence intensity at the channel outlet. Intensities of 2- and 3μm particles were measured and normalized independent from one another prior to comparison. Figure 3.5 shows particle separation from a localized input stream of mixed particles. The degree of deflection of both particles can be modulated by changing the AC to DC ratio or field magnitudes. At lower values of α, 2μm particles remain at the top of the channel while 3μm particles are

deflected. As α is increased, the deflection of $3\mu m$ particles continues to increase until they reach the bottom of the channel. Deflection of $2\mu m$ particles can then be modulated as a function of α.

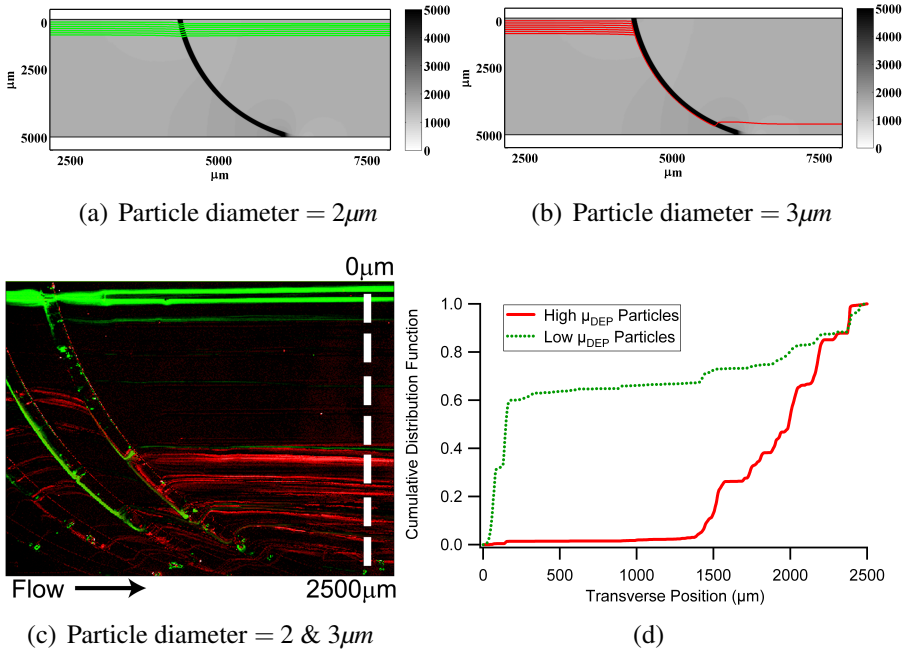

(a) Particle diameter $= 2\mu m$ (b) Particle diameter $= 3\mu m$

(c) Particle diameter $= 2$ & $3\mu m$ (d)

Figure 3.5: Background color table in 3.5(a) and 3.5(b) represents $|E_{DC}|$. Simulation parameters were: $\phi_{inlet} = 25V$, constriction ratio $= 10:1$, and $\alpha = 4$. 3.5(c) $2\mu m$ (green) particles pass redundant ridges with no net deflection while $3\mu m$ (red) particles show significant net deflection as expected due to higher DEP mobility. 3.5(d) shows experimental distribution functions of intensity along dashed line in 3.5(c).

3.6 Discussion

We have demonstrated (i) continuous-flow separation of particles, (ii) agreement between theory, simulation, and experiment, and (iii) simple modeling relationships for engineering design. Particle deflection and trapping were shown to be functions primarily of constriction ratio with minor contributions from other geometric factors.

The use of DC-offset AC electric fields allows independent modulation of linear electromigratory effects and non-linear dielectrophoretic effects. Increasing α controls the degree of y-axis deflection and can be used to control the location of the separated output streams.

The sorting demonstrated is a function of several mobilities, including linear and nonlinear electrokinetic particle mobilities (μ_{EP} and μ_{DEP}), which may vary independently for a given sample. By including additional EP mobility and size distribution measurements to define operating parameters, viable separation based on DEP mobility alone can be accomplished. Variations of size and EP mobility, for an isolated bacterial cell sample, are generally small compared to the expected variation in DEP mobility[30, 31, 4]. Furthermore, we avoid many of these difficulties by examining bacterial cells within a single species from a homogeneous and well characterized initial sample.

While insulator-based dielectrophoretic techniques (iDEP) have been reported by others, few use 3D device geometries for continuous flow particle processing. [36] reported the use of iDEP at low field frequencies to trap single- and double-stranded DNA in an array of insulating posts. Similarly, [28] reported the use of iDEP and DC electric fields to trap and distinguish bacterial species and to separate live from dead bacteria [28]. [25] reported similar results using a polymeric post array. Trapping and binary separation techniques such as these have the advantage of robust operation and ease of fabrication, but typically require higher electric fields than electrode based techniques to generate similar electric field gradients. Additionally, obtaining separated samples is frustrated by the fact that samples are separated temporally in a flow, rather than spatially. [23, 27] report the use of DC electric fields in an array of insulating posts with different angles of incidence to the direction of flow. The result is a spatial sep-

aration based on statistical averaging of DEP effects over all post-constrictions in the array. Similarly, this technique requires high electric fields to generate gradients, but achieves spatial sample separation, albeit over the length of the post array. [19] reported the separation of particles based on size over a "hurdle" in the channel. This "hurdle" is analagous to the constriction described above in section 3.3.3. By applying a DC electric field, the hurdle/constriction causes a net change in the particle trajectory [20] which was used to separate particles with a significant difference in size. This device achieves a separation based on particle size, but with relatively low sensitivity due to the magnitude of DEP force imposed on particles. By relying on exclusion due to the constriction and varying the angle of ridge incidence, the device reported in section 3.3.3 trades dynamic range for higher sensitivity to changes in DEP mobility.

Electrode-based DEP trapping techniques are well established, but still developing, with new electrode and device geometries rapidly emerging. A full review of these advances is beyond the scope of this text, and the authors would direct the reader to Voldman's review of biologically relevant DEP phenomena [4]. Notable work on the characterization of multipolar electrode arrays for DEP trapping and analysis is found in [12, 13, 14]. The use of multipolar and 3D electrode configurations to trap cells has been investigated extensively by Fuhr and co-workers [6, 7, 8, 9, 10, 11].

Of note, due to its similarity to the present work, are two reported devices: one is a continuous-flow separation technique using microfabricated, in-channel electrodes in the place of the curved ridge [24]. An array of interdigitated, linear electrodes are patterned in the channel and generate electric field gradients which interact periodically with particles to effect separation based on DEP mobility. The second uses insulative constrictions in channel depth to preferentially deflect particles based on the ratio of DEP to EO and EP mobilities [21, 22]. These devices are fabricated in glass and achieve

a binary separation. By using polymeric substrates, 3D geometries, and AC electric fields, we reduce the cost and difficulty of manufacture, achieve a continuous (rather than discrete) separation, and introduce increased experimental flexibility by changing the applied field frequency.

3.7 Conclusion

To the authors knowledge, this is the first reported use of 3D, insulative techniques to affect a continuous-flow particle separation whose output is characterized by continuous variation of dielectrophoretic mobility perpendicular to the direction of flow. We developed a set of theoretical approximations to be used in the design of similar microfluidic systems for the manipulation of particles using insulative dielectrophoresis, coupled with electrophoresis and electroosmosis for fluid and particle transport. We applied this model to the design and development of continuous-flow dielectrophoretic sorting devices with 3-dimensional modulation of electric fields. Theoretical and experimental results were compared by measuring the trapping threshold value, α_t, in simulation and experiment. Measurement of α_t is a straightforward method of characterization compared to tracking single particles or a statistical average of particles, and applies directly to the particle sorting device (Figure 3.1). Devices were fabricated with aspect ratios higher than previously reported for bonded thermoplastic devices (250:1, width-to-depth). Device functionality was verified by sorting 1.7μm and 2μm polystyrene spheres with similar material and surface properties. Good correspondence between the model, simulation, and experiment was found. The advantage of 3D modulation of electric fields is the resulting continuous variation of particle mobility ratios transverse to the direction of flow. This output can be separated into any number of output channels, yielding the potential for unprecedented resolution for a single separation.

3.8 Acknowledgements

The authors acknowledge the valuable input of Blake Simmons, Sandia National Laboratories, in the development of polymer fabrication techniques, and Eric Cummings, Sandia National Laboratories, in conceptual design.

BIBLIOGRAPHY

[1] Benjamin G Hawkins, A Ezekiel Smith, Yusef A Syed, and Brian J Kirby. Continuous-flow particle separation by 3D Insulative dielectrophoresis using coherently shaped, dc-biased, ac electric fields. *Analytical chemistry*, 79(19):7291–7300, October 2007.

[2] Herbert A Pohl. *Dielectrophoresis: The behavior of neutral matter in nonuniform electric fields*. Cambridge University Press, 1978.

[3] Thomas B Jones. *Electromechanics of Particles*. Cambridge University Press, New York, 1995.

[4] J Voldman. Electrical forces for microscale cell manipulation. *Annual review of biomedical engineering*, 8:425–54, 2006.

[5] Elizabeth R Rhoades, Rachel E Geisel, Barbara A Butcher, Sean McDonough, and David G Russell. Cell wall lipids from Mycobacterium bovis BCG are inflammatory when inoculated within a gel matrix: characterization of a new model of the granulomatous response to mycobacterial components. *Tuberculosis (Edinburgh, Scotland)*, 85(3):159–76, May 2005.

[6] Stefan Fiedler, Stephen G. Shirley, Thomas Schnelle, and Günter Fuhr. Dielectrophoretic Sorting of Particles and Cells in a Microsystem. *Analytical Chemistry*, 70(9):1909–1915, May 1998.

[7] Günter Fuhr, W. Michael Arnold, Rolf Hagedorn, Torsten Müller, Wolfgang Benecke, Bernd Wagner, and Ulrich Zimmermann. Levitation, holding, and rotation of cells within traps made by high-frequency fields. *Biochimica et Biophysica Acta (BBA) - Biomembranes*, 1108(2):215–223, July 1992.

[8] G. Fuhr, H Glasser, T Muller, and T Schnelle. Cell manipulation and cultivation under a.c. electric field influence in highly conductive culture media. *Biochimica et Biophysica Acta (BBA) - General Subjects*, 1201(3):353–360, December 1994.

[9] Guenter Fuhr, Rolf Hagedorn, Torsten Mueller, and Thomas Schnelle. Microelectrode arrangements for production of functional field barriers during dielectrophoresis, 2000.

[10] G Fuhr. High-frequency electric field trapping of individual human spermatozoa. *Human Reproduction*, 13(1):136–141, January 1998.

[11] T Müller. A 3-D microelectrode system for handling and caging single cells and particles. *Biosensors and Bioelectronics*, 14(3):247–256, March 1999.

[12] J Voldman. *Dielectrophoretic Traps for Cell Manipulation*, volume 4, chapter 8, pages 159–186. Springer US, 2007.

[13] J Voldman. Design and analysis of extruded quadrupolar dielectrophoretic traps. *Journal of Electrostatics*, 57(1):69–90, January 2003.

[14] J Voldman. Holding Forces of Single-Particle Dielectrophoretic Traps. *Biophysical Journal*, 80(1):531–542, January 2001.

[15] P Gascoyne, J Satayavivad, and M Ruchirawat. Microfluidic approaches to malaria detection. *Acta Tropica*, 89(3):357–369, February 2004.

[16] Peter R C Gascoyne and Jody Vykoukal. Particle separation by dielectrophoresis. *Electrophoresis*, 23(13):1973–83, July 2002.

[17] Enzhu Liang, Rosemary Smith, and David Clague. Dielectrophoretic manipulation of finite sized species and the importance of the quadrupolar contribution. *Physical Review E*, 70(6):0, December 2004.

[18] E Richter, G Fuhr, T. Muller, S Shirley, S. Rogaschewski, K. Reimer, and C. Dell. Growth of anchorage-dependent mammalian cells on microstructures and microperforated silicon membranes. *Journal of Materials Science: Materials in Medicine*, 7(2):85–97, February 1996.

[19] Kwan Hyoung Kang, Yuejun Kang, Xiangchun Xuan, and Dongqing Li. Continuous separation of microparticles by size with direct current-dielectrophoresis. *Electrophoresis*, 27(3):694–702, 2006.

[20] Kwan Hyoung Kang, Xiangchun Xuan, Yuejun Kang, and Dongqing Li. Effects of dc-dielectrophoretic force on particle trajectories in microchannels. *Journal of Applied Physics*, 99(6):064702, 2006.

[21] Louise M Barrett, Andrew J Skulan, Anup K Singh, Eric B Cummings, and Gregory J Fiechtner. Dielectrophoretic manipulation of particles and cells using insulating ridges in faceted prism microchannels. *Analytical chemistry*, 77(21):6798–804, 2005.

[22] Louise M Barrett, Andrew J Skulan, Anup K Singh, Eric B Cummings, and Gre-

gory J Fiechtner. Dielectrophoretic manipulation of particles and cells using insulating ridges in faceted prism microchannels., November 2005.

[23] E B Cummings. Streaming dielectrophoresis for continuous-flow microfluidic devices. *Ieee Engineering in Medicine and Biology Magazine*, 22(6):75–84, 2003.

[24] Jason G Kralj, Michael T W Lis, Martin a Schmidt, and Klavs F Jensen. Continuous dielectrophoretic size-based particle sorting. *Analytical chemistry*, 78(14):5019–25, July 2006.

[25] Petra Mela, Albert van Den Berg, Yolanda Fintschenko, Eric B Cummings, Blake A Simmons, and Brian J Kirby. The zeta potential of cyclo-olefin polymer microchannels and its effects on insulative (electrodeless) dielectrophoresis particle trapping devices. *Electrophoresis*, 26(9):1792–9, May 2005.

[26] Ronald F Probstein. *Physicochemical Hydrodynamics*. Wiley-interscience, 2nd edition, 1994.

[27] Eric B Cummings and Anup K Singh. Dielectrophoresis in Microchips Containing Arrays of Insulating Posts: Theoretical and Experimental Results. *Analytical Chemistry*, 75(18):4724–4731, 2003.

[28] Blanca H Lapizco-Encinas, Blake A Simmons, Eric B Cummings, and Yolanda Fintschenko. Insulator-based dielectrophoresis for the selective concentration and separation of live bacteria in water. *Electrophoresis*, 25(10-11):1695–704, 2004.

[29] Jonas O Tegenfeldt, Christelle Prinz, Han Cao, Richard L Huang, Robert H Austin, Stephen Y Chou, Edward C Cox, and James C Sturm. Micro- and nanofluidics for DNA analysis. *Analytical and bioanalytical chemistry*, 378(7):1678–92, April 2004.

[30] M J Smeulders, R A Speight, Jacquie Keer, and H D Williams. Adaptation of Mycobacterium smegmatis to stationary phase. *Journal of bacteriology*, 181(1):270–83, January 1999.

[31] Darren Lytle, Christy Frietch, and Terry Covert. Electrophoretic Mobility of Mycobacterium avium Complex Organisms. *Applied and environmental microbiology*, 70(9):5667–71, September 2004.

[32] Mandy B Esch, Sahil Kapur, Gizaida Irizarry, Vincent Genova, and Cornell Nanofabrication Facility. Influence of master fabrication techniques on the

characteristics of embossed microfluidic channels. *Lab on a chip*, 3(2):121–7, 2003.

[33] Thomas I Wallow, Alfredo M Morales, Blake A Simmons, Marion C Hunter, Karen Lee Krafcik, Linda A Domeier, Shane M Sickafoose, Kamlesh D Patel, and Andy Gardea. Low-distortion, high-strength bonding of thermoplastic microfluidic devices employing case-II diffusion-mediated permeant activation. *Lab on a chip*, 7(12):1825–31, December 2007.

[34] Brian J Kirby and Ernest F Hasselbrink. Zeta potential of microfluidic substrates: 1. Theory, experimental techniques, and effects on separations. *Electrophoresis*, 25(2):187–202, January 2004.

[35] Brian J Kirby and Ernest F Hasselbrink. Zeta potential of microfluidic substrates: 2. Data for polymers. *Electrophoresis*, 25(2):203–13, January 2004.

[36] C Chou, J Tegenfeldt, S Chan, O Bakajin, E Cox, N Darnton, R Austin, and T Duke. Electrodeless Dielectrophoresis of Single- and Double-Stranded DNA. *Biophysical Journal*, 83(4):2170–2179, October 2002.

CHAPTER 4

ELECTROTHERMAL FLOW EFFECTS IN INSULATING (ELECTRODELESS) DIELECTROPHORESIS SYSTEMS

4.1 Abstract

We simulate electrothermally induced flow in polymeric, insulating dielectrophoresis (iDEP) systems with DC-offset, AC electric fields at finite thermal Péclet number, and we identify key regimes where electrothermal effects enhance particle deflection and trapping. We study a single, two-dimensional constriction in channel depth with parametric variations in electric field, channel geometry, fluid conductivity, particle electrophoretic (EP) mobility, and channel electroosmotic (EO) mobility. We report the effects of increasing particle EP mobility, channel EO mobility, and AC and DC field magnitudes on the mean constriction temperature and particle behavior. Specifically, we quantify particle deflection and trapping, referring to the deviation of particle from their pathlines owing to dielectrophoresis as they pass a constriction and the stagnation of particles owing to negative dielectrophoresis (nDEP) near a constriction, respectively. This work includes the coupling between fluid, heat, and electromagnetic phenomena via temperature-dependent physical parameters. Results indicate that the temperature distribution depends strongly on the fluid conductivity and electric field magnitude, and particle deflection and trapping depend strongly on the channel geometry. Electrothermal effects perturb the electroosmotic flow field, creating vorticity near the channel constriction and enhancing the deflection and trapping effects. Electrothermal effects alter particle deflection and trapping responses in iDEP devices, especially at intermedi-

[0]The content of this chapter was submitted and accepted for publication as a research article "Electrothermal flow effects in insulating (electrodeless) dielectrophoresis systems" in the journal *Electrophoresis*. This is a pre-peer reviewed version of the article. Reproduced with permission from *Electrophoresis*, in press. Unpublished work copyright 2010 Wiley-VCH.

ate device aspect ratios ($2 \leq r \leq 7$) in solutions of higher conductivity ($\sigma_m \geq 1 \times 10^{-3}$ S/m). The impact of electrothermal effects on particle deflection and trapping are diminished when particle EP mobility or channel EO mobility is high. In almost all cases, electrothermal effects enhance negative dielectrophoretic particle deflection and trapping phenomena.

4.2 Introduction

Dielectrophoresis (DEP) is the transport of polarized particles in response to a nonuniform electric field, exclusive of electrophoresis [1]. DEP forces depend on the magnitude and nonuniformity of the electric field, as well as the complex permittivity of a particle and its surrounding media [2]. The complex permittivities ($\tilde{\varepsilon} = \varepsilon - i\sigma/\omega$) of the particle and surrounding media are a function of the frequency of the polarizing electric field; the permittivity, ε, is assumed independent of frequency in most DEP experiments [3]. The combination of material- and frequency dependence makes DEP a useful technique for researchers attempting to manipulate, separate, and characterize particles and cells. DEP devices have been used to characterize and separate a variety of species [4], e.g. bacterial populations [5, 6, 7, 8], mammalian cells [9, 10, 11, 12], DNA [13], proteins [14, 15, 16, 17], and viruses [18].

Electric field nonuniformities in DEP devices are most often generated via microfabricated electrodes (electrode-based DEP, eDEP) or insulating constrictions in channel cross-sectional area (insulator-based DEP, iDEP). eDEP devices rely on microfabricated electrodes embedded within the fluid channel. iDEP devices rely on macroscopic electrodes placed in external reservoirs, making device fabrication less time-consuming and less expensive. Devices can be fabricated via hot-embossing in low-cost polymeric sub-

strates in a matter of hours (after making a silicon master) [19]; even glass iDEP devices, which require longer fabrication processes, are relatively low-cost because they do not require internal, microfabricated electrodes. iDEP devices can be made from a variety of materials — from glass and silicon to polymers like Zeonor and polycarbonate. Compared to eDEP devices, iDEP devices require relatively large electric potentials to generate equivalent electric fields, limiting the range of field frequencies owing to the slew-rate limitations of high-voltage equipment. Recent work has shown that DC-offset, AC electric fields (of low-frequency) can enhance the operation of iDEP devices by decoupling electroosmotic and electrophoretic effects from DEP [19, 20]. We have previously demonstrated continuous-flow iDEP separation of polystyrene microspheres in Zeonor devices using DC-offset, AC electric fields [19]. As researchers continue to apply iDEP techniques to cellular analysis, it becomes increasingly relevant to investigate the potentially confounding effects of Joule heating and electrothermal flow.

Dielectrophoresis, either in electrode-based or insulating devices, is achieved by subjecting samples to a nonuniform electric field. Therefore, localized Joule heating is ever-present and particularly significant in high-conductivity solutions actuated by high electric fields, as is often desirable in cellular experiments in DEP devices. In addition to the temperature-specific implications for cellular response and viability, localized Joule heating creates gradients in temperature-dependent media properties, leading to electrothermally induced fluid motion [21]. Although some researchers have used Joule heating to facilitate PCR and chemical reactions, or leveraged electrothermal (ET) flows to enhance particle trapping [22, 23] and pump fluids [24, 25], most avoid these effects by using low-conductivity solutions to minimize Joule heating.

In eDEP systems, electrothermal forces manifest as localized regions of recirculation. Locally recirculating regions have been observed via analyte or tracer particles

[23, 26, 27, 28, 29, 30] and predicted via numerical simulation [31, 32, 33, 34, 24, 30, 35]. Experimental observations of recirculatory motion exhibited by trapped particles in iDEP devices have been anecdotally attributed to electrothermal effects, but no effort to date has modeled or experimentally confirmed this explanation. The majority of experimental and numerical works in eDEP devices do not consider the fully-coupled thermal-fluid-electrical problem, electing instead to solve the systems sequentially, solving for the electric field, then the resulting temperature field, and finally the induced electrothermal flow field. In many cases, the independent solutions approach is appropriate, owing to the low thermal-Péclet number, Pe_T. In iDEP systems, however, Pe_T is not small and thus we consider the fully-coupled problem.

Because electrothermal flow can affect the use of iDEP devices for particle and cellular analysis, we present a numerical investigation of electrothermal flow in insulator-based dielectrophoresis systems with the goals of determining the magnitude of electrothermal forces and examining their impact on particle deflection and trapping. Deflection (the deviation of particles from their pathlines owing to DEP as they pass a constriction) and trapping (the stagnation of particles owing to negative DEP near a constriction) are the two modes of negative DEP actuation common in iDEP systems. In modeling electrothermal flow at finite Pe_T, we simulate the coupling of thermal, electrical, and fluid mechanical systems. As a basis for our analysis, we choose a constriction in channel depth because it is commonly used (Figure 4.1) for particle manipulation [36, 37, 38, 39, 40, 41].

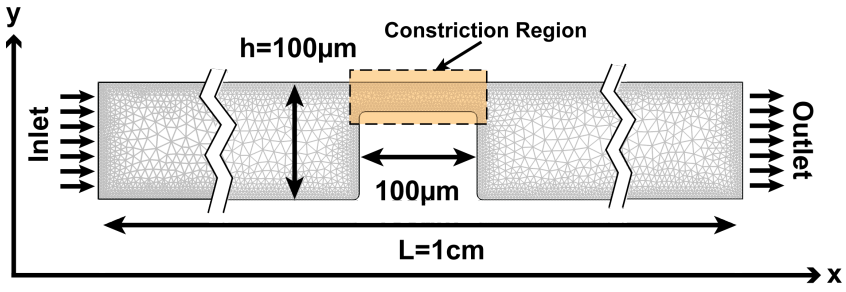

Figure 4.1: Insulating constriction geometry showing inlet, outlet, flow direction, and constriction region. Mesh shown is used in numerical simulations on the fluid domain. Axes are used as reference directions throughout this work.

4.3 Theory

In this section, we present three sets of coupled equations representing the physics of fluid, electrical, and thermal formulae as applied to the commonly used insulating constriction geometry [36, 37, 38, 40]. We present first the physical equations, then discuss appropriate approximations, and finally present the specific expressions used for numerical simulations in this work. We will re-express the general governing equations in terms of a DC-offset, AC electric field, which is relevant to our previous work [19]. The insulating constriction is considered in two dimensions with variation in the constriction height.

Temperature is the primary coupling variable between electrical, fluid, and thermal governing equations: heat is generated as a result of the applied electric field by Joule heating; this heat is conducted through the channel walls or convected via pressure-driven flow, electroosmotic flow, electrothermally induced flow, or combinations thereof. We consider the following temperature-dependent material properties: electrical conductivity (σ_m), electrical permittivity (ε_m), thermal conductivity (k_m), specific heat (C_p), and viscosity (η). Local variations in these material properties influence the resulting fluid, thermal, and electrical physics: (i) the electrothermal body force

and electroosmotic flow velocity depend on σ_m and ε_m, (ii) the heat flux depends on k_m and C_p, and (iii) the electric field and Joule heating depend on σ_m and ε_m. This coupling forms a nonlinear relationship between the three sets of governing equations (fluid, electrical, and thermal).

4.3.1 Electromagnetics

The governing equations for electrokinetic and electrothermal phenomena discussed here are the quasi-static Maxwell's equations for inhomogeneous materials. We consider sinusoidal electric fields of single and multiple frequencies. For simplicity, we express quantities, such as the electric field, in complex notation when we are deriving frequency-dependent expressions. Generally,

$$\begin{aligned} \mathbf{E}(t,\omega) &= \Re\left[\tilde{\mathbb{E}}\exp(i\omega t)\right] \\ \mathbf{E}(t,\omega_0,\omega_1,...,\omega_n) &= \Re\left[\sum_n \tilde{\mathbb{E}}_n \exp(i\omega_n t)\right] \end{aligned} \tag{4.1}$$

where $\Re[\cdots]$ isolates the real component of $[\cdots]$, $\tilde{\mathbb{E}} = \mathbb{E}\exp(i\vartheta)$ is the electric field phasor containing spatially dependent phase information, and the tilde ($\tilde{f}$) denotes a complex quantity. In this work, the electric field phase is uniform and so $\vartheta = 0$ and $\tilde{\mathbb{E}}$ is purely real. We will use these complex expressions to present general analytical results and use their time-averaged real component for numerical computation.

In the absence of accelerating charge (this quasi-static assumption is valid where the wavelength of the electromagnetic field is large compared to the size of the system [42], and implies $\nabla \times \mathbf{E} = -\partial\mathbf{B}/\partial t = 0$), Gauss's law (Equation 4.2) and charge conservation (Equation 4.3) are written as

$$\nabla \cdot (\varepsilon_m \mathbf{E}) = \rho_e \tag{4.2}$$

$$\nabla \cdot (\sigma_m \mathbf{E} + \rho_e \mathbf{u}) + \frac{\partial \rho_e}{\partial t} = 0 \tag{4.3}$$

where bolded variables denote vector fields, ρ_e is volumetric charge density, and the $\rho_e \mathbf{u}$ term represents the convective charge flux density. We neglect charge transport due to diffusion because it is dominated by charge transport due to electrophoresis. Following Ramos, et al. [43] we additionally assume that ohmic current ($\sigma_m \mathbf{E}$) rearranges charge faster than fluid flow ($\rho_e \mathbf{u}$). Therefore, in the remainder of this work, we neglect the convection of charge due to fluid motion.

4.3.2 Hydrodynamics

We describe the time-averaged hydrodynamics of electroosmotic and electrothermal fluid flow using the time-averaged Navier-Stokes equations with appropriate boundary conditions. For incompressible fluids [44]:

$$\rho_m \left(\frac{\partial \mathbf{u}}{\partial t} + \mathbf{u} \cdot \nabla \mathbf{u} \right) = -\nabla p + \nabla \cdot (\eta \nabla \mathbf{u}) + \mathbf{f} \tag{4.4}$$

where ρ_m is mass density, η is the dynamic viscosity, p is time-averaged pressure, $\mathbf{u}$ is the time-averaged fluid velocity, and $\mathbf{f}$ is a volumetric body force. In this work we consider only flows where the time-averaged fluid velocity is constant ($\partial \mathbf{u}/\partial t = 0$).

Electroosmotic Flow

Electroosmosis is often used to drive fluid motion in microfluidic systems and arises owing to the electrophoretic motion of mobile counterions accumulated in the double layer near the channel wall. For system sizes that are large ($10-100\mu$m) compared to the double layer ($\lambda_D \sim 10$nm), fluid motion outside the double layer can be approximated via a slip boundary condition on the bulk fluid according to the Smoluchowski equation [45]:

$$\mathbf{u}_{EO} = -\frac{\varepsilon_m \zeta_w}{\eta}\mathbf{E} \tag{4.5}$$

$$\mu_{EO} = -\frac{\varepsilon_m \zeta_w}{\eta} \tag{4.6}$$

at the interface. We define an electroosmotic mobility, μ_{EO}, and a phenomenological potential, ζ_w, that defines the no-slip boundary condition applied within the electrical double layer [46, 47]. We assume that the thickness of the double layer does not change significantly — relative to the size of the channel — as a function of temperature and that ζ_w is independent of temperature.

Electrothermal Flow

Electrothermal flow arises in systems with nonuniform permittivity and conductivity. In such a system, a local charge distribution must be present if Gauss's Law (Equation 4.2) and charge conservation are to be satisfied simultaneously. This local charge density responds to the applied electric field, resulting in a non-zero body force on the fluid:

$$\mathbf{f}_{ET} = \rho_e \mathbf{E} - \frac{1}{2}|\mathbf{E}|^2 \nabla \varepsilon_m \tag{4.7}$$

The first and second terms on the right-hand side express the Coulomb force on free and bound charges, respectively. Following the analysis of Ramos, et al. [43], we perform a perturbative expansion of the electric field around this isothermal solution. We assume that changes to ε_m and σ_m are small and consider a small perturbation, $\mathbf{E}_1$, to the electric field, $\mathbf{E}_0$, that would be present in the isothermal case: $\mathbf{E} = \mathbf{E}_0 + \mathbf{E}_1$ where $|\mathbf{E}_1| \ll |\mathbf{E}_0|$. The isothermal solution is assumed to be electroneutral ($\nabla \cdot \mathbf{E}_0 = 0$), therefore small perturbations in the charge density are associated only with $\mathbf{E}_1$. As a result we write the charge density (from Gauss's Law, Equation 4.2) as:

$$\rho_e = \nabla \varepsilon_m \cdot \mathbf{E}_0 + \varepsilon_m \nabla \cdot \mathbf{E}_1 \tag{4.8}$$

The continuity equation (4.3) can be expanded as:

$$\nabla \sigma_m \cdot \mathbf{E}_0 + \sigma_m \nabla \cdot \mathbf{E}_1 + \frac{\partial}{\partial t}\left(\nabla \varepsilon_m \cdot \mathbf{E}_0 + \varepsilon_m \nabla \cdot \mathbf{E}_1\right) = 0 \tag{4.9}$$

We further expand this representation to include an electric field with multiple sinusoidal components, take the Fourier transform with respect to time ($\mathcal{F}[\mathbf{E}] = \underline{\mathbf{E}}$), and solve for $\nabla \cdot \underline{\mathbf{E}_1}$:

$$\begin{aligned} 0 &= \nabla \sigma_m \cdot \underline{\mathbf{E}_0} + \sigma_m \nabla \cdot \underline{\mathbf{E}_1} + i\omega\left(\nabla \varepsilon_m \cdot \underline{\mathbf{E}_0} + \varepsilon_m \nabla \cdot \underline{\mathbf{E}_1}\right) \\ \nabla \cdot \underline{\mathbf{E}_1} &= \frac{-(\nabla \sigma_m + i\omega \nabla \varepsilon_m) \cdot \underline{\mathbf{E}_0}}{\sigma_m + i\omega \varepsilon_m} \end{aligned} \tag{4.10}$$

from this we can write the Fourier transform of the charge density as:

$$\underline{\rho_e} = \frac{(\sigma_m \nabla \varepsilon_m - \varepsilon_m \nabla \sigma_m) \cdot \underline{\underline{\mathbf{E}_0}}}{\sigma_m + i\omega\varepsilon_m} \tag{4.11}$$

Note that ω is the independent variable in frequency space and not equivalent to ω_n in Equation 4.1. Returning to the time domain by applying the inverse Fourier transform ($\mathcal{F}^{-1}[\underline{\rho_e}] = \rho_e$), we can re-write Equation 4.7 explicitly:

$$\begin{aligned} \tilde{\mathbf{f}}_{ET} &= \sum_n \left(\frac{\sigma_m \nabla \varepsilon_m - \varepsilon_m \nabla \sigma_m}{\sigma_m + i\omega_n \varepsilon_m} \cdot \tilde{\mathbb{E}}_n \exp(i\omega_n t) \right) \sum_k \tilde{\mathbb{E}}_k \exp(i\omega_k t) \\ &\quad -\frac{1}{2} \sum_n \tilde{\mathbb{E}}_n \exp(i\omega_n t) \sum_k \tilde{\mathbb{E}}_k \exp(i\omega_k t) \nabla \varepsilon_m \end{aligned} \tag{4.12}$$

Taking the time average and invoking orthogonality (only terms where n = k are non-zero when averaged over time), we find:

$$\begin{aligned} \langle \mathbf{f}_{ET} \rangle &= \frac{1}{2} \Re \left[\sum_n \left(\frac{\sigma_m \nabla \varepsilon_m - \varepsilon_m \nabla \sigma_m}{\sigma_m + i\omega_n \varepsilon_m} \cdot \tilde{\mathbb{E}}_n \right) \tilde{\mathbb{E}}_n \right] \\ &\quad -\frac{1}{4} \Re \left[\tilde{\mathbb{E}}_n \cdot \tilde{\mathbb{E}}_n \right] \nabla \varepsilon_m \end{aligned} \tag{4.13}$$

Equation 4.13 shows that the real, time-average electrothermal force obeys superposition.

4.3.3 Thermodynamics

In this section, we examine several thermodynamic contributions: (i) the conduction of heat through the fluid and channel boundaries, (ii) the convection of heat through the

channel, and (iii) the effect of temperature dependent solid, fluid, and electrical material properties.

Temperature-dependent Parameters

In this work, we consider temperature-dependent viscosity (η), thermal conductivity (k_m), specific heat (C_p), electrical conductivity (σ_m), and permittivity (ε_m). The ionic solutions considered in this work are of low concentration such that mechanical parameters (η, k_m, and C_p) are approximately independent of concentration. Electrical conductivity of electrolytes increases $2.2\%/^{\circ}\text{K}$ [48]. Viscosity, thermal conductivity, specific heat, and electrical permittivity are modeled using polynomial fits of data taken from [49] between 273 °K and 373 °K with coefficient values listed in Table 4.1:

Table 4.1: Coefficient values used to model the temperature dependence of the fluid media's viscosity, η (a_n coefficients, Equation 4.14), thermal conductivity, k_m (b_n coefficients, Equation 4.15), specific heat at constant pressure, C_p (c_n coefficients, Equation 4.16), and electrical permittivity, ε_m (d_n coefficients, Equation 4.17).

Coefficient	Value	Coefficient	Value
a_0	1.379957	c_0	1.201×10^{4}
a_1	-2.122402×10^{-2}	c_1	-80.407
a_2	1.360456×10^{-4}	c_2	0.30987
a_3	-4.645409×10^{-7}	c_3	-5.3819×10^{-4}
a_4	8.904274×10^{-10}	c_4	3.6254×10^{-7}
a_5	$-9.079069 \times 10^{-13}$		
a_6	3.845733×10^{-16}		
b_0	-8.69×10^{-1}	d_0	251.1
b_1	8.948×10^{-3}	d_1	-0.7992
b_2	-1.5836×10^{-5}	d_2	7.375×10^{-4}
b_3	7.9754×10^{-9}		

$$\eta = a_0 + a_1 T + a_2 T^2 + a_3 T^3 + a_4 T^4 + a_5 T^5 + a_6 T^6 \tag{4.14}$$

$$k_m = b_0 + b_1 T + b_2 T^2 + b_3 T^3 \tag{4.15}$$

$$C_p = c_0 + c_1 T + c_2 T^2 + c_3 T^3 + c_4 T^4 \tag{4.16}$$

$$\varepsilon_m = d_0 + d_1 T + d_2 T^2 \tag{4.17}$$

Joule Heating

Localized Joule heating near a channel constriction is a source of temperature gradients that lead to spatial variations in material properties and associated electrothermal flow phenomena. Joule heating corresponds to the electrical energy generated per unit volume:

$$q = \mathbf{J} \cdot \mathbf{E} = \sigma_m \mathbf{E} \cdot \mathbf{E} \tag{4.18}$$

where $\mathbf{J}$ is the electric current. The energy generated by Joule heating depends on the temperature distribution via σ_m.

Heat Conduction and Convection

Heat is transferred through the system by convection and conduction. Heat generated by Joule heating is dissipated through the fluid and substrate by conduction and transported downstream by convection according to Equation 4.19 [50]:

$$\rho_m C_p \frac{\partial T}{\partial t} + \rho_m C_p \mathbf{u} \cdot \nabla T = k_m \nabla^2 T + \sigma_m \mathbf{E} \cdot \mathbf{E} \tag{4.19}$$

where we have neglected viscous dissipation and the temperature (T) and electric field

are time-averaged. The thermal Péclet number, which compares magnitude of heat convection to heat diffusion,

$$\frac{|\rho_m C_p \mathbf{u} \cdot \nabla T|}{|k_m \nabla^2 T|} \approx \frac{\rho_m C_p u l}{k_m} \equiv Pe_T \tag{4.20}$$

is of order 1 in this work owing to the thermally insulating nature of the surrounding plastic substrate, large fluid speeds, and large temperature gradients in the constriction region. Therefore, in this work, we choose to retain the convective term. We examine only stationary, time-averaged solutions, so we neglect the first term on the left-hand side of Equation 4.19, resulting in

$$\rho_m C_p \mathbf{u} \cdot \nabla T = k_m \nabla^2 T + \sigma_m \mathbf{E} \cdot \mathbf{E} \tag{4.21}$$

In addition to heat conduction and convection within the fluid domain, we model conductive heat transfer through the channel walls and into the air surrounding the device. To do this, we consider a 100-μm-deep channel embedded between two 1-mm-thick Zeonor (plastic) substrates. This defines five regions in a two-dimensional model: air (above and below), Zeonor substrate (above and below), and the channel. There are four distinct interfaces to consider, of two types: air/Zeonor and Zeonor/water. These four interfaces correspond to a device placed on an inverted microscope stage, where free convection occurs on top and bottom of the device. We treat the air/Zeonor interfaces by extracting a heat transfer coefficient from empirically determined Rayleigh (Ra) and average Nusselt ($\overline{\mathrm{Nu}}_\ell$) numbers [50].

$$\overline{\mathrm{Nu}}_\ell = 0.54 \mathrm{Ra}_\ell^{1/4} \tag{4.22}$$

$$
\begin{aligned}
&= \frac{h_{\mathrm{a/Z}}\ell}{k_{\mathrm{a}}} \\
&\approx \frac{1}{2}\sqrt[4]{\frac{g\beta_{\mathrm{a}}a\ell^3}{\alpha_{\mathrm{a}}\nu_{\mathrm{a}}}(T_{\mathrm{a,Z}}-T_0)}
\end{aligned} \tag{4.23}
$$

where ℓ is the ratio of device area to perimeter, $k_{\mathrm{a}} = 0.028\mathrm{W/m^{\circ}K}$ is the thermal conductivity of air, $h_{\mathrm{a/Z}}$ is the heat transfer coefficient for the air/Zeonor interface, T_0 is the room or reservoir temperature (far from the interface), and $g\beta_{\mathrm{a}}/\alpha_{\mathrm{a}}\nu_{\mathrm{a}}$ is a ratio of thermal convection and conduction constants. g is acceleration due to gravity, β_{a} is the thermal expansion coefficient of air, α_{a} is the thermal diffusivity of air, and ν_{a} is the kinematic viscosity of air. The lower interface is characterized by a slightly different relationship [50]:

$$
\overline{\mathrm{Nu}}_{\ell} \approx \frac{1}{4}\mathrm{Ra}_{\ell}^{1/4} \tag{4.24}
$$

For the purposes of estimation, we assume that the heat transfer occurs in one dimension, and we balance the heat flux across both air/Zeonor and Zeonor/water interfaces:

$$
\begin{aligned}
q_{\mathrm{a,Z}} &= h_{\mathrm{a,Z}}(T_{\mathrm{a,Z}}-T_0) && (4.25)\\
&= \frac{k_{\mathrm{Z}}}{\ell}(T_{\mathrm{Z,w}}-T_{\mathrm{a,Z}}) = q_{\mathrm{Z,w}} && (4.26)
\end{aligned}
$$

where $T_{\mathrm{a,Z}}$ and $T_{\mathrm{Z,w}}$ are the temperatures at the air/Zeonor and Zeonor/water interfaces, respectively, and $k_{\mathrm{Z}} = 0.147\mathrm{W/m^{\circ}K}$ is the thermal conductivity of Zeonor [51]. Solving for the linearized heat transfer coefficient across the air/Zenor interface, we obtain:

$$
\text{Upper} \quad : \quad h_{\mathrm{a,Z}} \approx \frac{k_{\mathrm{a}}l}{2k_{\mathrm{Z}}\ell}\sqrt[4]{\frac{g\beta_{\mathrm{a}}\ell^3}{\alpha_{\mathrm{a}}\nu_{\mathrm{a}}}(T_{\mathrm{a,Z}}-T_0)} \tag{4.27}
$$

$$\text{Lower} \quad : \quad h_{a,Z} \approx \frac{k_a l}{4 k_Z \ell} \sqrt[4]{\frac{g \beta_a \ell^3}{\alpha_a \nu_a} (T_{a,Z} - T_0)} \tag{4.28}$$

These expressions give boundary conditions for the upper and lower air/Zeonor interfaces. In addition, to eliminate the substrate material from the computational domain and reduce computation time, we define a linearized thermal conductivity term that is determined by fitting

$$(T_{Z,w} - T_{a,Z})^4 = \frac{g \beta_a \ell^3}{32 \alpha_a \nu_a} \left(\frac{l k_a}{\ell k_Z} \right)^4 (T_{a,Z} - T_0) \tag{4.29}$$

where $l = 1$mm is the thickness of the Zeonor substrate and is a result of linearizing heat transfer through the substrate. Plotting $T_{a,Z}$ vs $T_{Z,w}$ and fitting to a linear function at the top and bottom interfaces and averaging the results we obtain:

$$\overline{q_{Z,w}} = \frac{k_Z}{l} \xi (T_{Z,w} - T_0) \tag{4.30}$$

where $\xi = 0.1286$ with $R^2 = 0.9$. Using Equations 4.27 and 4.28, we simulate the channel and the Zeonor substrate to assess the error introduced by our linearization and averaging. In these simulations, the applied voltage was swept from 1V to 250V in a quiescent fluid. Results (not shown) show less than 2% error.

4.3.4 Particle Electrokinetics

Electrophoresis

Electrophoresis drives particle motion in the direction of the local electric field. For particles whose radius is significantly greater than the thickness of their double layer

($\lambda_D \ll a$), particle electrophoretic velocity can be described by a Smoluchowski equation:

$$\mathbf{u}_{EP} = \frac{\varepsilon_m \zeta_p}{\eta}\mathbf{E} \tag{4.31}$$

where ζ_p is a phenomenological potential that defines the no-slip boundary condition within the particle double layer.

Dielectrophoresis

Dielectrophoresis results from the Coulomb force on bound charge at the interface between fluid and particle (mathematically, resulting from a discontinuity in complex permittivity). Given a homogeneous, isotropic, spherical particle in a homogeneous, infinite medium, the time-averaged DEP force can be written as [2]

$$\langle \mathbf{f}_{DEP} \rangle = \pi a^3 \varepsilon_m \Re[\tilde{f}_{CM}] \nabla(\mathbf{E}\cdot\mathbf{E}) \tag{4.32}$$

$$\tilde{f}_{CM} = \frac{\tilde{\varepsilon}_p - \tilde{\varepsilon}'_m}{\tilde{\varepsilon}_p + 2\tilde{\varepsilon}'_m} \tag{4.33}$$

where $\tilde{\varepsilon} = \varepsilon - i\sigma/\omega$ and $\tilde{f}_{CM}$ is the complex Clausius-Mossotti factor and contains the frequency dependence of the DEP force. In the limit as $\omega \to 0$, $\tilde{f}_{CM}$ can be expressed using purely real, conductive components of $\tilde{\varepsilon}$. It has been shown that the DEP force obeys superposition for electric fields with multiple frequencies [52, 19]:

$$\langle \mathbf{f}_{DEP} \rangle = \pi a^3 \varepsilon_m \sum_{\mathrm{n}} \Re[\tilde{f}_{CM,\mathrm{n}}] \nabla(\mathbf{E}_\mathrm{n}\cdot\mathbf{E}_\mathrm{n}) \tag{4.34}$$

where $\tilde{f}_{CM,\mathrm{n}}$ is the complex Clausius-Mossotti factor at frequency ω_{n}.

4.3.5 Summary of Governing Equations and Boundary Conditions used in Numerical Simulations

We now simplify the general analytical expressions presented above to those solved numerically in our simulations. In our numerical work, we consider a DC-offset, AC electric field defined by:

$$\mathbf{E} = \mathbf{E}_{AC} + \mathbf{E}_{DC} = (\alpha + 1)\mathbf{E}_{DC} \tag{4.35}$$

and write the governing equations in terms of the DC field ($\mathbf{E}_{DC}$) and the scaling parameter, α, that relates the peak magnitude of the AC field to the magnitude of the DC field. The following steady-state governing equations were used in our simulations:

- **Electric Field** The equation for charge continuity was solved to determine the electric field.

$$\nabla \cdot (\sigma_m \mathbf{E}_{DC}) = 0 \tag{4.36}$$

  Electromagnetic boundary conditions are defined by specifying the potential at the channel inlet and outlet and specifying zero normal current at insulating channel walls.

$$\text{Inlet} \quad : \quad \phi = V_{\text{applied}} \tag{4.37}$$

$$\text{Outlet} \quad : \quad \phi = 0 \tag{4.38}$$

$$\text{Walls} \quad : \quad \hat{\mathbf{n}} \cdot (\sigma_m \mathbf{E}_{DC}) = 0 \tag{4.39}$$

where $\hat{\mathbf{n}}$ is an outward-facing normal unit vector and V_{applied} is the magnitude of the DC component of the electric potential at the inlet.

- **Fluid Velocity Field** Equation 4.13 is simplified by setting $\omega_0 = 0$ and $\omega_1 = \omega$. The incompressible Navier-Stokes equations with an electrothermal body force term and the continuity equation are solved to determine the fluid velocity field.

$$\rho_m(\mathbf{u} \cdot \nabla)\mathbf{u} = -\nabla p + \eta \nabla^2 \mathbf{u} + \langle \mathbf{f}_{ET} \rangle \tag{4.40}$$

$$\langle \mathbf{f}_{ET} \rangle = \frac{1}{2}\Re\left[\left(\left[(\sigma_m \nabla \varepsilon_m - \varepsilon_m \nabla \sigma_m)\left(\frac{\alpha^2}{\sigma_m + i\omega\varepsilon_m} + \frac{2}{\sigma_m}\right)\right] \cdot \mathbf{E}_{DC}\right)\mathbf{E}_{DC}\right] - \frac{\alpha^2 + 2}{4}\Re\left[\mathbf{E}_{DC} \cdot \mathbf{E}_{DC}\right]\nabla \varepsilon_m \tag{4.41}$$

$$\nabla \cdot \mathbf{u} = 0 \tag{4.42}$$

The hydrodynamic boundary conditions applied in our numerical simulations are zero viscous stress at the inlet and outlet with no applied pressure gradient and an electroosmotic slip boundary condition at the channel walls.

$$\text{Inlet} \quad : \quad \partial \mathbf{u}/\partial \mathbf{n} = 0, p = 0 \tag{4.43}$$

$$\text{Outlet} \quad : \quad \partial \mathbf{u}/\partial \mathbf{n} = 0, p = 0 \tag{4.44}$$

$$\text{Walls} \quad : \quad \mathbf{u} = -\frac{\varepsilon_m \zeta_w}{\eta}\mathbf{E} \tag{4.45}$$

- **Temperature Field** The energy conservation and Joule heating equations are solved to determine the temperature field.

$$\rho_m C_p \mathbf{u} \cdot \nabla T = k_m \nabla^2 T + q \tag{4.46}$$

$$q = \frac{\alpha^2 + 2}{2} \sigma_m \mathbf{E} \cdot \mathbf{E} \tag{4.47}$$

Thermal boundary conditions are based on a 1mm-thick Zeonor (plastic) wall. The inlet boundary condition is a fixed temperature, assuming that the fluid in the reservoir equilibrates to room temperature. At the outlet, heat transfer is allowed via convective flux. This assumes that the outlet reservoir is far from the constriction. Testing reveals that this boundary condition incurs less than 2% error, comparing favorably with setting a fixed temperature condition as done in [53]. Heat transfer through the channel walls is described above in §4.3.3 and results in a linearized boundary condition for the channel wall.

$$\text{Inlet} \quad : \quad T = 293 \tag{4.48}$$

$$\text{Outlet} \quad : \quad q = \rho_m C_p \mathbf{u} \cdot \nabla T \tag{4.49}$$

$$\text{Walls} \quad : \quad q = -\frac{k_Z}{l} \xi (T - T_0), T_0 = 293 \tag{4.50}$$

- **Particle Velocity Field** Electrophoretic and dielectrophoretic force fields are determined from the electric field

$$\mathbf{u}_{EP} = \frac{\varepsilon_m \zeta_p}{\eta} \mathbf{E} \tag{4.51}$$

$$\mathbf{u}_{DEP} = \frac{\varepsilon_m a^2}{6\eta} \left(\alpha^2 \Re[\tilde{f}_{CM}(\omega)] + 2\Re[\tilde{f}_{CM}(0)] \right) \nabla \mathbf{E}_{DC}^2 \tag{4.52}$$

4.4 Methods

Numerical simulations of the fully coupled system were performed using COMSOL multiphysics modeling software. A representative system was developed and tested in COMSOL and then scripted for parametric studies of geometry (r), AC-to-DC ratio (α), particle zeta potential (ζ_p), wall zeta potential (ζ_w), and conductivity (σ_m) in MATLAB.

4.4.1 Particle Deflection and Trapping

Particle deflection and trapping are two metrics used in this work to evaluate the impact of electrothermal flow on iDEP devices. Dielectrophoretic deflection refers to the movement of particles transverse to the direction of flow owing to a negative DEP (nDEP) force ($f_{CM} < 0$) pointing away from the corners of the constriction (localized peaks in the electric field magnitude). Consider a particle entering the channel in the middle (i.e., $y = 50\mu$m in a 100μm-wide channel, Figure 4.1): in the absence of electrothermal and DEP forces, this particle will pass the constriction and exit the channel at the same location. nDEP forces deflect the particle from this pathline, causing the particle to be displaced away from the constriction edge and exit at a different location (e.g., $y = 75\mu$m). Particle deflection and deflection difference in the presence of an electrothermal body force are defined in Figure 4.2. We calculated particle pathlines by balancing Equation 4.34 against Stokes' drag ($\mathbf{u}_{DEP} = \mathbf{f}_{DEP}/6\pi\eta a$) for a 1$\mu$m diameter particle:

$$\begin{aligned} \mathbf{u}_{\text{particle}} &= \mathbf{u}_{EP} + \mathbf{u}_{DEP} + \mathbf{u} \\ &= \frac{\varepsilon_m \zeta_p}{\eta}\mathbf{E} + \frac{\varepsilon_m a^2}{6\eta}\left(\alpha^2 \Re[\tilde{f}_{CM}(\omega)] + 2\Re[\tilde{f}_{CM}(0)]\right)\nabla \mathbf{E}_{DC}^2 + \mathbf{u} \end{aligned} \quad (4.53)$$

where **u** is the fluid velocity due to electroosmosis and electrothermal flow. For the purposes of comparison and to isolate the effects of electrothermal flow, the Clausius-Mossotti factor was -0.5 in all simulations, with no frequency dependence. Deflection was calculated by subtracting the inlet position of the middle particle pathline from its outlet position. In cases where the particle did not exit the channel, no data is reported.

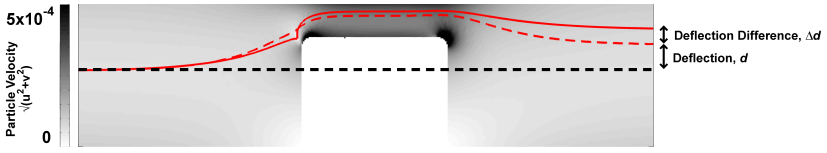

Figure 4.2: Particle deflection, d, and deflection difference, Δd, are two metrics used to quantify electrothermal effects in this work. Particle pathlines (red, color online) include the effects of electrophoresis, DEP, and fluid flow on particle motion with (solid) and without (dashed) an electrothermal body force term in the Navier-Stokes equations. The background color table corresponds to particle velocity magnitude ($|\mathbf{u}|$) in the baseline case, without electrothermal flow. Simulation parameters are those listed in Table 4.2 with $\alpha = 38$.

Dielectrophoretic trapping in insulating systems occurs when nDEP forces overcome linear electrokinetic and fluid drag forces, preventing particles from passing the constriction region. We consider a particle entering the channel in the middle (i.e., $y = 50\mu$m in a 100μm-wide channel) and calculate its path due to the combined effects of electrophoresis, DEP, and fluid drag (combined electroosmotic and electrothermal flow)(Equation 4.53). If the final (stagnation) position of the particle is not past the constriction, then the particle is considered "trapped". We quantify this phenomenon by recording the value of α where trapping first occurs, $\alpha_{trapping}$.

4.5 Results and Discussion

We conducted several sets of simulations with variations from a baseline case. The datum case parameters are listed in Table 4.2. We investigate how changes in channel

geometry (r), fluid conductivity (σ_m), particle zeta potential (ζ_p), channel wall zeta potential (ζ_w), and the DC electric potential magnitude (V_{DC}), affect particle transport. Values are listed in Table 4.3. The channel geometry parameter, r, is the constriction ratio, defined as the bulk channel depth divided by the constriction depth (e.g., a 100μm-wide channel that is constricted to 25μm-wide would have a constriction ratio $r = 4$). For all cases, the AC-to-DC ratio, α, was varied from 0 to 50. Each case was also investigated with and without the electrothermal body force term (Equation 4.13).

Table 4.2: Datum case for numerical simulations of electrothermal flow.

σ_m (S/m)	$-\zeta_w$ (mV)	$-\zeta_p$ (mV)	r	V_{DC} (V)
0.01	40	60	4	10

Table 4.3: Simulation parameter sets for numerical simulations of electrothermal flow. Each set isolates a particular variable from the datum state.

Simulation Set	Variable (units)	Values
S1	r (unitless)	1.3, 1.7, 2.9, 3.3, 4, 5, 6.7, 10, 20
S2	σ_m (S/m)	5×10^{-2}, 1×10^{-2}, 5×10^{-3}, 1×10^{-3}, 5×10^{-4}, 1×10^{-4}, 5×10^{-5}, 1×10^{-5}, 5×10^{-6}, 1×10^{-6}
S3	$-\zeta_w$ (mV)	1, 5, 10, 20, 30, 40, 50, 60, 70, 80, 90, 100
S4	$-\zeta_p$ (mV)	0.01, 0.1, 1, 10, 20, 30, 40, 50, 60, 70, 80, 90, 100
S5	V_{DC} (V)	1, 5, 10, 15, 25, 50, 75, 100

4.5.1 Electrothermal Flow

The electrothermal body force acts opposite the direction of flow on the upstream side of the constriction, decreasing — and eventually reversing — fluid velocity as the force magnitude increases. The body force depends on gradients in fluid conductivity and permittivity. These gradients are temperature-driven in this system and so the electrothermal body force is directed down gradients in fluid temperature. In the iDEP constriction

geometry, the temperature is highest in the constriction region and lowest at the channel entrance and the resulting electrothermal body force is therefore directed away from the constriction, as shown in Figure 4.3.

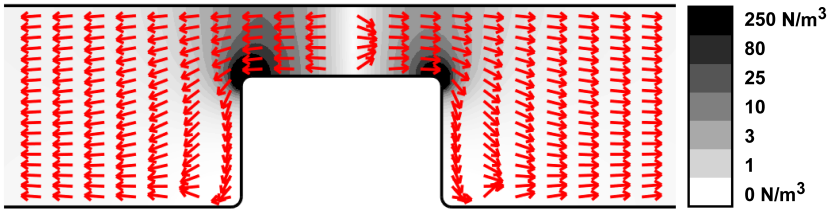

Figure 4.3: The electrothermal body force is directed down gradients in fluid electrical parameters, i.e. down gradients in temperature. Arrows (red, color online) show the direction of the electrothermal force (Equation 4.13). Filled contours correspond to the magnitude of the electrothermal force and are logarithmic. The highest contour groups all electrothermal force magnitude values above 250N/m^3 for clarity (maximum, $1,865$N/m^3). Simulation parameters are those listed in Table 4.2 with $\alpha = 40$ and include the electrothermal body force term in the Navier-Stokes equations.

As α increases, the magnitude of the electrothermal body force increases and perturbs the electroosmotic flow field. Figures 4.4(a) and 4.4(b) show how the flow field changes as α (and the electrothermal body force) increases at two different locations near the constriction region: $x = 4.75$mm and $x = 4.9$mm. These figures highlight three key phenomena: (i) as α increases the fluid velocity in the center of the channel ($y = 50\mu$m) decreases and reverses direction for $\alpha \gtrsim 35$, (ii) as α increases the fluid velocity near the channel wall increases because the electroosmotic mobility increases as a function of temperature (η decreases more rapidly than ε_m in Equation 4.6), and (iii) the fluid velocity distribution becomes skewed near the constriction because of locally fast electroosmosis in the constriction region, driven by higher electric fields and higher electroosmotic mobility (μ_{EO}).

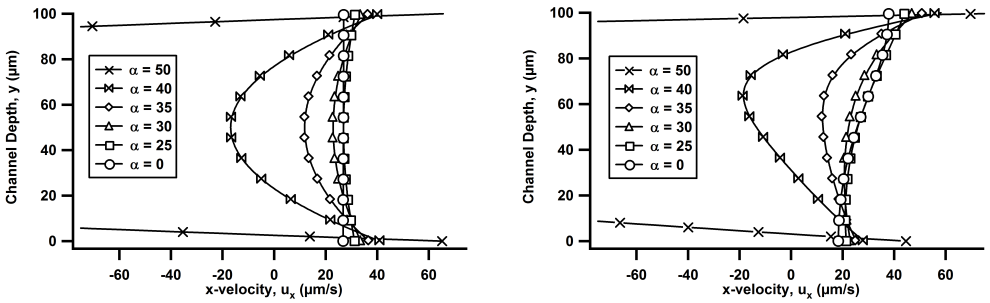

Figure 4.4: Profiles of fluid velocity in the x-direction plotted against channel height (y, Figure 4.1) at select values of α. Velocity profiles are calculated at $x = 4.75$mm in 4.4(a) and $x = 4.9$mm in 4.4(b). The upper portion of the fluid velocity profile is skewed closer to the constriction as a result of the increase in the electroosmotic flow velocity. Simulation parameters are listed in Table 4.2.

4.5.2 Temperature

Channel temperature is of critical importance for experiments involving cellular samples. We choose to analyze the mean temperature in the constriction region, $\overline{T}_c$, because it represents the highest temperature region within the channel and it is the most sensitive to electrothermal effects. The results of simulations with varying constriction ratio (r), solution conductivity (σ_m), wall zeta potential (ζ_w), and DC-field magnitude (V_{DC}) are reported in Figure 4.5. Also reported is the percent difference in $\overline{T}_c$ due to electrothermal flow.

The mean constriction temperature decreases with increasing constriction ratio and wall zeta potential. This is indicative of increased heat convection out of the constriction region. As the constriction ratio increases, the electric field within the constriction region increases and the electroosmotic flow velocity increases. This increase in heat convection competes with additional Joule heating in the constriction region, leading to a weak decrease in $\overline{T}_c$ as a function of constriction ratio. Similarly, changes in ζ_w change the electroosmotic flow velocity. In both cases, changing r or ζ_w, convection

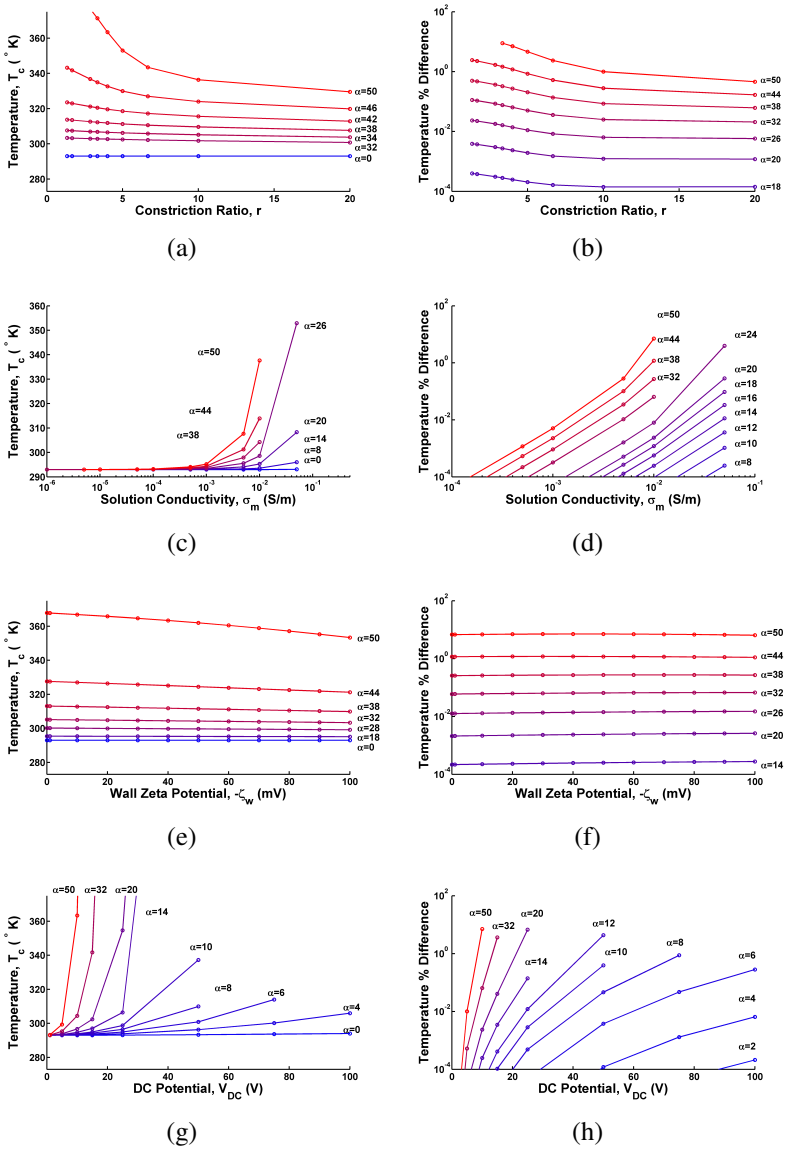

Figure 4.5: The mean constriction temperature (region defined in Figure 4.1) is plotted for the datum state (Table 4.2, including the electrothermal body force term) with variations in r, σ_m, ζ_w, and V_{DC} in the left-hand column (Figures 4.5(a), 4.5(c), 4.5(e), and 4.5(g)). The percentage difference in $\overline{T}_c$ between solutions with and without an electrothermal body force term are plotted in the right-hand column (Figures 4.5(b), 4.5(d), 4.5(f), 4.5(h)).

transports heat generated within the constriction region downstream, into the bulk of the channel. The result of increased convection due to increasing r ro ζ_w is a decrease in $\overline{T}_c$. The influence of electrothermal flow decreases with increasing r. The increased

electroosmotic fluid velocity within the constriction region dominates the contributions from the electrothermal body force, which act opposite the direction of electroosmosis on the leading side of the constriction. The effects of electrothermal flow on $\overline{T}_c$ were found to be independent of ζ_w over the range of test values.

$\overline{T}_c$ increases with increasing solution conductivity, σ_m, and DC field magnitude, V_{DC}. These results are indicative of increased Joule heating (Equation 4.18) in the constriction region. Electrothermal effects on $\overline{T}_c$ also increase with increasing σ_m and V_{DC}, owing to increased localized heat generation within the constriction region, which drives gradients in fluid conductivity and permittivity.

4.5.3 Particle Deflection and Trapping

Particle deflection and trapping are the two primary modes of operation for 2D and 3D iDEP techniques, respectively [19, 20, 37, 38, 54, 39, 55]. Electrothermal effects, in certain regimes, significantly enhance these phenomena by decreasing the local fluid velocity and increasing particle residence time. The particle deflection and trapping results for simulations with varying constriction ratio (r), solution conductivity (σ_m), particle zeta potential (ζ_p), channel wall zeta potential (ζ_w), and DC electric field magnitude (V_{DC}) are shown in Figure 4.6. These results quantify particle deflection as a function of these parameters with varying AC-to-DC ratio, α, in the presence of electrothermal flow, the percent difference between simulation results with and without the electrothermal body force term in Equation 4.4, and the threshold value of α for particle trapping, α_{trapping}.

Figure 4.6: Particle trajectory analysis data for the datum state (Table 4.2) with variations in r (4.7(a),4.7(b), 4.7(c)), σ_m (4.7(d), 4.7(e), 4.7(f)), ζ_p (4.7(g), 4.7(h), 4.7(i)), ζ_w (4.7(j), 4.7(k), 4.7(l)), and V_{DC} (4.7(m), 4.7(n), 4.7(o)). Particle deflection with the electrothermal body force is plotted in the left-hand column in Figures 4.7(a), 4.7(d), 4.7(g), 4.7(j), and 4.7(m). Percentage difference in particle deflection between simulations with and without the electrothermal body force term is plotted in the center column in Figures 4.7(b), 4.7(e), 4.7(h), 4.7(k), and 4.7(n). Finally, α_{trapping} is plotted in the right-hand column in Figures 4.7(c), 4.7(f), 4.7(i),. 4.7(l), and 4.7(o). In left and center columns, line color (online) corresponds to α, varying from 0 (blue) to 50 (red) and increasing upward. In the right column, the line color (online) corresponds to data with (solid red, lower) and without (dashed blue, upper) electrothermal flow.

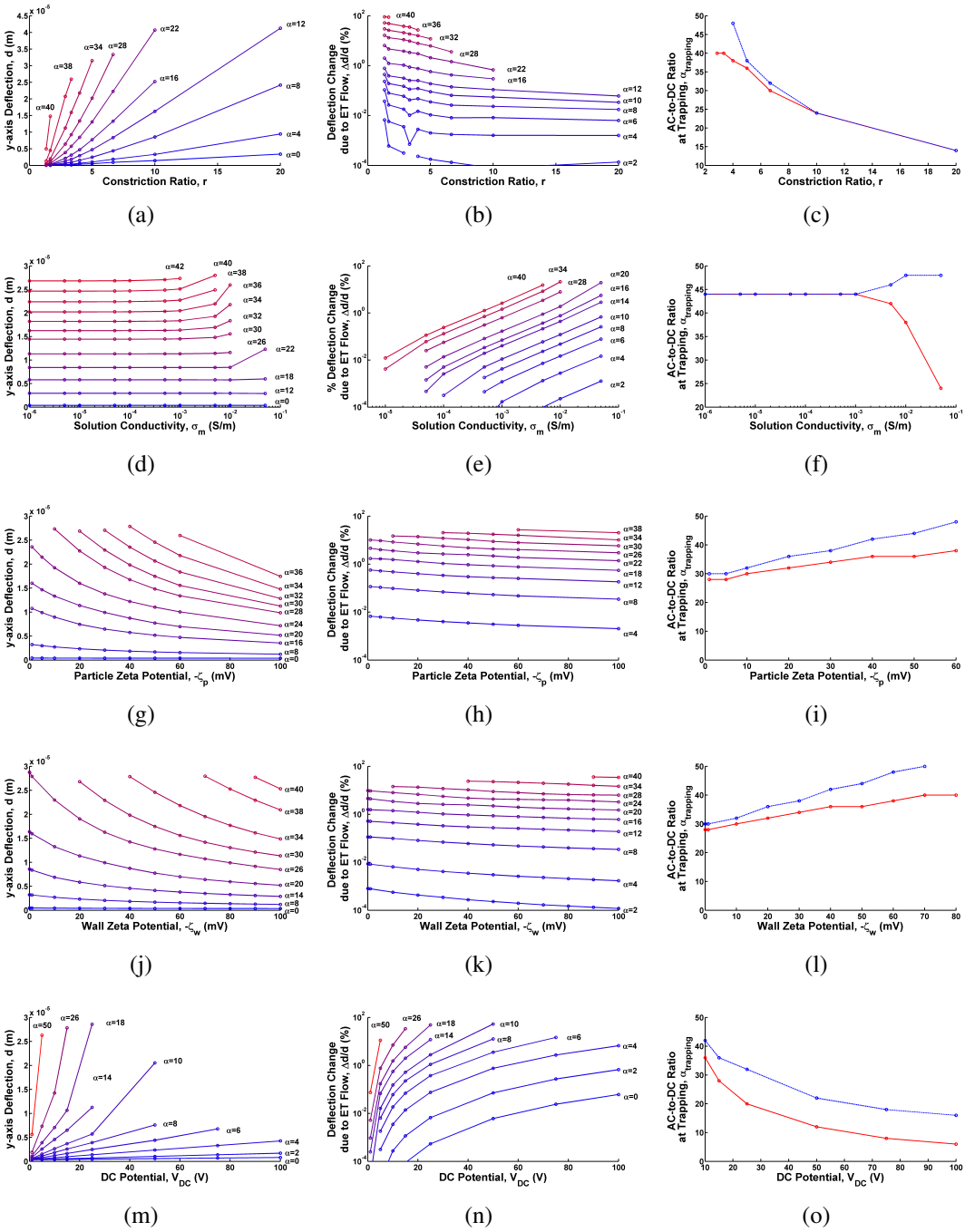
y-axis Deflection, d (m)
Constriction Ratio, r
(a)
Deflection Change due to ET Flow, Δd/d (%)
Constriction Ratio, r
(b)
AC-to-DC Ratio at Trapping, α_trapping
Constriction Ratio, r
(c)
y-axis Deflection, d (m)
Solution Conductivity, σ_m (S/m)
(d)
% Deflection Change due to ET Flow, Δd/d (%)
Solution Conductivity, σ_m (S/m)
(e)
AC-to-DC Ratio at Trapping, α_trapping
Solution Conductivity, σ_m (S/m)
(f)
y-axis Deflection, d (m)
Particle Zeta Potential, -ζ_p (mV)
(g)
Deflection Change due to ET Flow, Δd/d (%)
Particle Zeta Potential, -ζ_p (mV)
(h)
AC-to-DC Ratio at Trapping, α_trapping
Particle Zeta Potential, -ζ_p (mV)
(i)
y-axis Deflection, d (m)
Wall Zeta Potential, -ζ_w (mV)
(j)
Deflection Change due to ET Flow, Δd/d (%)
Wall Zeta Potential, -ζ_w (mV)
(k)
AC-to-DC Ratio at Trapping, α_trapping
Wall Zeta Potential, -ζ_w (mV)
(l)
y-axis Deflection, d (m)
DC Potential, V_DC (V)
(m)
Deflection Change due to ET Flow, Δd/d (%)
DC Potential, V_DC (V)
(n)
AC-to-DC Ratio at Trapping, α_trapping
DC Potential, V_DC (V)
(o)

Particle deflection is a strong function of constriction ratio and can be affected by electrothermal flow. As the constriction ratio increases, the depth in the constriction region decreases and the electric field increases in order to satisfy conservation of current. This results in increasing electric field gradients and DEP forces. A particle approaching the constriction will be increasingly forced away from the constriction corners by nDEP as the constriction ratio increases (Figure 4.7(a)). The effects of electrothermal flow decrease with increasing constriction ratio and become significant only at higher values of α (Figure 4.7(b)). As discussed above in §4.5.2 in the context of the mean constriction temperature, $\overline{T}_c$, the magnitude of the electroosmotic boundary condition within the constriction region increases with the constriction ratio and dominates the electrothermal body force on the fluid as a result. This can be seen in Figures 4.7(p) and 4.7(q), in which recirculating flow is suppressed as the constriction ratio increases. Consistent with the results for particle deflection, the value of α_{trapping} is a strong function of the constriction ratio and is affected by electrothermal flow at low constriction ratios, $r < 6$ (Figure 4.7(c)). Beyond $r = 6$, the flow velocity within the constriction region obscures the effects of the electrothermal body force.

Solution conductivity, σ_m, has a significant impact on $\overline{T}_c$, but does not significantly impact particle deflection (Figure 4.7(d)). Rather, σ_m influences the magnitude of electrothermal flow and thereby indirectly affects particle deflection. This can be seen in Figures 4.7(d) and 4.7(e) where particle deflection is independent of solution conductivity below 1×10^{-3}S/m. The variations observed at high conductivities and high α are the result of increasing electrothermal effects. Electrothermal effects increase significantly with increasing σ_m, especially where $\sigma_m \gtrsim 1 \times 10^{-3}$S/m and $\alpha \gtrsim 25$ (Figure 4.7(e)). Based on deflection data shown in Figure 4.7(d), α_{trapping} is expected to be independent of σ_m at low conductivities and to decrease at higher conductivities. In these cases, at values of σ_m above $\sim 1 \times 10^{-3}$, electrothermal flow decreases α_{trapping} (Figure

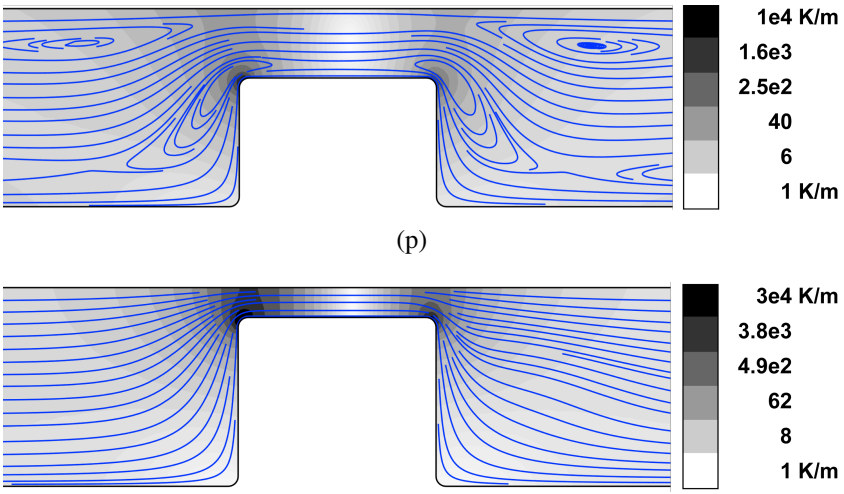

Figure 4.7: Fluid streamlines (blue, color online) at different constriction ratios show that recirculation is suppressed at higher constriction ratios, a result of higher electroosmotic flow boundary conditions within the constriction region. Simulation parameters are identical and listed in Table 4.2 with $\alpha = 40$ and $r = 2.86$ in 4.7(p) and $r = 6.67$ in 4.7(q). Filled contours correspond to temperature gradient magnitude and are logarithmic. The highest contour groups all temperature gradient magnitudes above 1×10^4K/m (top, maximum 3.2×10^4K/m) and 3×10^4K/m (4.7(q)), maximum 4.6×10^4K/m) for clarity. Several streamlines are terminated for clarity.

4.7(f)).

Increasing the magnitude of the particle zeta potential, $|\zeta_p|$, decreases particle deflection and decreases the effects of electrothermal flow. Increasing the particle electrophoretic mobility via increases in $|\zeta_p|$ decreases the relative impact of dielectrophoretic deflection (Figure 4.7(g)). Similarly, the impact of variations in the fluid velocity field owing to the electrothermal body force also decrease with increasing $|\zeta_p|$ (Figure 4.7(h)). For the same reason particle deflection decreases with increasing $|\zeta_p|$, the value of the AC-to-DC ratio necessary to trap particles also increases: electrothermal flow enhances particle trapping by decreasing the fluid velocity transporting particles toward the constriction. This effect, augmented slightly by increasing $|\zeta_p|$, shifts particle pathlines toward regions of slower fluid flow and larger nDEP force (i.e., toward con-

striction corners as shown in Figure 4.2).

Channel wall zeta potential, ζ_w, determines the electroosmotic mobility and the magnitude of the associated slip boundary condition. Increasing $|\zeta_w|$ increases the electroosmotic fluid velocity at the channel boundaries, decreasing particle deflection (Figure 4.7(j)), diminishing the effects of electrothermal flow (Figure 4.7(k)), and increasing α_{trapping} (Figure 4.7(l)). The increasing difference between α_{trapping} in simulations with and without electrothermal flow is attributable to particle pathline distortion from increasing electroosmotic fluid flow, similar to the mechanism described above for particle electrophoresis (ζ_p).

Increasing the DC magnitude of the electric field has a number of effects. Particle electrophoresis and fluid electroosmosis both increase with increasing V_{DC}, as does Joule heating within the channel, leading to increased electrothermal effects. α is scaled by V_{DC}, i.e. the AC field magnitude at $\alpha = 10$ increases as V_{DC} increases. As V_{DC} increases particle deflection increases (Figure 4.7(m)). The electrothermal contribution to particle deflection also increases (Figure 4.7(n)). α_{trapping} decreases with increasing V_{DC} because the ohmic power input is approximately proportional to $(\alpha V_{DC})^2$ and the resulting electrothermal flow (Figure 4.7(o)). As particle electrophoresis and electroosmosis increase $\propto \mathbf{E}$, Joule heating scales $\propto \mathbf{E}^2$, which likely accounts for the decrease in α_{trapping} from electrothermal effects (Figure 4.7(o)).

In this work, we examine particle trajectories as a result of electroosmotic, electrophoretic, and dielectrophoretic phenomena with coupled Joule heating and electrothermal flow effects in polymeric iDEP devices using DC-offset, AC electric fields. We focus on the effects of channel constriction ratio, solution conductivity, and electrokinetic mobilities. Other researchers have studied iDEP particle deflection numerically and experimentally as a technique for size-based separation [39, 37, 38]. The role

of channel geometry has been examined experimentally using an oil drop within the channel to change the constriction ratio [54, 56]. Additional work, utilizing DC-biased, AC electric fields, used an insulating constriction to focus particles using iDEP [20]. Temperature effects were neglected in each of these cases, because the experiments could be run in a low-conductivity buffer. Figures 4.7(d), 4.7(e), and 4.7(f) show that electrothermal effects have the potential to alter the predicted particle trajectories when experiments are run with physiological media where conductivities are in the range of 1S/m.

In contrast to the results presented here, where electrothermal effects generated near an insulating constriction decreased the fluid velocity, other researchers have leveraged electrothermal flows to enhance fluid flow and even pump fluids. Manoochehri et al., utilized asymmetric electrodes strategically placed on channel constrictions to enhance AC electrothermal pumping [24, 34]. Electrode asymmetry creates counter-rotating vortices of different size, resulting in net bulk fluid flow. By placing one of the electrodes on top of a constriction and the other in a groove, the pumping velocity was increased because the counter-flow vortex was displaced away from the bulk fluid. Electrothermal effects have also been used to enhance mixing in microfluidic devices [35, 57].

The key conclusions drawn from our thermal simulations — that channel geometry influences the equilibrium channel temperature and that the temperature distribution within the channel is shifted by heat convection — are consistent with previous studies of electrothermal flow in microfluidic devices. Simulations of Joule heating in microfluidic devices have generally focused on electrode based systems and static fluids [58, 31]. One notable exception is work done by Kates and Ren [53], who numerically studied a diverging microfluidic channel used for isoelectric focusing (IEF). IEF experiments rely on a continuous pH gradient, set up by temperature gradients generated by the applica-

tion of an electric field to a diverging channel. They performed 3D, numerical simulations of a diverging channel and the surrounding substrate with natural heat convection outside the device. Their work examined static and moving fluids and found that heat convection shifted the temperature distribution significantly. Additionally, they found that the channel geometry (the angle of the diverging channel) significantly influenced the channel temperature.

Like the current work, the majority of numerical work examining electrothermal flow near electrodes and particle deflection in iDEP devices is two dimensional. When extending this work to a three dimensional domain, i.e. to ridged structures or constrictions in depth [19], we expect that the results to qualitatively describe fluid and particle behavior perpendicular to such constrictions, provided the constriction is long compared to the depth of the channel. Confounding factors, such as angled constrictions and curved constrictions, can potentially change the local electric and fluid velocity fields. However, if the electric field does not change significantly along the constriction, a two dimensional approximation is justified perpendicular to the constriction, and the local electrothermal body forces remain unchanged. Extensions to three dimensional iDEP devices are not expected to alter the trends identified by this work.

4.6 Concluding Remarks

This work has numerically investigated the effects of electrothermal flow on the mean channel temperature and particle trajectories in a polymeric iDEP device at finite thermal Péclet number as a function of channel geometry (r), electric field parameters (α and V_{DC}), and particle and device properties (ζ_p and ζ_w). These simulations include coupled fluid, electrical, and thermal equations via temperature dependent material properties

such as solution conductivity and permittivity, thermal conductivity, specific heat, and viscosity.

The results show that heat convection contributes to the temperature distribution and temperature gradients responsible for electrothermal flows. The average constriction temperature is a strong function of solution conductivity and electric field magnitude, with weak dependence on the constriction ratio. While convective heat transfer significantly alters the temperature distribution and determines the electrothermal flow field, it can usually be neglected when calculating the mean constriction temperature. $\overline{T}_c$ changes less than 1% due to electrothermal effects except as $\alpha \rightarrow 50$, in which case the error can approach $\sim 10\%$. Particle deflection is a strong function of constriction ratio, as electrothermal effects increase particle deflection more than 10% when the constriction ratio is ≤ 8 and $\alpha \gtrsim 38$. Solution conductivity plays an important role in determining the temperature in the channel and the magnitude of electrothermal effects. As $\sigma_m \geq 1 \times 10^{-2}$ and $\alpha \rightarrow 40$, electrothermal effects make more than a 10% difference in particle deflection. Increasing particle and wall zeta potentials ($|\zeta_p|$, $|\zeta_w|$) decrease particle deflection, but act independent of electrothermal effects, with no appreciable change in electrothermal contributions to particle deflection over the range of ζ_p and ζ_w tested in this work. Varying the DC field magnitude significantly alters particle trajectories and also increases electrothermal effects. The net result of increasing V_{DC} is to increase particle deflection and increase the electrothermal augmentation of deflection. These quantitative results are applicable for a Zeonor microfluidic iDEP device under the datum conditions listed in Table 4.2.

While the quantitative results are specific only to the geometry under study, the trends are clear: $\overline{T}_c$ is a strong function of σ_m and V_{DC}; particle deflection and trapping are strong functions of r and V_{DC}, relatively weak functions of ζ_p and ζ_w, and nearly

independent of σ_m; and electrothermal effects are significant at high electric fields and in solutions of high conductivity. These results are qualitatively consistent with our previous experimental and simulation work [19] and anecdotal explanations for recirculating particle motion in other iDEP devices. Changes in effective solution conductivity can also be induced by particle concentration variations [59, 60] rather than local temperature variations. In this work we assume non-interacting particles at a low volume fraction. The results for particle deflection are unlikely to be affected by particle concentration variations because deflection causes minimal concentration changes. In the case of particle trapping, however, particle volume fraction will increase over time, increasing the effective solution conductivity and further enhancing the effects of fluid forces caused by conductivity inhomogeniety. This accumulation of particles however, only occurs as $\alpha \rightarrow \alpha_{\text{trapping}}$, and so we expect that the results presented here will be applicable across a reasonable range of particle concentrations. In all the cases examined in this work, electrothermal forces (regardless of the source of conductivity variation) point away from the constriction, decreasing the electroosmotic fluid velocity upstream of the constriction and thereby *enhancing* particle deflection and trapping.

4.7 Appendix: Numerical Techniques

4.7.1 COMSOL

Three packages — convection and conduction (heat transfer), conductive media DC (electrostatic), and incompressible Navier-Stokes — were combined to solve for stationary fluid and electrokinetic velocity fields. The convection and conduction package was selected from the COMSOL Multiphysics Heat Transfer toolbox. Conductive media

DC and incompressible Navier-Stokes packages were selected from the MEMS Electrostatics and MEMS Microfluidics toolboxes, respectively. The MEMS toolbox includes boundary conditions that correctly handle simultaneous electoosmotic slip along, and thermal conductivity across, the chanel boundary.

Specific boundary conditions and governing equations are discussed and expressed previously for electromagnetic, thermal, and fluid systems in §4.3.

4.7.2 Geometry Definition

Device geometry was defined and varied parametrically using MATLAB. The geometry consisted of a 1cm-long, 100μm-tall channel with a 100μm-long constriction in the middle. The corners of the constriction were filleted (rounded) with a 5μm radius of curvature. The height of the constriction varied from 25μm to 95μm. We describe the constriction using a "constriction ratio", r, of the bulk channel depth vs the channel depth in the constriction region.

4.7.3 Mesh Resolution and Refinement

Mesh resolution in COMSOL was specified using a free (unstructured) triangular mesh. Maximum element sizes were specified on both the boundary and subdomain. The computational domain was meshed using a $100,000$-element triangular mesh with maximum element resolution specified as 25μm in the domain and 2.5μm on the boundaries. Element density was highest near the boundaries and in the constriction region (Figure 4.1), consistent with the regions of interest in the computational domain.

A series of test simulations, with electrothermal body force, was run over a range of element sizes to qualitatively assess the sensitivity of the solution to mesh resolution. Element size for the unstructured triangular mesh in COMSOL was set by defining the maximum element size on the subdomain and boundaries. The coarsest mesh was defined using a 50μm maximum boundary element size and a 500μm maximum subdomain element size. The simulation was run over this mesh and four subsequent refinements. These simulations contained 1,827, 4,756, 16,566, 63,426, and 250,180 elements, respectively. The relative error was calculated using Equation 4.54 assuming that the finest resolution mesh was correct.

$$\bar{\mathcal{E}}_{\mathrm{n}} = \frac{\sum_p \frac{X_{\mathrm{n}} - X_0}{X_0}}{P} \tag{4.54}$$

where $\bar{\mathcal{E}}_{\mathrm{n}}$ is the average relative error at a resolution of n, X_{n} is the value of a simulation variable (e.g., $\mathbf{u}_x$) at a point p on the coarse, unstructured mesh, P is the total number of grid points, and X_0 is the solution at the same point on the highest resolution mesh. Residuals calculated in this manner for the x and y components of velocity and the fluid temperature were less than 1×10^{-4} and indicate first-order convergence. Verification of the ODE formulation was performed by calculating a 1-D temperature distribution in a stagnant fluid and calculating the Laplace solution for electroosmotic flow in an isothermal case. Numerical results matched the analytical results in both cases.

BIBLIOGRAPHY

[1] Herbert A Pohl. *Dielectrophoresis: The behavior of neutral matter in nonuniform electric fields*. Cambridge University Press, 1978.

[2] Thomas B Jones. *Electromechanics of Particles*. Cambridge University Press, New York, 1995.

[3] Brian J. Kirby. *Micro- and Nanoscale Fluid Mechanics: Transport in Microfluidic Devices*. Cambridge University press, 2010.

[4] Benjamin G. Hawkins, Jason P. Gleghorn, and Brian J. Kirby. *Dielectrophoresis for Particle and Cell Manipulations*, chapter 6, pages 133–182. Artech House, Boston, 2009.

[5] A Sanchis, A P Brown, M Sancho, G Martínez, J L Sebastián, S Muñoz, and J M Miranda. Dielectric characterization of bacterial cells using dielectrophoresis. *Bioelectromagnetics*, 28(5):393–401, 2007.

[6] Blanca H Lapizco-Encinas, Blake a Simmons, Eric B Cummings, and Yolanda Fintschenko. Dielectrophoretic concentration and separation of live and dead bacteria in an array of insulators. *Analytical chemistry*, 76(6):1571–9, March 2004.

[7] Yoon-Kyoung Cho, Suhyeon Kim, Kyusang Lee, Chinsung Park, Jeong-Gun Lee, and Christopher Ko. Bacteria concentration using a membrane type insulator-based dielectrophoresis in a plastic chip. *Electrophoresis*, 30(18):3153–9, 2009.

[8] M Castellarnau, A Errachid, C Madrid, A Juárez, and J Samitier. Dielectrophoresis as a tool to characterize and differentiate isogenic mutants of Escherichia coli. *Biophysical journal*, 91(10):3937–45, November 2006.

[9] Jun Yang, Ying Huang, Xiao-Bo Wang, X.B. Wang, F.F. Becker, and P.R.C. Gascoyne. Dielectric properties of human leukocyte subpopulations determined by electrorotation as a cell separation criterion. *Biophysical journal*, 76(6):3307–3314, 1999.

[10] J Yang. Differential Analysis of Human Leukocytes by Dielectrophoretic Field-Flow-Fractionation. *Biophysical Journal*, 78(5):2680–2689, 2000.

[11] P.R.C. Gascoyne, J. Noshari, F.F. Becker, and R. Pethig. Use of dielectrophoretic collection spectra for characterizing differences between normal and cancerous cells. *IEEE Transactions on Industry Applications*, 30(4):829–834, 1994.

[12] Chandra M Das, Frederick Becker, Suzanne Vernon, Jamileh Noshari, Celine Joyce, and Peter R C Gascoyne. Dielectrophoretic segregation of different human cell types on microscope slides. *Analytical chemistry*, 77(9):2708–19, 2005.

[13] C Chou, J Tegenfeldt, S Chan, O Bakajin, E Cox, N Darnton, R Austin, and T Duke. Electrodeless Dielectrophoresis of Single- and Double-Stranded DNA. *Biophysical Journal*, 83(4):2170–2179, October 2002.

[14] Richard W Clarke, Samuel S White, Dejian Zhou, Liming Ying, and David Klenerman. Trapping of proteins under physiological conditions in a nanopipette. *Angewandte Chemie (International ed. in English)*, 44(24):3747–50, June 2005.

[15] Richard Clarke, Joe Piper, Liming Ying, and David Klenerman. Surface Conductivity of Biological Macromolecules Measured by Nanopipette Dielectrophoresis. *Physical Review Letters*, 98(19):198102–6, May 2007.

[16] Ralph Hölzel, Nils Calander, Zackary Chiragwandi, Magnus Willander, and Frank Bier. Trapping Single Molecules by Dielectrophoresis. *Physical Review Letters*, 95(12):128102–4, September 2005.

[17] Blanca H Lapizco-Encinas, Sandra Ozuna-Chacón, and Marco Rito-Palomares. Protein manipulation with insulator-based dielectrophoresis and direct current electric fields. *Journal of chromatography. A*, 1206(1):45–51, October 2008.

[18] M Hughes, H Morgan, F Rixon, J Burt, and R Pethig. Manipulation of herpes simplex virus type 1 by dielectrophoresis. *Biochimica et Biophysica Acta (BBA) - General Subjects*, 1425(1):119–126, September 1998.

[19] Benjamin G Hawkins, A Ezekiel Smith, Yusef A Syed, and Brian J Kirby. Continuous-flow particle separation by 3D Insulative dielectrophoresis using coherently shaped, dc-biased, ac electric fields. *Analytical chemistry*, 79(19):7291–7300, October 2007.

[20] Junjie Zhu and Xiangchun Xuan. Dielectrophoretic focusing of particles in a microchannel constriction using DC-biased AC flectric fields. *Electrophoresis*, 30(15):2668–75, 2009.

[21] Xiangchun Xuan. Joule heating in electrokinetic flow. *Electrophoresis*, 29(1):33–43, 2008.

[22] Torsten Mueller, Annamaria Gerardino, Thomas Schnelle, Stephen G Shirley, Franco Bordoni, Giovanni De Gasperis, R Leoni, and Guenter Fuhr. Trapping of

micrometre and sub-micrometre particles by high-frequency electric fields and hydrodynamic forces. *Journal of Physics D: Applied Physics*, 29(2):340–349, 1996.

[23] Seungkyung Park, Mehti Koklu, and Ali Beskok. Particle Trapping in High-Conductivity Media with Electrothermally Enhanced Negative Dielectrophoresis. *Analytical chemistry*, 2009.

[24] E. Du and Souran Manoochehri. Enhanced ac electrothermal fluidic pumping in microgrooved channels. *Journal of Applied Physics*, 104(6):064902, 2008.

[25] G. Fuhr, R. Hagedorn, T. Muller, W. Benecke, and B. Wagner. Microfabricated electrohydrodynamic (EHD) pumps for liquids of higher conductivity. *Journal of Microelectromechanical Systems*, 1(3):141–146, 1992.

[26] Jonghyun Oh, Robert Hart, Jorge Capurro, and Hongseok Moses Noh. Comprehensive analysis of particle motion under non-uniform AC electric fields in a microchannel. *Lab on a chip*, 9(1):62–78, 2009.

[27] H Morgan, M P Hughes, and N G Green. Separation of submicron bioparticles by dielectrophoresis. *Biophys. J*, 77:516–525, 1999.

[28] Ling-Sheng Jang, Pao-Hua Huang, and Kung-Chieh Lan. Single-cell trapping utilizing negative dielectrophoretic quadrupole and microwell electrodes. *Biosensors & bioelectronics*, 24(12):3637–44, 2009.

[29] Zachary Gagnon and Hsueh-Chia Chang. Aligning fast alternating current electroosmotic flow fields and characteristic frequencies with dielectrophoretic traps to achieve rapid bacteria detection. *Electrophoresis*, 26(19):3725–37, October 2005.

[30] J Cao, P Cheng, and F Hong. A numerical analysis of forces imposed on particles in conventional dielectrophoresis in microchannels with interdigitated electrodes. *Journal of Electrostatics*, 66(11-12):620–626, 2008.

[31] Stuart J. Williams, Pramod Chamarthy, and Steven T. Wereley. Comparison of Experiments and Simulation of Joule Heating in ac Electrokinetic Chips. *Journal of Fluids Engineering*, 132(2):021103, 2010.

[32] Ivan R Perch-Nielsen, Nicolas G Green, and Anders Wolff. Numerical simulation of travelling wave induced electrothermal fluid flow. *Journal of Physics D: Applied Physics*, 37(16):2323–2330, August 2004.

[33] Meng Lian and Jie Wu. Microfluidic flow reversal at low frequency by AC electrothermal effect. *Microfluidics and Nanofluidics*, 7(6):757–765, March 2009.

[34] E Du and Souran Manoochehri. Electrohydrodynamic-mediated dielectrophoretic separation and transport based on asymmetric electrode pairs. *Electrophoresis*, 29(24):5017–25, 2008.

[35] J. Cao, P. Cheng, and F. J. Hong. A numerical study of an electrothermal vortex enhanced micromixer. *Microfluidics and Nanofluidics*, 5(1):13–21, 2007.

[36] Louise M Barrett, Andrew J Skulan, Anup K Singh, Eric B Cummings, and Gregory J Fiechtner. Dielectrophoretic manipulation of particles and cells using insulating ridges in faceted prism microchannels. *Analytical chemistry*, 77(21):6798–804, 2005.

[37] Kwan Hyoung Kang, Xiangchun Xuan, Yuejun Kang, and Dongqing Li. Effects of dc-dielectrophoretic force on particle trajectories in microchannels. *Journal of Applied Physics*, 99(6):064702, 2006.

[38] Kwan Hyoung Kang, Yuejun Kang, Xiangchun Xuan, and Dongqing Li. Continuous separation of microparticles by size with direct current-dielectrophoresis. *Electrophoresis*, 27(3):694–702, 2006.

[39] Yuejun Kang, Dongqing Li, Spyros A Kalams, and Josiane E Eid. DC-Dielectrophoretic separation of biological cells by size. *Biomedical microdevices*, 10(2):243–9, April 2008.

[40] Y Kang, B Cetin, Z Wu, and D Li. Continuous particle separation with localized AC-dielectrophoresis using embedded electrodes and an insulating hurdle. *Electrochimica Acta*, 54(6):1715–1720, 2009.

[41] Soumya K Srivastava, Prashant R Daggolu, Shane C Burgess, and Adrienne R Minerick. Dielectrophoretic characterization of erythrocytes: positive ABO blood types. *Electrophoresis*, 29(24):5033–46, December 2008.

[42] John David Jackson. *Classical Electrodynamics*. John Wiley &Sons, Ltd, third edition, 1998.

[43] Antonio Ramos, Hywel Morgan, and Antonio Castellanos. AC Electrokinetics: A Review of Forces in Microelectrode Structures. *Journal of Physics D: Applied Physics*, 31:2338–2353, 1998.

[44] Frank M White. *Viscous Fluid Flow*. Mcgraw Hill, 3rd edition, 2003.

[45] J Lyklema. *Fundamentals of Interface and Colloid Science: Volume II: Solid-Liquid Interfaces*. Academic Press, New York, NY, 1995.

[46] Vishal Tandon, Sharath K Bhagavatula, Wyatt C Nelson, and Brian J Kirby. Zeta potential and electroosmotic mobility in microfluidic devices fabricated from hydrophobic polymers: 1. The origins of charge. *Electrophoresis*, 29(5):1092–101, 2008.

[47] Vishal Tandon and Brian J Kirby. Zeta potential and electroosmotic mobility in microfluidic devices fabricated from hydrophobic polymers: 2. Slip and interfacial water structure. *Electrophoresis*, 29(5):1102–14, 2008.

[48] a Castellanos, a Ramos, a González, N G Green, and H Morgan. Electrohydrodynamics and dielectrophoresis in microsystems: scaling laws. *Journal of Physics D: Applied Physics*, 36(20):2584–2597, October 2003.

[49] CRC. *CRC handbook of chemistry and physics*. Knovel, Binghamton, NY, 90 edition, 2010.

[50] Adrian Bejan. *Heat Transfer*. John Wiley &Sons, Ltd, New York, NY, 1993.

[51] Zeon Chemicals. Zeonor 1020R Datasheet.

[52] S. Loire and I. Mezic. Separation of bioparticles using the travelling wave dielectrophoresis with multiple frequencies. *42nd IEEE International Conference on Decision and Control (IEEE Cat. No.03CH37475)*, 6(December):6448–6453, 2003.

[53] Brian Kates and Carolyn L Ren. Study of Joule heating effects on temperature gradient in diverging microchannels for isoelectric focusing applications. *Electrophoresis*, 27(10):1967–76, May 2006.

[54] Irena Barbulovic-Nad, Xiangchun Xuan, Jacky S H Lee, and Dongqing Li. DC-dielectrophoretic separation of microparticles using an oil droplet obstacle. *Lab on a chip*, 6(2):274–9, February 2006.

[55] Junjie Zhu, Tzuen-Rong J Tzeng, and Xiangchun Xuan. Continuous dielectrophoretic separation of particles in a spiral microchannel. *Electrophoresis*, 31(8):1382–8, April 2010.

[56] Prasanna K Thwar, Jennifer J Linderman, and Mark A Burns. Electrodeless direct current dielectrophoresis using reconfigurable field-shaping oil barriers. *Electrophoresis*, 28(24):4572–81, December 2007.

[57] Hope C Feldman, Marin Sigurdson, and Carl D Meinhart. AC electrothermal enhancement of heterogeneous assays in microfluidics. *Lab on a chip*, 7(11):1553–9, 2007.

[58] Xiangchun Xuan. Joule heating in electrokinetic flow. *Electrophoresis*, 29(1):33–43, January 2008.

[59] M. Trau, S. Sankaran, D. A. Saville, and I. A. Aksay. Electric-field-induced pattern formation in colloidal dispersions. *Nature*, 374(6521):437–439, March 1995.

[60] M. Trau, S. Sankaran, D. A. Saville, and I. A. Aksay. Pattern Formation in Nonaqueous Colloidal Dispersions via Electrohydrodynamic Flow. *Langmuir*, 11(12):4665–4672, December 1995.

CHAPTER 5

AUTOMATED DIELECTROPHORETIC CHARACTERIZATION OF *MYCOBACTERIUM SMEGMATIS*

5.1 Abstract

We report the positive dielectrophoretic (pDEP) characterization of wild-type and ethambutol-treated *Mycobacterium smegmatis* populations via automated pDEP cell trapping experiments. The automated technique was validated by measurements of carboxylate-modified polystyrene microspheres and *Escherichia coli*. The characterization of *M. smegmatis* identifies a key frequency regime where the membrane-specific action of ethambutol leads to a change in the cellular dielectrophoretic response. This work highlights the potential for DEP measurements to measure changes in mycobacterial membrane properties associated with chemical treatments or genetic mutation.

5.2 Introduction

Dielectrophoresis (DEP) is the transport of polarizable particles in response to a nonuniform electric field, exclusive of electrophoresis [1]. DEP forces depend on the magnitude and nonuniformity of an externally applied electric field, as well as the complex permittivity of a particle and its surrounding media [2]. The complex permittivities ($\tilde{\varepsilon} = \varepsilon - i\sigma/\omega$) of the particle and surrounding media are a function of the frequency of the polarizing electric field, ω, electrical conductivity, σ, and permittivity, ε; the permittivity, ε, is assumed independent of frequency over the range used in this study. The

[0]The content of this chapter was submitted for publication as a research article titled "Automated dielectrophoretic characterization of *Mycobacterium smegmatis*" in the journal *Analytical Chemistry*. Reproduced with permission from *Analytical Chemistry*. Copyright 2010 American Chemical Society.

combination of material- and frequency dependence makes DEP a useful technique for researchers attempting to manipulate, separate, and characterize particles and cells.

In this work, we present an automated DEP-based characterization technique and apply it to the bacterial species *Mycobacterium smegmatis*. *M. smegmatis* is a non-pathenogenic, acid-fast, gram-positive bacteria with a membrane structure similar to other, pathogenic species such as *Mycobacterium tuberculosis*. The outer layer of *M. smegmatis* is composed of covalently attached lipids, namely, α-, keto-, and methoxy-mycolic acids. Some *Mycobacteria* additionally possess a pseudo-capsule of non-covalently attached lipids. Mycolic acids, specifically the complex trehalose dimycolate in *M. tuberculosis*, are responsible for the host inflammatory and granulomatous responses [3, 4] that are the primary symptoms of tuberculosis infection. In addition to their adjuvant effects on the host immune system, the lipid content of mycobacterial species forms a dense, hydrophobic barrier to antibiotics, contributing to mycobacterial drug resistance. These membrane lipids are bound to the polysaccharide arabinogalactan [5]. The anti-mycobacterial drug ethambutol inhibits biosynthesis of arabinogalactan, limiting mycolate attachment sites and significantly altering membrane composition [6]. Due to its role in pathogenicity and host immune response, the exterior lipid composition of the cell membrane of mycobacterial species is relevant to studies of membrane biosynthesis, drug resistance, and pathogenicity.

DEP devices have been used to characterize and separate a variety of species, e.g. bacterial populations[7, 8, 9, 10], mammalian cells[11, 12, 13, 14], DNA[15], proteins[16, 17, 18, 19], and viruses[20]. DEP separation techniques are often binary, centering on the cross over frequency — at which the sign of the DEP force changes. For samples with different cross over frequencies, there exists a frequency regime where the DEP force is positive for one population and negative for another. Another class of

DEP-based separation techniques depend on differences in the magnitude of the DEP force at a particular frequency[7, 21, 22, 10]. Because the cross over frequency can be insensitive to changes in cell membrane composition (the primary component affected by ethambutol), it is beneficial to investigate separation techniques that depend on the magnitude of the DEP force. These separation techniques require characterization of cellular dielectric response as a function of frequency in order to determine the optimal regime for efficient operation.

5.3 Theory

We employ a combination of numerical and analytical techniques to model particle behavior near an interdigitated electrode array. The configuration of the array and the direction of positive DEP forces are shown in 5.1.

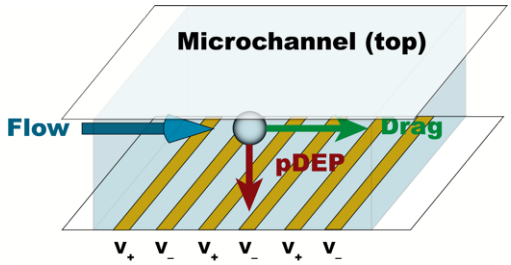

Figure 5.1: (color online) An interdigitated electrode array is configured with alternating positive (V_+) and negative (V_-) electrodes on the bottom of a microfluidic channel. Fluid drag moves particles with the direction of flow while pDEP forces attract particles to the electrode array. Negative DEP forces repel particles from the array.

5.3.1 Dielectrophoresis and Cell Modeling

We start by considering a sphere in an infinite domain with homogeneous and isotropic complex permittivities. If a uniform field $\mathbf{E} = \mathbf{E}_0 \cos(\omega t)$ is applied, the contribution

of a polarized sphere to the total electric field can be described using an electric dipole with a moment[23, 2, 24], $\mathbf{p} = \mathbf{p}_0(\cos\omega t + \varphi)$:

$$\mathbf{p}_0 = 4\pi\varepsilon_m a^3 \left| \frac{\tilde{\varepsilon}_p - \tilde{\varepsilon}_m}{\tilde{\varepsilon}_p + 2\tilde{\varepsilon}_m} \right| \mathbf{E}_0 \tag{5.1}$$

where a is the particle radius, $\mathbf{E}$ is the externally applied electric field and the subscripts m and p refer to the medium and particle, respectively. If the field is slightly nonuniform over the length scale of the particle, then the force on the dipole will be:

$$\mathbf{F} = \mathbf{p} \cdot \nabla \mathbf{E} \tag{5.2}$$

Using the appropriate vector identities[1] and assumptions[2], this yields[2] the following expression for the time-averaged dielectrophoretic force:

$$\langle \mathbf{F}_{\mathrm{DEP}} \rangle = \pi\varepsilon_m a^3 \tilde{f}_{\mathrm{CM}} \nabla(\mathbf{E}_0 \cdot \mathbf{E}_0) \tag{5.3}$$

For ellipsoidal particles (specifically, a prolate spheroid), a change of variables can be performed and a similar analytical solution can be found[2, 25] for particles oriented with their long axis parallel to the external electric field (along the z axis):

$$\langle \mathbf{F}_{\mathrm{DEP},z} \rangle = \pi\varepsilon_m l_z l_{x,y}^2 \Re \left[\frac{\tilde{\varepsilon}_p - \tilde{\varepsilon}_m}{3\left[\tilde{\varepsilon}_m + (\tilde{\varepsilon}_p - \tilde{\varepsilon}_m) L_z\right]} \right] \nabla(\mathbf{E}_0 \cdot \mathbf{E}_0) \tag{5.4}$$

[1] For any vectors $\mathbf{A}$ and $\mathbf{B}$:

$$\nabla(\mathbf{A}\cdot\mathbf{B}) = (\mathbf{A}\cdot\nabla)\mathbf{B} + (\mathbf{B}\cdot\nabla)\mathbf{A} + \mathbf{B}\times(\nabla\times\mathbf{A}) + \mathbf{A}\times(\nabla\times\mathbf{B})$$
$$\nabla\times(\mathbf{A}\times\mathbf{B}) = (\mathbf{B}\cdot\nabla)\mathbf{A} - (\mathbf{A}\cdot\nabla)\mathbf{B} + (\nabla\cdot\mathbf{B})\mathbf{A} - (\nabla\cdot\mathbf{A})\mathbf{B}$$

[2] Specifically, that the electric field is curl-free and there is no free charge: $\nabla\times\mathbf{E} = 0$ and $\nabla\cdot\mathbf{E} = 0$.

where l_z and $l_x(=l_y)$ are the lengths of the major and minor axes, respectively. L_z is the "depolarizing factor" along the major axis:

$$L_z = \frac{l_{x,y}^2}{2l_z^2 e^3}\left[\ln\left(\frac{1+e}{1-e}\right) - 2e\right] \tag{5.5}$$

where $e = \sqrt{1 - l_{x,y}^2/l_z^2}$ is the particle eccentricity.

In order to describe particles with inhomogenous complex permittivity such as cells, a multishell model is often invoked, using spherically symmetric layers of constant thickness, permittivity, and conductivity[26, 27, 28]. For a spherical particle composed of shells of homogeneous, isotropic complex permittivity, $\langle \mathbf{F}_{\mathrm{DEP}} \rangle$ can be described using a single *effective* complex particle permittivity. Using the same change of variables, an ellipsoidal particle can also be described using the multishell approach, if the shells can be approximated as confocal. Though this is typically not exact for cells, the ellipsoidal multishell model provides a convenient analytical tool to describe coccoidal bacteria. A prolate spheroid with a single shell of complex permittivity, $\tilde{\varepsilon}_s$, has a dipole coefficient (analogous to $\tilde{f}_{\mathrm{CM}}$ for spherical particles):

$$\tilde{K}_{z,1} = \frac{\tilde{\varepsilon}_p - \tilde{\varepsilon}_m}{3\left[\tilde{\varepsilon}_m + L_1\left(\tilde{\varepsilon}_s - \tilde{\varepsilon}_m\right)\right] + 9\tilde{K}_{z,0}\gamma L_1\left(1 - L_1\right)\left(\tilde{\varepsilon}_s - \tilde{\varepsilon}_m\right)} \tag{5.6}$$

where γ is the ratio of volumes of the core to the whole spheroid and $\tilde{K}_{z,0}$ is the spheroidal complex Clausius-Mossotti factor:

$$\tilde{K}_{z,0} = \frac{\tilde{\varepsilon}_p - \tilde{\varepsilon}_s}{3\left[\tilde{\varepsilon}_s + L_1\left(\tilde{\varepsilon}_p - \tilde{\varepsilon}_s\right)\right]} \tag{5.7}$$

Additional shells can be added as described by Castellarnau, et al. [10], and Huang, et

al.[29], with the nth shell factor described as:

$$\tilde{K}_{z,n} = \frac{1}{3}\frac{(\tilde{\varepsilon}_m - \tilde{\varepsilon}_{n-1}) + 3\tilde{K}_{z,n-1}x_{n-1}(\tilde{\varepsilon}_{n-1} + L_{z,n}(\tilde{\varepsilon}_m - \tilde{\varepsilon}_{n-1}))}{(\tilde{\varepsilon}_m + L_{z,n}(\tilde{\varepsilon}_{n-1} - \tilde{\varepsilon}_m)) + 3\tilde{K}_{z,n-1}x_{n-1}L_{z,n}(1 - L_{z,n})(\tilde{\varepsilon}_{n-1} - \tilde{\varepsilon}_m)} \quad (5.8)$$

$$x_n = \frac{\left(hl_{x,y} + \sum_{k=1}^{n-1}\delta_k\right)\left(l_{x,y} + \sum_{k=1}^{n-1}\delta_k\right)^2}{\left(hl_{x,y} + \sum_{k=1}^{n}\delta_k\right)\left(l_{x,y} + \sum_{k=1}^{n}\delta_k\right)^2} \quad (5.9)$$

$$L_{z,n} = \frac{1 - e_n^2}{2e_n^3}\left[\log\left(\frac{1 + e_n}{1 - e_n}\right) - 2e_n\right] \quad (5.10)$$

$$e_n = \sqrt{1 - \left(\frac{l_{x,y} + \sum_{k=1}^{n}\delta_k}{hl_{x,y} + \sum_{k=1}^{n}\delta_k}\right)} \quad (5.11)$$

where $h = l_z/l_{x,y}$ is the particle spheroid aspect ratio ($h > 1$ for a prolate spheroid), and δ_n refers to the thickness of the nth shell. In an effort to account for some of the error induced by the confocal shell approximation, specifically that incurred due to varying shell thicknesses, Equations 9 and 11 redefine the volume ratio, x_n, and eccentricity, e_n, to exclude the aspect ratio, h, from the shell thickness parameter, δ_n.

In this study, a three-shell model ($n = 5$) was used to approximate the structure and composition of bacterial samples. This model accounts for the complex permittivity and relative sizes of the cytoplasm ($n = 1$), cytoplasmic membrane ($n = 2$), cell wall ($n = 3$), and media ($n = 5$). The outer shell ($n = 4$) of the particle was used to approximate the outer membrane in *E. coli* samples and the covalently bound lipids in *M. smegmatis* samples.

Polystyrene microspheres are modeled as a homogeneous particle with a surface conductance that contributes significantly to the effective particle conductivity[30, 31, 32, 33]:

$$\sigma_p = \sigma_{p,\text{bulk}} + 2\frac{K_s}{a} \quad (5.12)$$

where $\sigma_{p,\text{bulk}}$ is the bulk particle conductivity and K_s is the surface conductance.

5.3.2 Electric Field and Cell Collection Modeling

The DEP force is a direct function of the electrical properties of the particle and the fluid medium (related by the real part of the Clausius-Mossotti factor, $\Re[\tilde{f}_{\text{CM}}]$), as well as the magnitude and frequency of the applied electric field. To characterize the DEP response of particles and cells, we fabricated a device with a microchannel defined in poly(dimethylsiloxane) (PDMS) and bonded on top of gold interdigitated electrodes deposited on glass (5.2, inset). In certain ranges of electric field magnitude and frequency, the positive DEP force acting on a particle will overcome fluid drag and trap the particle onto the electrodes. The intensity of trapped, fluorescently labeled particles was recorded over time, and was fit to a series of physically informed functions such that a quantitative measure of particle trapping, a "threshold trapping potential", can be defined and compared between trials and samples. This trapping potential data is inversely proportional to the square root of $\Re[\tilde{f}_{\text{CM}}]$ and allows for the relative magnitudes of the particles' DEP responses to be measured.

The electric field above a pair of interdigitated electrodes can be approximated by assuming that the gap between the electrodes is differentially small. The resulting expressions for the electric field and the dielectrophoretic force on a homogeneous spherical particle are[7, 34]:

$$\mathbf{E} = \frac{V}{\pi}\frac{\hat{\theta}}{r} \tag{5.13}$$

$$\langle \mathbf{F}_{\text{DEP}} \rangle = \frac{a^3 \varepsilon_{\text{m}}}{3\pi r^3} \Re[\tilde{f}_{\text{CM}}] V^2 \hat{r} \tag{5.14}$$

where $\hat{\theta}$ and $\hat{r}$ are unit vectors in cylindrical coordinates, r is the radial distance from the center of the electrode gap, and V is the applied potential. We assume that in order to trap a particle, $\langle \mathbf{F}_{\mathrm{DEP}} \rangle$ must be equivalent to the fluid drag on a particle. This is a gross approximation that neglects the fluid velocity, but our goal is only to determine the functional relationship between the DEP force and the trapping potential.

Following the analysis of Sanchis, et al.[7], we calculate the time required to trap a particle on the electrode array from a distance r_{trap} from the electrode gap. During this time, a semi-cylindrical volume of cells is trapped on the array. The resulting relationship gives the approximate number of cells on the array after a time, Δt, given a cell number density, n_0.

$$N \approx n_0 \frac{\pi r_{trap}^2 w}{2} \approx \frac{n_0 w a V}{6} \sqrt{\frac{2\varepsilon_{\mathrm{m}} \Re[\tilde{f}_{\mathrm{CM}}] \Delta t}{\eta}} \tag{5.15}$$

We can rearrange this relationship to express $\tilde{f}_{\mathrm{CM}}$ as a function of the trapping potential, V_{trapping}:

$$\Re[\tilde{f}_{\mathrm{CM}}] \sim \frac{\eta}{n_0 w a} \frac{N^2}{\Delta t} \frac{1}{V_{\mathrm{trapping}}^2} \tag{5.16}$$

The number density and trapping time, Δt, are fixed parameters in the experiment, so the number of cells collected is a function of $\Re[\tilde{f}_{\mathrm{CM}}]$. Rather than measuring the number of captured cells, as done in other DEP collection experiments[7, 13], we measure the potential required to trap a particular number of cells, defined by a threshold value of fluorescence intensity I_{max}, discussed in the next section, because this is less sensitive to variations in particle concentration and fluid velocity.

5.3.3 Data Collection and Analysis

An automated data collection scheme was developed to measure particle trapping as a function of electric field frequency and magnitude. A custom LabVIEW interface controlled the electric field inputs of the experiment — magnitude, frequency, "on" duration, and "off" duration — and recorded the fluorescence intensity outputs. Fluorescence intensity was integrated over a region of interest and normalized by the number of pixels to give an average pixel intensity. The average pixel intensity is then a function of the magnitude of the DEP force, which in turn depends on particle composition and on electric field magnitude and frequency. Inflow particle density was assumed uniform and constant throughout all experiments. Variations in particle fluorescence intensity were controlled by careful staining protocols and corrected for during data analysis by background subtraction.

The spatially averaged pixel intensity was recorded over the course of the experiment for two separate regions of interest: upstream of the electrode array (ROI-1) and around the gaps between the first, second, and third electrodes (ROI-2, 5.2). ROI-1 was used as a representative measure of background signal to account for changes in particle concentration. ROI-2 measured the intensity of particles trapped on the array. The order in which frequencies were applied was randomized for every repetition. Three repetitions were performed for every trial and, for biological samples, each trial was a separately cultured and prepared sample.

In order to quantitatively compare sample DEP response, a series of analyses was performed to account for background fluorescence, particle density fluctuations, and permanent particle adhesion to the electrodes. First, the raw intensity data recorded in LabVIEW was loaded in MATLAB, and the background signal, ROI-1, was subtracted from the particle trapping data, ROI-2. The data recorded during the electric field "off"

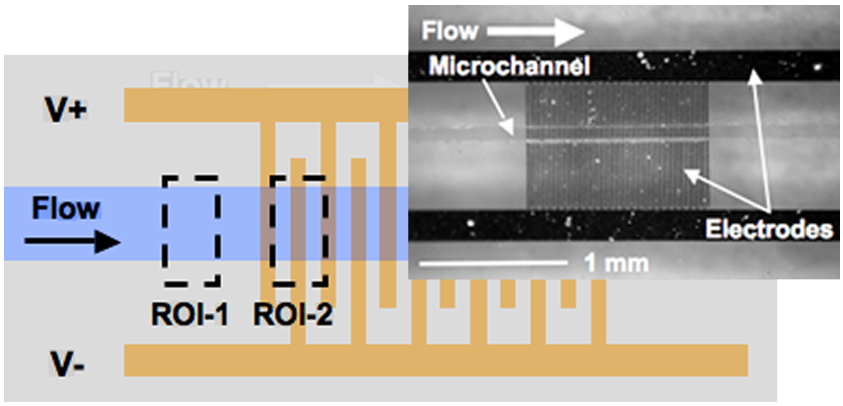

Figure 5.2: Interdigitated electrode array schematic with regions of interest (ROI-1 and ROI-2) defined. The average pixel intensity in ROI-1 was used as a background intensity signal proportional to particle density and fluorescence staining intensity. The average pixel intensity in ROI-2 was used as a measure of particle trapping. Inset shows a top view of the fabricated device with PDMS channel.

time was smoothed by a locally weighted scatterplot smoothing function, and the minimum of this smoothed curve was subtracted from the entire data set; this step further removes background signal and accounts for permanent particle adhesion. Next, each data subset corresponding to a specific applied voltage (e.g., 0 through 1.5 V, shown in 5.3) was fit to a quadratic curve which served as a low-pass filter for measurement noise. This method was repeated for all voltage data sets at each applied frequency, and the maximum intensity value, $I_{\max}$, of the fits across the whole dataset was recorded. Finally, the peaks of the quadratic curves were fit to a sigmoidal curve with a peak plateau region set to $I_{\max}$.

$$I_{\text{fit}} = \frac{I_{\max}}{1 + \frac{e^{-nx}}{b}} \tag{5.17}$$

Fitting all frequency data sets to one peak value corrected for experimental variability due to particle concentration and electrode surface contamination between runs. A sigmoidal fit was chosen because it characterizes the trapping behavior of particles well, including a lower region before trapping is observed and a saturation region as

the trapped particles fill the space near the electrodes. If the goodness of the sigmoidal fit did not exceed a defined threshold ($R^2 > 0.7$), then the dataset from that particular applied frequency was excluded from further analysis.

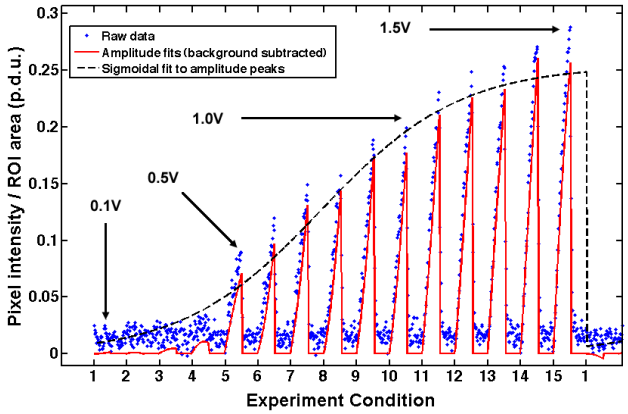

Figure 5.3: Raw average pixel intensity data from ROI-2 (blue points, color online) was fit to quadratic curves (solid red) at each "experiment condition" — corresponding to a particular frequency–potential pair. In this example dataset, taken at 1kHz with polystyrene beads, experimental conditions 1–15 correspond to applied potentials of 0.1V–1.5V in 0.1V increments. The peaks of each quadratic fit were fit to a sigmoid (dashed black) whose plateau was determined by the maximum measured average pixel intensity for all frequency–potential pairs in a trail.

The threshold trapping potential, V_{trapping}, for each applied frequency was defined as the voltage at which the sigmoidal fit function at that frequency has a value of $I_{\text{max}}/2$; for frequencies at which DEP forces are weak, this gives V_{trapping} values larger than the experimental voltage range, with increased uncertainty associated with the extrapolation of the data. The trapping potential as a function of frequency was obtained for polystyrene particles in solutions of varying conductivity as well as bacterial cell cultures. The inverse square of the trapping potential data was calculated to compare the relative DEP response magnitudes of the particles and cells.

5.4 Materials and Methods

5.4.1 Device Fabrication

Electrodes were fabricated using standard lift-off photolithography. 4 inch borofloat glass wafers were cleaned using hot piranha solution and vapor primed using HMDS. Microposit® S1818 photoresist was spun onto the wafers at 3000rpm for 30 seconds and baked at 115°C for 60 seconds. Photoresist was exposed using a EV620 contact aligner in soft-contact mode for 2 seconds (12mW/cm^2). Photoresist was developed in Microposit® MF-321 for 120 seconds. Wafers were then treated for 90 seconds with oxygen plasma to descum and then placed in a CVC SC4500 electron-beam evaporator. 200nm of gold was deposited between 50nm and 10nm layers of chrome. Lift off was performed in Microposit® Remover 1165 for 12 hours. Wafers were then coated with resist and diced (K&S 7100 Dicing Saw).

Fluid channel fabrication was accomplished using standard soft lithography. First, a silicon master was fabricated with 25μm tall features using standard photolithography. Wafers were coated with Microposit® S1818 photoresist (3000rpm, 30 seconds) and exposed for 2 seconds (12 mW/cm^2). Features were etched to a depth of 25μm using a Unaxis 770 Bosch reactive ion etch tool and resist stripped with reactive oxygen plasma (Gasonics Aura 1000). Wafers were coated with 1H,1H,2H,2H,Perfluorooctyltrichlorosilane (FOTS) using a vacuum evaporation process to prevent PDMS adhesion. Poly(dimethylsiloxane) monomer and curing agent were mixed in a 15:1 ratio for 5 minutes and placed under vacuum to remove bubbles. PDMS mixture was then poured over the silicon master in a custom made jig and placed in an oven to cure for 12 hours at 60°. PDMS devices were cut to size and via holes punched using a biopsy punch. PDMS channels and electrode devices were plasma

cleaned in an air plasma at 250 mTorr vacuum for 45 seconds (Harrick Plasma) and immediately bonded. Electrodes were wired using silver conductive epoxy.

5.4.2 Sample Preparation

Lyophilized *E. coli* (K-12 wild-type, EMG 2: K (lambda), ATCC® 23716™, passage 1-2) and *M. smegmatis* (mc(2)155, ATCC® 700084™, passage 1-2) samples were obtained from ATCC and grown in LB media and Middlebrook 7H9 media with OADC enrichment (100mL/L), respectively. Media solutions were obtained from Becton/Dickinson and prepared as directed by the manufacturer, with the exception of using OADC enrichment in Middlebrook 7H9 media. *E. coli* cells were grown in liquid media (10mL LB broth) in an incubating shaker at 37°C and 350rpm for 24 hours. *E. coli* were then plated in Petri dishes on LB Agar (prepared as directed by the manufacturer) and incubated for 24 hours at 37°C. *M. smegmatis* cells were grown under the same conditions in liquid media (10mL Middlebrook 7H9) for 48 hours. *M. smegmatis* cells were then plated on LB Agar with 0.5mL/L Tween80 and incubated for 48 hours at 37°C. Petri dishes were then sealed with paraffin, inverted, and refrigerated.

E. coli cells were taken from first or second passage solid culture and placed in 10mL of LB media in sterile 14mL polystyrene culture tubes (loosely capped). Samples were allowed to grow through log phase to stationary phase ($18-24$ hours) before preparation. *M. smegmatis* samples were prepared identically with the exception of culture media (Middlebrook 7H9 with OADC enrichment) and growth time to stationary phase ($36-48$ hours). Cells were grown to stationary phase — as determined by representative growth rate experiments, optical density (OD_{650}) measurements (data not shown), and data available in literature[35] — prior to preparation. To assess the im-

pact of changing cell membrane composition, samples of *M. smegmatis* were treated with ethambutol (ETB) at a concentration of 10μg/mL after 24 hours of growth and the treatment was maintained at this concentration throughout preparation and experiment. Growth in liquid culture was carried out in an incubating shaker at 37°C at 350 rpm. 1mL samples were removed and placed in centrifuge tubes and spun down at 5000×g for 10 minutes. The samples were resuspended in 0.85% (w/v) NaCl in deionized water and allowed to incubate for 1 hour. Samples were then spun down again and resuspended in 0.85% (w/v) NaCl with 4μL/mL of BACLight live/dead stain (Molecular Probes®) and allowed to incubate in the dark (culture oven, 37°C) for 1 hour. The samples were then washed once with and then resuspended in 0.5% (w/v) Tween80 solution (a subset of *E. coli* samples were processed in DI water for comparison). *Mycobacterium smegmatis* samples were analyzed to confirm that treatment with ethambutol did not affect fluorescence intensity or significantly alter cell size. A representative sample was evaluated using Phylum analysis software for cell length and diameter as well as average intensity. Wild-type and ethambutol-treated samples exhibited lengths of 1.24μm and 1.33μm with standard deviations of 0.14μm and 0.11μm, respectively. Average pixel intensity per cell was 1037p.d.u. (WT) and 1041p.d.u (ETB) with standard deviations of 49.9 and 45.1, respectively.

Fluoresbrite® 1.75μm-diameter carboxylate-modified polystyrene microspheres (beads) were obtained from Polysciences, Inc. Beads were spun down at 5000×g for 10 min and resuspended in DI water with trace amounts of salt (KCl) to control conductivity. Particles were diluted to a density of $\sim 4.25 \times 10^6$ particles/mL in polystyrene bead samples.

5.4.3 Data Collection and Processing

Prepared samples were drawn into a Hamilton GASTIGHT 1000 1mL glass syringe (Hamilton Company, USA) and dispensed at a rate of 10μL/hr using a Chemyx Fusion 400 syringe pump. The precision glass syringe and high step resolution of the syringe pump (0.02μm) combined to significantly reduce variability in the volumetric flow rate. The syringe was coupled to the PDMS channel using a 30-gauge needle and Tygon® Microbore tubing (OD: 0.76mm; ID: 0.25mm). Electric potentials were applied to the electrode array using an Agilent 33200A arbitrary waveform generator and controlled using a custom LabVIEW interface (National Instruments Corporation, USA).

The LabVIEW interface controlled the electric field frequency, magnitude, "on" time, and "off" time. The "on" time was fixed at 3 seconds for all experiments and the "off" time was 3 seconds for polystyrene bead samples and 5 seconds for biological samples. Electric field frequencies were randomized and tested at every potential, from 0.1V to 1.5V in 0.1V increments (2.5V in 0.2V increments in ethambutol-treated *M. smegmatis* experiments) to minimize electrode fouling over the courses of the experiment.

Particle trapping was measured using a Nikon LV100 upright microscope using long working distance objectives (Nikon S Plan Fluor, $40\times/0.60$, $3.6-2.8$mm), a EXFO X-Cite Series 120 fluorescence excitation source, and a QImaging EXiFast Blue high speed monochrome CCD camera.

5.5 Results and Discussion

Polystyrene Microspheres Carboxylate-modified polystyrene microspheres were tested in solutions with three different conductivities (adjusted using KCl) to show that, as expected, trapping potential increases in the low-frequency regime. This is consistent with a decrease in $\Re[\tilde{f}_{\mathrm{CM}}]$ over the same frequency range. The apparent cross over frequency is $\sim 10^6$Hz, decreasing with increasing conductivity in Figures 5.4(a) and 5.4(b).

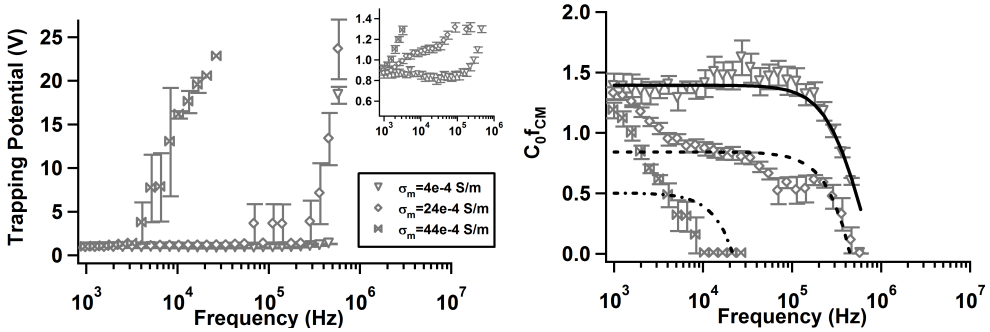

(a) (b)

Figure 5.4: Trapping potential, V_{trapping}, Figure 5.4(a), and $1/V^2_{\mathrm{trapping}}(\propto \Re[\tilde{f}_{\mathrm{CM}}])$, Figure 5.4(b), as a function of frequency for 1.75μm-diameter carboxylate-modified polystyrene particles suspended in aqueous solutions with conductivities $\sigma_m = 4\times10^{-4}$, $\sigma_m = 24\times10^{-4}$, and $\sigma_m = 44\times10^{-4}$S/m. Inset in 5.4(a) expands the low potential range for clarity. Curve fits in 5.4(b) were calculated using an effective surface conductance model (Equation 5.12). Error bars represent standard error of the mean: $S_e = S_d/\sqrt{n}$ where S_d is the standard deviation. The symbol C_0 denotes an arbitrary constant related to the flow rate and electrode geometry.

The homogenous sphere model for polystyrene in water neglects the significant surface conductance that dominates the particle response at low frequency. It has been shown by several researchers that carboxylate-modified polystyrene microspheres posess a significant surface conductance that contributes to particle dielectrophoretic behavior[36, 32, 33, 37, 31]. The cross over frequency predicted by a homogenous particle model remains constant at low medium conductivity ($<\sim 1\times10^{-3}$S/m) then

decreases rapidly and disappears when $\tilde{\varepsilon}_m > \tilde{\varepsilon}_p$[31]. The experimentally observed decrease in cross over frequency with increasing conductivity is often attributed to surface conductance and double-layer polarization effects[31]. Low conductivity data was well-fit using a simple surface conductivity model (Equation 5.12) with the parameters listed in 5.1. However, as conductivity increased, the model becomes less appropriate, as evidenced by decreasing values of R^2. Fits shown in Figure 5.4(b) were calculated using the constants listed in 5.1 with C_0 and K_s as free parameters. C_0 is a scaling constant related to flow conditions and electrode geometry.

Table 5.1: Multivariable fit coefficients chosen to match experimental measurements of the real part of the Clausius-Mossotti factor, $\Re[\tilde{f}_{\mathrm{CM}}]$, for carboxylate-modified polystyrene particles in solutions of increasing conductivity. Parameters are divided into fixed (above) and free (below) groups.

Parameter	$\sigma_m = 0.4$mS/m	$\sigma_m = 2.4$mS/m	$\sigma_m = 4.4$mS/m
ε_p	2.5	2.5	2.5
ε_m	78.5	78.5	78.5
σ_p	1×10^{-12}S/m	1×10^{-12}S/m	1×10^{-12}S/m
r	0.876×10^{-6}m	0.876×10^{-6}m	0.876×10^{-6}m
K_s	$2.13 \times 10^{-9} S$	$1.5 \times 10^{-9} S$	$1.9 \times 10^{-9} S$
C_0	1.33	2.71	70.7
R^2	0.942	0.417	0.11

Eschericia coli As additional verification of our experimental data collection and data analysis techniques, we measured the pDEP response of *E. coli* in DI water and 0.5% (w/v) Tween80 solution. The results, 5.5, show a constant trapping potential for low frequency which increases above 10^5Hz and peaks $\sim 10^6$Hz before decreasing again. This is consistent with our model predictions for *E. coli* as well as experimental results obtained by Sanchis, et al[7] and Castellarnau, et al [10].

The data were well fit using the spheroidal 3-shell model discussed previously (i.e., Equation 5.8). Initial fits were performed with constraints determined by values ob-

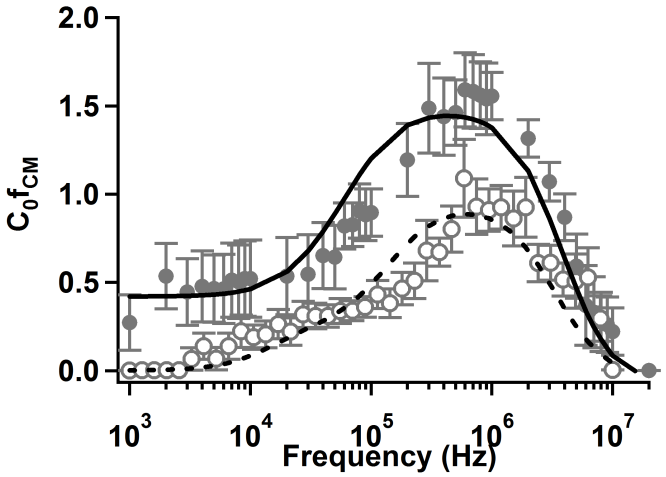

Figure 5.5: $1/V^2_{\text{trapping}} (\propto \Re[\tilde{f}_{\text{CM}}])$ as a function of frequency for wild-type *E. coli* suspended in DI water (filled circles, $\sigma_m \approx 0.05$mS/m) and 0.5% (w/v) Tween80 solution (open circles, $\sigma_m \approx 1$mS/m). Curve fits for *E. coli* in DI water (solid) and 0.5% (w/v) Tween80 solution (dashed) were calculated using a multivariate nonlinear least squares technique to a spheroidal multishell model. Error bars represent standard error of the mean. The symbol C_0 denotes an arbitrary constant related to the flow rate and electrode geometry.

tained in the literature[10, 7]. After initial fitting, cytoplasmic, plasma membrane, and cell wall coefficients were fixed along with outer membrane conductivity, allowing the permittivity of the outer membrane to vary. The results of fitting are given in 5.2. In the presence of 0.5% (w/v) Tween, the outer membrane permittivity increased by a factor of three. While by no means conclusive, this result suggests that the presence of the surfactant in solution may have interacted with the outer membrane and contributed to the local effective permittivity.

Mycobacterium smegmatis *M. smegmatis* is a gram-positive bacterium with both a different shape and different composition from *E. coli*. We therefore expect a different trapping response due to the presence of the lipid/mycolic acid region of the mycobacterial envelope. Indeed, we do observe such a distinction, particularly below $\sim 10^6$Hz where *E. coli* samples exhibit significant low-frequency dispersion that is not observed

Table 5.2: Multivariable fit coefficients for the Clausius-Mossotti factor, $\Re[\tilde{K}_z]$, for *E. coli* in deionized water and a 0.5% (w/v) solution of Tween80 (5.5). Parameters are divided into fixed (above) and free (below) groups.

Parameter	DI Water	0.5% (w/v)Tween80
ε_{cyto}	60	60
ε_{pmem}	2.3	2.3
ε_{wall}	60	60
σ_{cyto}	0.1S/m	0.1S/m
σ_{pmem}	6×10^{-6}S/m	6×10^{-6}S/m
σ_{wall}	1.9×10^{-4}S/m	1.9×10^{-4}S/m
σ_{mem}	2.2×10^{-6}S/m	2.2×10^{-6}S/m
r	0.5×10^{-6}m	0.5×10^{-6}m
δ_1	8×10^{-9}m	8×10^{-9}m
δ_2	15×10^{-9}m	15×10^{-9}m
δ_3	8×10^{-9}m	8×10^{-9}m
ε_{mem}	2	6.3
C_0	0.99	0.517
R^2	0.90	0.8075

in *M. smegmatis*. This low-frequency component to the DEP response is indicative of multiple Maxwell–Wagner relaxation frequencies, which can result when the interfaces between materials are not well defined. At still lower frequencies (i.e., $< 1 \times 10^4$Hz) the so-called α-relaxation associated with ion motion within the double layer is responsible for the observed pDEP response.

Treatment with ethambutol significantly alters the dielectrophoretic response of *M. smegmatis*. *Mycobacteria* are susceptible to modification of their membrane composition using ethambutol to inhibit the production of arabinogalactan and prevent the attachment of mycolic acids. The removal of the outer layer of lipids exposes the peptidoglycan[38, 5] and significantly decreases the effective permittivity of the cell. Treatment with ethambutol caused the values of $1/V^2_{\text{trapping}}$ to be significantly diminished and shifted toward higher frequencies ($\sim 10^6 - 10^7$Hz). The dramatic difference observed in 5.6 confirms the effect that ethambutol has on mycobacterial membrane

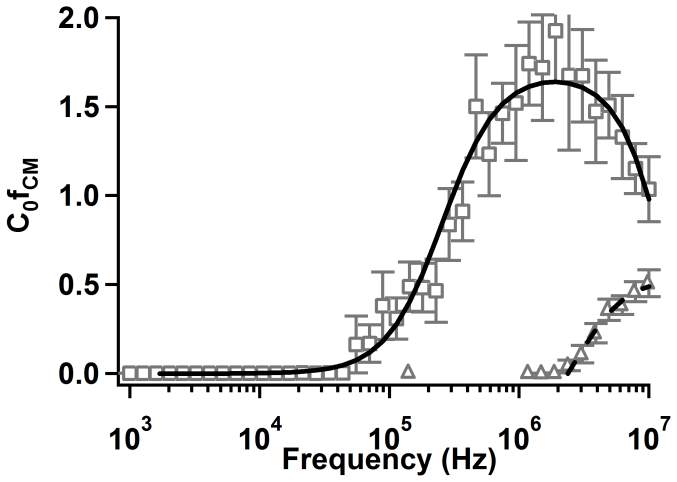

Figure 5.6: $1/V^2_{\text{trapping}} (\propto \Re[\tilde{f}_{\text{CM}}])$ as a function of frequency for wild-type (open squares) and ethambutol-treated (open triangles) *M. smegmatis* suspended in 0.5% (w/v) Tween80 solution ($\sigma_m \approx$ 1mS/m). Curve fits for wild-type (solid) and ethambutol-treated (dashed) samples were calculated using a multivariate nonolinear least squares technique to a spheroidal multishell model. Error bars represent standard error of the mean. The symbol C_0 denotes an arbitrary constant related to the flow rate and electrode geometry.

composition. The data in 5.6 can be fit using the spheroidal multishell model introduced earlier. Parameters used to generate curve fits are given in 5.3. The aspect ratio, h, for *M. smegmatis* was 3.3, calculated from measurements by Nguyen, et al.[39]. Thicknesses were estimated based on the work of Takade, et al.[40], and Paul, et al[41, 42, 43] and inferred from the curve fit process.

The results of the curve fitting analysis indicate a wide range of changes within the cell membrane as a result of treatment with ethambutol. There are slight variations in the permittivity and conductivity of the plasma membrane and cell wall, and an increase in cytoplasmic conductivity. The most dramatic change, however, occurs in the outer membrane or lipid region, where both the permittivity and conductivity increased to approximately those of the external media. The thickness of the lipid region also decreased. These are both suggestive of the anti-mycolic acid action of ethambutol, which has been shown to prevent the attachment of mycolic acids in the outer membrane.

Table 5.3: Multivariable fit coefficients for the Clausius-Mossotti factor, $\Re[\tilde{K}_{z,}]$, for wild-type and ethambutol-treated *M. smegmatis* in a 0.5% (w/v) solution of Tween80 (5.6). Parameters are divided into fixed (above) and free (below) groups.

Parameter	WT *M. smegmatis*	ETB-treated *M. smegmatis*
ε_{cyto}	70	70
r	0.3×10^{-6}m	0.3×10^{-6}m
δ_1	7×10^{-9}m	7×10^{-9}m
δ_2	40×10^{-9}m	40×10^{-9}m
ε_{pmem}	5.65	2
ε_{wall}	13	3
ε_{mem}	10.5	78.5
σ_{cyto}	0.3S/m	0.98S/m
σ_{pmem}	5.5×10^{-5}S/m	2.6×10^{-4}S/m
σ_{wall}	1.33×10^{-4}S/m	3.6×10^{-4}S/m
σ_{lipid}	1.0×10^{-4}S/m	11.5×10^{-4}S/m
δ_3	84×10^{-9}m	53×10^{-9}m
C_0	9.72	7.68
R^2	0.97	0.96

A wide array of techniques are available for characterization of the dielectrophoretic response of a sample. The majority rely on electrorotation[44, 45, 29, 11, 46] or measurements of the cross over frequency[10]. Electrorotation provides precise information about the cross over frequency while positive and negative DEP techniques provide more precise information about the direction of the DEP force. The use of DEP "collection spectra" has been employed to characterize a number of different cell types, to screen bacteria for antibiotic resistance, and to detect cancerous cells[47, 13, 48, 7]. By associating fluorescence intensity with collection spectra, we can automate the data collection and analysis process. The resulting quantitative characterization of V_{trapping} allows comparison of the magnitude of pDEP forces on a particular sample, a crucial step when developing dielectrophoresis-based sorting techniques that rely on a difference in the magnitude of $\Re[\tilde{f}_{\text{CM}}]$.

5.6 Conclusion

Using an automated experiment, we measured the effects of ethambutol treatment on the positive dielectrophoretic response of wild-type and ethambutol-treated *Mycobacterium smegmatis*. Additional experiments measured the pDEP response of carboxylate-modified polystyrene microspheres and wild-type *Escherichia coli*. Polystyrene bead data was fit using a surface conductance model and bacterial data were fit using a spheroidal multishell model. This characterization technique offers insight into the frequency regimes where membrane specific differences in mycobacterial cells manifest as significant changes in the dielectrophoretic response.

The automated pDEP characterization of wild-type and ethambutol-treated *mycobacterium smegmatis* performed in this study shows that ethambutol significantly alters cell dielectrophoretic response in a manner that is consistent with a removal or permeabilization of the outer lipid structure of these cells. Wild-type (mc(2)155) *mycobacterium smegmatis* exhibit pDEP response above 5×10^4Hz while ethambutol-treated bacteria exhibited pDEP response only above 2×10^7Hz. This frequency regime may represent a key frequency space where dielectrophoresis-based sorting techniques can be implemented to measure changes in mycobacterial membrane properties associated with chemical treatments or genetic mutation.

5.7 Acknowledgment

This work is supported by the National Science Foundation, grant CBET-0828997. B.G.H. and C.H. also acknowledge support from NSF Graduate Research Fellowships.

BIBLIOGRAPHY

[1] Herbert A Pohl. *Dielectrophoresis: The behavior of neutral matter in nonuniform electric fields*. Cambridge University Press, 1978.

[2] Thomas B Jones. *Electromechanics of Particles*. Cambridge University Press, New York, 1995.

[3] Elizabeth R Rhoades, Rachel E Geisel, Barbara A Butcher, Sean McDonough, and David G Russell. Cell wall lipids from Mycobacterium bovis BCG are inflammatory when inoculated within a gel matrix: characterization of a new model of the granulomatous response to mycobacterial components. *Tuberculosis (Edinburgh, Scotland)*, 85(3):159–76, May 2005.

[4] Johanna Korf, Anton Stoltz, Jan Verschoor, Patrick De Baetselier, and Johan Grooten. The Mycobacterium tuberculosis cell wall component mycolic acid elicits pathogen-associated host innate immune responses. *European journal of immunology*, 35(3):890–900, March 2005.

[5] David Alsteens, Claire Verbelen, Etienne Dague, Dominique Raze, Alain R Baulard, and Yves F Dufrêne. Organization of the mycobacterial cell wall: a nanoscale view. *Pflügers Archiv : European journal of physiology*, 456(1):117–25, April 2008.

[6] K Mikusová, R A Slayden, G S Besra, and P J Brennan. Biogenesis of the mycobacterial cell wall and the site of action of ethambutol. *Antimicrobial agents and chemotherapy*, 39(11):2484–9, 1995.

[7] A Sanchis, A P Brown, M Sancho, G Martínez, J L Sebastián, S Muñoz, and J M Miranda. Dielectric characterization of bacterial cells using dielectrophoresis. *Bioelectromagnetics*, 28(5):393–401, 2007.

[8] Blanca H Lapizco-Encinas, Blake a Simmons, Eric B Cummings, and Yolanda Fintschenko. Dielectrophoretic concentration and separation of live and dead bacteria in an array of insulators. *Analytical chemistry*, 76(6):1571–9, March 2004.

[9] Yoon-Kyoung Cho, Suhyeon Kim, Kyusang Lee, Chinsung Park, Jeong-Gun Lee, and Christopher Ko. Bacteria concentration using a membrane type insulator-based dielectrophoresis in a plastic chip. *Electrophoresis*, 30(18):3153–9, 2009.

[10] M Castellarnau, A Errachid, C Madrid, A Juárez, and J Samitier. Dielectrophoresis

as a tool to characterize and differentiate isogenic mutants of Escherichia coli. *Biophysical journal*, 91(10):3937–45, November 2006.

[11] Jun Yang, Ying Huang, Xiao-Bo Wang, X.B. Wang, F.F. Becker, and P.R.C. Gascoyne. Dielectric properties of human leukocyte subpopulations determined by electrorotation as a cell separation criterion. *Biophysical journal*, 76(6):3307–3314, 1999.

[12] J Yang. Differential Analysis of Human Leukocytes by Dielectrophoretic Field-Flow-Fractionation. *Biophysical Journal*, 78(5):2680–2689, 2000.

[13] P.R.C. Gascoyne, J. Noshari, F.F. Becker, and R. Pethig. Use of dielectrophoretic collection spectra for characterizing differences between normal and cancerous cells. *IEEE Transactions on Industry Applications*, 30(4):829–834, 1994.

[14] Chandra M Das, Frederick Becker, Suzanne Vernon, Jamileh Noshari, Celine Joyce, and Peter R C Gascoyne. Dielectrophoretic segregation of different human cell types on microscope slides. *Analytical chemistry*, 77(9):2708–19, 2005.

[15] C Chou, J Tegenfeldt, S Chan, O Bakajin, E Cox, N Darnton, R Austin, and T Duke. Electrodeless Dielectrophoresis of Single- and Double-Stranded DNA. *Biophysical Journal*, 83(4):2170–2179, October 2002.

[16] Richard W Clarke, Samuel S White, Dejian Zhou, Liming Ying, and David Klenerman. Trapping of proteins under physiological conditions in a nanopipette. *Angewandte Chemie (International ed. in English)*, 44(24):3747–50, June 2005.

[17] Richard Clarke, Joe Piper, Liming Ying, and David Klenerman. Surface Conductivity of Biological Macromolecules Measured by Nanopipette Dielectrophoresis. *Physical Review Letters*, 98(19):198102–6, May 2007.

[18] Ralph Hölzel, Nils Calander, Zackary Chiragwandi, Magnus Willander, and Frank Bier. Trapping Single Molecules by Dielectrophoresis. *Physical Review Letters*, 95(12):128102–4, September 2005.

[19] Blanca H Lapizco-Encinas, Sandra Ozuna-Chacón, and Marco Rito-Palomares. Protein manipulation with insulator-based dielectrophoresis and direct current electric fields. *Journal of chromatography. A*, 1206(1):45–51, October 2008.

[20] M Hughes, H Morgan, F Rixon, J Burt, and R Pethig. Manipulation of herpes simplex virus type 1 by dielectrophoresis. *Biochimica et Biophysica Acta (BBA) - General Subjects*, 1425(1):119–126, September 1998.

[21] Chandra M Das, Frederick Becker, Suzanne Vernon, Jamileh Noshari, Celine Joyce, and Peter R C Gascoyne. Dielectrophoretic segregation of different human cell types on microscope slides. *Analytical chemistry*, 77(9):2708–19, 2005.

[22] Benjamin G Hawkins, A Ezekiel Smith, Yusef A Syed, and Brian J Kirby. Continuous-flow particle separation by 3D Insulative dielectrophoresis using coherently shaped, dc-biased, ac electric fields. *Analytical chemistry*, 79(19):7291–7300, October 2007.

[23] Brian J. Kirby. *Micro- and Nanoscale Fluid Mechanics: Transport in Microfluidic Devices*. Cambridge University press, 2010.

[24] Hywel Morgan and Nicolas G Green. *AC Electrokinetics: Colloids and Nanoparticles*. Research Studies Press, Hertfordshire, 2003.

[25] Julius Adams Stratton. *Electromagnetic Theory*. 1941.

[26] M P Hughes, H Morgan, F J Rixon, J P Burt, and R Pethig. Manipulation of herpes simplex virus type 1 by dielectrophoresis. *Biochimica et biophysica acta*, 1425(1):119–26, September 1998.

[27] Victoria E Froude and Yingxi Zhu. Dielectrophoresis of functionalized lipid unilamellar vesicles (liposomes) with contrasting surface constructs. *The journal of physical chemistry. B*, 113(6):1552–8, 2009.

[28] J Korlach, C Reichle, T Müller, T Schnelle, and W W Webb. Trapping, deformation, and rotation of giant unilamellar vesicles in octode dielectrophoretic field cages. *Biophysical journal*, 89(1):554–62, July 2005.

[29] J. P. Huang, G. Q. Gu, and Mikko Karttunen. Electrorotation in graded colloidal suspensions. *Physical Review E*, 67(5):51405, 2003.

[30] J. J. Bikerman. Electrokinetic equations and surface conductance. A survey of the diffuse double layer theory of colloidal solutions. *Transactions of the Faraday Society*, 35:154, 1940.

[31] Nicolas G. Green and Hywel Morgan. Dielectrophoresis of Submicrometer Latex Spheres. 1. Experimental Results. *The Journal of Physical Chemistry B*, 103(1):41–50, 1999.

[32] MP Hughes, H Morgan, and MF Flynn. The Dielectrophoretic Behavior of Sub-

micron Latex Spheres: Influence of Surface Conductance. *Journal of colloid and interface science*, 220(2):454–457, December 1999.

[33] Michael Pycraft Hughes and Nicolas Gavin Green. The influence of stern layer conductance on the dielectrophoretic behavior of latex nanospheres. *Journal of colloid and interface science*, 250(1):266–8, June 2002.

[34] Antonio Ramos, Hywel Morgan, and Antonio Castellanos. AC Electrokinetics: A Review of Forces in Microelectrode Structures. *Journal of Physics D: Applied Physics*, 31:2338–2353, 1998.

[35] Sieu L Tran and Gregory M Cook. The F1Fo-ATP synthase of Mycobacterium smegmatis is essential for growth. *Journal of bacteriology*, 187(14):5023–8, July 2005.

[36] W. M. Arnold, H. P. Schwan, and U. Zimmermann. Surface conductance and other properties of latex particles measured by electrorotation. *The Journal of Physical Chemistry*, 91(19):5093–5098, 1987.

[37] Mp Hughes, H Morgan, and Mf Flynn. The Dielectrophoretic Behavior of Submicron Latex Spheres: Influence of Surface Conductance. *Journal of colloid and interface science*, 220(2):454–457, December 1999.

[38] Claire Verbelen, Vincent Dupres, Franco D. Menozzi, Dominique Raze, Alain R Baulard, Pascal Hols, and Yves F Dufrêne. Ethambutol-induced alterations in Mycobacterium bovis BCG imaged by atomic force microscopy. *FEMS microbiology letters*, 264(2):192–7, November 2006.

[39] Liem Nguyen, Nicole Scherr, John Gatfield, Anne Walburger, Jean Pieters, and Charles J Thompson. Antigen 84, an effector of pleiomorphism in Mycobacterium smegmatis. *Journal of bacteriology*, 189(21):7896–910, November 2007.

[40] Akemi Takade, Akiko Umeda, Masanori Matsuoka, Shin-ichi Yoshida, Masahiro Nakamura, and Kazunobu Amako. Comparative studies of the cell structures of Mycobacterium leprae and M. tuberculosis using the electron microscopy freeze-substitution technique. *Microbiology and immunology*, 47(4):265–70, January 2003.

[41] T R Paul and T J Beveridge. Reevaluation of envelope profiles and cytoplasmic ultrastructure of mycobacteria processed by conventional embedding and freeze-substitution protocols. *Journal of bacteriology*, 174(20):6508–17, October 1992.

[42] T R Paul and T J Beveridge. Preservation of surface lipids and determination of ultrastructure of Mycobacterium kansasii by freeze-substitution. *Infection and immunity*, 62(5):1542–50, May 1994.

[43] T R Paul and T J Beveridge. Ultrastructure of mycobacterial surfaces by freeze-substitution. *Zentralblatt für Bakteriologie : international journal of medical microbiology*, 279(4):450–7, November 1993.

[44] X-F Zhou, G. H. Markx, Ronald Pethig, and Ian M Eastwood. Differentiation of viable and non-viable bacterial biofilms using electrorotation. *Biochimica et Biophysica Acta (BBA) - General Subjects*, 1245(1):85–93, 1995.

[45] W. M. Arnold, H. P. Schwan, and U. Zimmermann. Surface conductance and other properties of latex particles measured by electrorotation. *The Journal of Physical Chemistry*, 91(19):5093–5098, 1987.

[46] J Gimsa. A comprehensive approach to electro-orientation, electrodeformation, dielectrophoresis, and electrorotation of ellipsoidal particles and biological cells. *Bioelectrochemistry*, 54(1):23–31, 2001.

[47] Kai F Hoettges, Jeremy W Dale, and Michael P Hughes. Rapid determination of antibiotic resistance in E. coli using dielectrophoresis. *Physics in medicine and biology*, 52(19):6001–9, October 2007.

[48] Juliana Johari, Yvonne H Bner, Judith C Hull, Jeremy W Dale, and Michael P Hughes. Dielectrophoretic assay of bacterial resistance to antibiotics. *Physics in Medicine and Biology*, 48(14):N193–N198, July 2003.

CHAPTER 6

CONCLUSION

The primary focus of this work has been to investigate dielectrophoresis devices for particle separation and characterization. The intended outcome of this line of research is the development of a continuous-flow cell enrichment technique that is sensitive to phenotypic differences in the composition of the cell membrane. With this goal in mind, we have developed a continuous-flow particle separation technique that is dependent on dielectrophoretic mobility, examined and quantified the potentially confounding effects of electrothermal flow in insulator-based DEP devices, and characterized the positive dielectrophoretic response of *Mycobacteria* with chemically altered membrane characteristics. These accomplishments enable the description and design of future devices capable of affecting continuous-flow cell enrichment.

6.1 Summary of Accomplishments

Our initial work in developing an insulator-based DEP particle sorting device characterized a novel device geometry consisting of coherently patterned 3D microstructures that modulate the DEP force as a function of transverse channel position. The resulting particle distribution is a continuous-flow stream of particles whose spatial position transverse to the direction of flow is a function of their DEP mobility (see **Chapter 3**). In addition to demonstrating this separation, we developed a set of simplified design criteria to aid researchers in the development of similar devices and developed a new fabrication technique for creating microfluidic devices in Zeonor thermoplastic with high aspect ratios. Similar work in the development of insulator-based DEP techniques has been pioneered by Cummings, et al.[1] and Lapizco-Encinas and co-workers in a series of papers detailing the use of an insulating post-array to manipulate or separate bacteria, DNA, and

proteins[2, 3, 4, 5, 6, 7, 8, 9, 10]. One of the most interesting recent developments in electrode-less dielectrophoresis is the advent of "contactless dielectrophoresis" wherein electric fields are applied to the microchannel by placing highly conductive fluid channels next to the sample analysis channel, separated by a thin wall of PDMS. The thin wall of PDMS prevents mass transfer between the channels, but admits the AC electric field. This technique, developed by Shafii, et al.[11], effectively allows the application of electric fields without the use of microfabricated electrodes, while overcoming the one of the major challenges of insulator-based DEP devices: equipment slew rate limitations owing to the high electric potentials required to generate the electric fields necessary for DEP. The devices used by Lapizco-Encinas and Shafii contain two-dimensional arrays and operate in a batch process mode, trapping some particles between posts within the array while allowing others to pass. In the realm of continuous-flow insulator-based techniques, Barrett and co-workers developed an angled constriction in channel depth and demonstrated separation of *B. subtilis* from a suspension of polystyrene beads[12]. Continuous-flow separation was also demonstrated by Schelle, et al.[13], via the use of a pair of curved electrodes on the top and bottom of a microfluidic channel. The operating principle is the same as the one presented in **Chapter 3**, but implemented using microfabricated electrodes.

As part of our effort to characterize insulator-based dielectrophoresis devices in thermoplastic substrates we undertook a set of numeric simulations to quantitatively assess the effects of electrothermal flow. In **Chapter 4**, we describe a set of multiphysics simulations that address coupled electrical, fluid, and thermal equation systems. The results of this work quantify the impact of electrothermal flow on particle trajectories in insulator-based dielectrophoresis systems. Other researchers have studied particle trajectories in insulator-based DEP devices numerically and experimentally as a technique for size-based separation [14, 15, 16]. The role of channel geometry has been exam-

ined experimentally using an oil drop within the channel to change the constriction ratio [17, 18]. None of these works include the effect of temperature, however. The majority of simulations of Joule heating in microfluidic devices have focused on electrode based systems and static fluids [19, 20]. One notable exception is work done by Kates and Ren [21], who numerically studied a diverging microfluidic channel used for isoelectric focusing (IEF). Their IEF experiments rely on a continuous pH gradient, set up by temperature gradients generated by the application of an electric field to a diverging channel. They performed 3D, numerical simulations of a diverging channel and the surrounding substrate with natural heat convection outside the device. Their results match well with those presented in **Chapter 4**. The results of the work described in **Chapters 3 and 4** will be used to inform the design of future insulator-based DEP devices to be used for cell enrichment studies.

In order to achieve particle separation or enrichment, it is also necessary to characterize the cellular populations under study. In **Chapter 5**, we developed an automated DEP characterization technique and applied it to polystyrene and *E. coli* populations for comparison to similar results in literature. The results of this initial characterization work compare favorably with those found in literature. We subsequently characterized populations of wild-type and ethambutol-treated *M. smegmatis*. The action of ethambutol (discussed in **Chapters 1 and 5**) provides a cellular sample with significantly altered membrane composition. The results of this characterization study show that dielectrophoresis can indeed measure alterations in the membrane structure of *Mycobacteria* and identify a key frequency regime where the DEP force is sensitive to changes in the Mycobacterial membrane composition. These membrane differences can be interpreted within the context of a spheroidal multishell model and, when fit, correspond with a significant increase in the outer membrane (lipid) permittivity and conductivity. In addition to the one developed here, a wide array of techniques are available for

characterization of the dielectrophoretic response of a sample. The majority rely on electrorotation[22, 23, 24, 25, 26] or measurements of the cross over frequency[27]. Electrorotation provides precise information about the cross over frequency while positive and negative DEP techniques provide more precise information about the direction of the DEP force. The use of DEP "collection spectra" has been employed to characterize a number of different cell types, to screen bacteria for antibiotic resistance and to detect cancerous cells[28, 29, 30, 31]. By associating fluorescence intensity with collection spectra, we can automate the data collection and analysis process. The resulting quantitative characterization of $V_{rmtrapping}$ allows comparison of the magnitude of pDEP forces on a particular sample, a crucial step when developing dielectrophoresis-based sorting techniques that rely on a difference in the magnitude of $\Re[f_{\mathrm{CM}}]$.

6.2 Future Work

The work accomplished to date enables several new avenues of experiment. The characterization results for devices and cells presented in **Chapters 3, 4, and 5** can be used to design a device capable of operation in the appropriate frequency regime and with the required sensitivity. Additional testing of cellular subpopulations with known phenotypic differences in membrane composition, rather than gross, chemically induced transformations, will provide additional data to inform the design of separation devices, specifically critical frequency and sensitivity information. The final stage of verification will involve separation of a population of random mutants and characterization of the enriched subpopulation.

BIBLIOGRAPHY

[1] E B Cummings. Streaming dielectrophoresis for continuous-flow microfluidic devices. *Ieee Engineering in Medicine and Biology Magazine*, 22(6):75–84, 2003.

[2] Blanca H Lapizco-Encinas, Blake a Simmons, Eric B Cummings, and Yolanda Fintschenko. Dielectrophoretic concentration and separation of live and dead bacteria in an array of insulators. *Analytical chemistry*, 76(6):1571–9, March 2004.

[3] Blanca H Lapizco-Encinas, Sandra Ozuna-Chacón, and Marco Rito-Palomares. Protein manipulation with insulator-based dielectrophoresis and direct current electric fields. *Journal of chromatography. A*, 1206(1):45–51, October 2008.

[4] Héctor Moncada-Hernández and Blanca H Lapizco-Encinas. Simultaneous concentration and separation of microorganisms: insulator-based dielectrophoretic approach. *Analytical and bioanalytical chemistry*, 2010.

[5] Sandra Ozuna-Chacón, Blanca H Lapizco-Encinas, Marco Rito-Palomares, Sergio O Martínez-Chapa, and Claudia Reyes-Betanzo. Performance characterization of an insulator-based dielectrophoretic microdevice. *Electrophoresis*, 29(15):3115–22, 2008.

[6] Blanca H Lapizco-Encinas, Blake A Simmons, Eric B Cummings, and Yolanda Fintschenko. Insulator-based dielectrophoresis for the selective concentration and separation of live bacteria in water. *Electrophoresis*, 25(10-11):1695–704, 2004.

[7] Roberto C Gallo-Villanueva, Carlos E Rodríguez-López, Rocío I Díaz-de-la Garza, Claudia Reyes-Betanzo, and Blanca H Lapizco-Encinas. DNA manipulation by means of insulator-based dielectrophoresis employing direct current electric fields. *Electrophoresis*, 30(24):4195–205, December 2009.

[8] Javier L Baylon-Cardiel, Nadia M Jesús-Pérez, Ana V Chávez-Santoscoy, and Blanca H Lapizco-Encinas. Controlled microparticle manipulation employing low frequency alternating electric fields in an array of insulators. *Lab on a chip*, October 2010.

[9] B A Simmons, B Lapizco-Encinas, G J Fiechtner, E B Cummings, Y Fintschenko, R Shediac, J Hachman, and J M Chames. Polymeric insulating post electrodeless dielectrophoresis (EDEP) for the monitoring of water-borne pathogens. In *Abstracts of Papers of the American Chemical Society*, volume 227, pages U464–U465, 2004.

[10] Javier L Baylon-Cardiel, Blanca H Lapizco-Encinas, Claudia Reyes-Betanzo, Ana V Chávez-Santoscoy, and Sergio O Martínez-Chapa. Prediction of trapping zones in an insulator-based dielectrophoretic device. *Lab on a chip*, 9(20):2896–901, October 2009.

[11] Hadi Shafiee, Michael B Sano, Erin A Henslee, John L Caldwell, and Rafael V Davalos. Selective isolation of live/dead cells using contactless dielectrophoresis (cDEP). *Lab on a chip*, 10(4):438–45, 2010.

[12] Louise M Barrett, Andrew J Skulan, Anup K Singh, Eric B Cummings, and Gregory J Fiechtner. Dielectrophoretic manipulation of particles and cells using insulating ridges in faceted prism microchannels. *Analytical chemistry*, 77(21):6798–804, 2005.

[13] Thomas Schnelle, Torsten Muller, G Gradl, S G Shirley, and G Fuhr. Paired microelectrode system: dielectrophoretic particle sorting and force calibration. *Journal of Electrostatics*, 47:121–132, 1999.

[14] Yuejun Kang, Dongqing Li, Spyros A Kalams, and Josiane E Eid. DC-Dielectrophoretic separation of biological cells by size. *Biomedical microdevices*, 10(2):243–9, April 2008.

[15] Kwan Hyoung Kang, Xiangchun Xuan, Yuejun Kang, and Dongqing Li. Effects of dc-dielectrophoretic force on particle trajectories in microchannels. *Journal of Applied Physics*, 99(6):064702, 2006.

[16] Kwan Hyoung Kang, Yuejun Kang, Xiangchun Xuan, and Dongqing Li. Continuous separation of microparticles by size with direct current-dielectrophoresis. *Electrophoresis*, 27(3):694–702, 2006.

[17] Irena Barbulovic-Nad, Xiangchun Xuan, Jacky S H Lee, and Dongqing Li. DC-dielectrophoretic separation of microparticles using an oil droplet obstacle. *Lab on a chip*, 6(2):274–9, February 2006.

[18] Prasanna K Thwar, Jennifer J Linderman, and Mark A Burns. Electrodeless direct current dielectrophoresis using reconfigurable field-shaping oil barriers. *Electrophoresis*, 28(24):4572–81, December 2007.

[19] Xiangchun Xuan. Joule heating in electrokinetic flow. *Electrophoresis*, 29(1):33–43, January 2008.

[20] Stuart J. Williams, Pramod Chamarthy, and Steven T. Wereley. Comparison of

Experiments and Simulation of Joule Heating in ac Electrokinetic Chips. *Journal of Fluids Engineering*, 132(2):021103, 2010.

[21] Brian Kates and Carolyn L Ren. Study of Joule heating effects on temperature gradient in diverging microchannels for isoelectric focusing applications. *Electrophoresis*, 27(10):1967–76, May 2006.

[22] X-F Zhou, G. H. Markx, Ronald Pethig, and Ian M Eastwood. Differentiation of viable and non-viable bacterial biofilms using electrorotation. *Biochimica et Biophysica Acta (BBA) - General Subjects*, 1245(1):85–93, 1995.

[23] W. M. Arnold, H. P. Schwan, and U. Zimmermann. Surface conductance and other properties of latex particles measured by electrorotation. *The Journal of Physical Chemistry*, 91(19):5093–5098, 1987.

[24] J. P. Huang, G. Q. Gu, and Mikko Karttunen. Electrorotation in graded colloidal suspensions. *Physical Review E*, 67(5):51405, 2003.

[25] Jun Yang, Ying Huang, Xiao-Bo Wang, X.B. Wang, F.F. Becker, and P.R.C. Gascoyne. Dielectric properties of human leukocyte subpopulations determined by electrorotation as a cell separation criterion. *Biophysical journal*, 76(6):3307–3314, 1999.

[26] J Gimsa. A comprehensive approach to electro-orientation, electrodeformation, dielectrophoresis, and electrorotation of ellipsoidal particles and biological cells. *Bioelectrochemistry*, 54(1):23–31, 2001.

[27] M Castellarnau, A Errachid, C Madrid, A Juárez, and J Samitier. Dielectrophoresis as a tool to characterize and differentiate isogenic mutants of Escherichia coli. *Biophysical journal*, 91(10):3937–45, November 2006.

[28] Kai F Hoettges, Jeremy W Dale, and Michael P Hughes. Rapid determination of antibiotic resistance in E. coli using dielectrophoresis. *Physics in medicine and biology*, 52(19):6001–9, October 2007.

[29] P.R.C. Gascoyne, J. Noshari, F.F. Becker, and R. Pethig. Use of dielectrophoretic collection spectra for characterizing differences between normal and cancerous cells. *IEEE Transactions on Industry Applications*, 30(4):829–834, 1994.

[30] Juliana Johari, Yvonne H Bner, Judith C Hull, Jeremy W Dale, and Michael P Hughes. Dielectrophoretic assay of bacterial resistance to antibiotics. *Physics in Medicine and Biology*, 48(14):N193–N198, July 2003.

[31] A Sanchis, A P Brown, M Sancho, G Martínez, J L Sebastián, S Muñoz, and J M Miranda. Dielectric characterization of bacterial cells using dielectrophoresis. *Bioelectromagnetics*, 28(5):393–401, 2007.